NASA Conference Publication 3353

Conference on the High Energy Radiation Background in Space

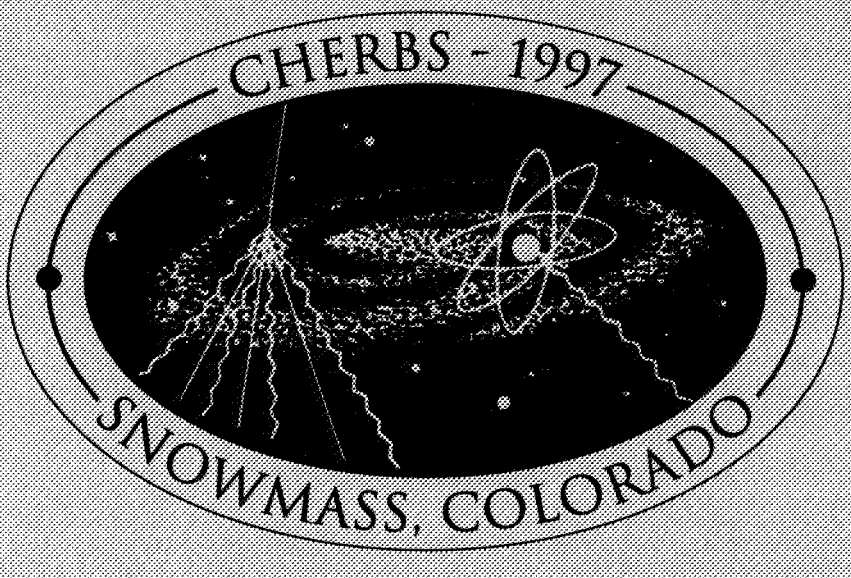

Proceedings of a conference held at
Wildwood Conference Center
Snowmass, Colorado
July 22–23, 1997

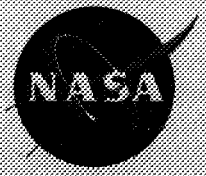

NASA Conference Publication 3353

Conference on the High Energy Radiation Background in Space

Edited by
Pamela H. Solomon
NASA Goddard Space Flight Center
Greenbelt, Maryland

Sponsored by
National Aeronautics and Space Administration,
Goddard Space Flight Center
Constellation Technology Corporation
IEEE/NPSS Radiation Effects Committee,
Nuclear and Sapce Radiation Effects Conference

National Aeronautics
and Space Administration

Goddard Space Flight Center
Greenbelt, Maryland 20771

1997

This publication is available from the NASA Center for AeroSpace Information,
800 Elkridge Landing Road, Linthicum Heights, MD 21090-2934, (301) 621-0390.

Preface

Much has happened both scientifically and technologically since the first "Conference on the High-Energy Radiation Background in Space" (CHERBS) meeting was held on Sanibel, Island in 1987. The intervening decade has seen extensive leaps in our understanding of solar physics, astrophysics, and planetary physics. We have witnessed the substantially increased sophistication of equipment developed for space flight missions utilizing x-ray and gamma-ray detector systems. From the data obtained from recent missions, great insight has been gained on the nature of our solar system, our galaxy, and the extra-galactic universe.

We are very pleased that the 1997 CHERBS meeting has been sponsored by the Goddard Space Flight Center and the IEEE/NPSS Radiation Effects Committee, and held jointly with the "Nuclear and Space Radiation Effects Conference." The synergy of this joint meeting will greatly enhance the assimilation of information relative to detector operation in radiation environments that is vitally important to the planning of future terrestrial and space flight programs.

Dr. Alfred Carl Rester, Jr. was a key organizer of the original CHERBS conference, and before his death on December 2, 1996, contributed significantly to the planning of the 1997 conference. Dr. Rester was a most creative investigator and tireless worker in the field of x-ray and gamma spectroscopy. We miss greatly his scientific contributions, his insightful understanding, and his personal wit and warmth as a friend and collaborator. We sadly but proudly dedicate this meeting to Carl's memory.

Jacob I. Trombka
Goddard Space Flight Center
July, 1997

Page intentionally left blank

In Memory of Alfred Carl Rester, Jr.

The 1997 Conference on the High Energy Radiation Background in Space (CHERBS) is dedicated to the memory of Dr. Alfred Carl Rester, Jr. Known by his friends simply as "Carl," he dedicated his life to advancing nuclear and astrophysical science, and especially, to creating a positive, trusting, and happy environment for others to pursue these sciences as well. He endeared himself to those who knew him for both his caring for people and his love of science.

Together with Dr. Jacob I. Trombka, Carl worked hard as a co-sponsor of CHERBS 1997 to make this conference possible, just as he and Dr. Trombka had done to create CHERBS at its first conference in 1987 at Sanibel Island, Florida. Carl earned a Ph.D. in experimental nuclear physics in 1969 at Vanderbilt University, and began a career in nuclear physics that included work at the Technological University of Delft, Oak Ridge National Laboratory, the University of Bonn, Emory University, Tennessee Technological University, and the University of Florida. In 1988 he founded the Institute for Astrophysics and Planetary Exploration at the University of Florida. Carl led the world's first successful expedition in Antarctica in high-altitude balloon-born astrophysics in 1987, returning with significant measurements for the gamma-ray radiation from Supernova 1987A. In 1992 Carl founded Constellation Technology Corporation in St. Petersburg, Florida. Carl dedicated Constellation's efforts to developing technologies to help make the world safe from the proliferation of nuclear weapons and from nuclear terrorism.

Carl passed away on December 2, 1996, without having the opportunity – except perhaps in spirit here with us – of seeing his vision of a second successful CHERBS come true. We are grateful to him for his vision, enthusiasm, and energy in making this conference possible, and as we share our continuing work in advancing the space radiation sciences we shall all miss him. He is remembered by all as a good friend, an honorable gentleman, and a pioneering visionary in the world of astrophysical exploration.

Page intentionally left blank

Conveners

A. Carl Rester, Jr., Constellation Technology Corporation
Jacob I. Trombka, NASA Goddard Space Flight Center
Jeffrey Schweitzer, University of Connecticut; State University of New York at Albany
George P. Lasche, Constellation Technology Corporation

Sponsors

NASA Goddard Space Flight Center
Constellation Technology Corporation
IEEE/NPSS Radiation Effects Committee
Nuclear and Space Radiation Effects Conference

Organizing and Science Review Committee

Paul Albats
Ridgefield, CT

Larry G. Evans
Computer Sciences Corporation
NASA Goddard Space Flight Center

Gerald Fishman
NASA Marshall Space Flight Center

Neil Gehrels
NASA Goddard Space Flight Center

George P. Lasche
Constellation Technology Corporation

Calvin E. Moss
Los Alamos National Laboratory

Robert R. Reedy
Los Alamos National Laboratory

James M. Ryan
University of New Hampshire

Jeffrey S. Schweitzer
University of Connecticut and State
University of New York at Albany

Pamela H. Solomon
Hughes STX
Goddard Space Flight Center

Richard Starr
Catholic University
NASA Goddard Space Flight Center

Steven M. Seltzer
National Institute of Standards and Tech.

Jacob I. Trombka, Chair
NASA Goddard Space Flight Center

Technical Support

Pamela H. Solomon
Hughes STX
NASA Goddard Space Flight Center

Rita Clark
Constellation Technology Corporation
NASA Goddard Space Flight Center

Page intentionally left blank

Table of Contents

Preface i

Dedication iii

Credits v

Conference Program 1

Summaries 9

T. W. Armstrong, B. L. Colborn, K. L. Dietz, S. L. O'Dell, and M. C. Weisskopf 11
AXAF Detector Backgrounds Produced by Cosmic Ray Protons

T. W. Armstrong, B. L. Colborn, K. L. Dietz, and B. D. Ramsey 15
Neutron Induced Backgrounds in the MIXE-X-Ray Detector at Balloon Altitudes

W. V. Boynton, L. G. Evans, R. Starr, J. BrÅckner, S. H. Bailey and J. I. Trombka 19
Induced Background in the Mars Observer Gamma-Ray Spectrometer

J. Brückner, M. Koenen, L. G. Evans, R. Starr, S. H. Bailey, and W. V. Boynton 23
Charged Particle Induced Radiation Damage of Germanium Detectors in Space: Two Mars Observer Gamma-Ray Detectors

P. Buhler, A. Zehnder, L. Desorgher, W. Hajdas, E. Daly, L. Adams 27
Measurements of the Radiation Belts from MIR and STRV 1994-1997

P. E. Clark, S. R. Floyd, and J. I. Trombka 31
The Effectiveness of the Proportional Counter with a Specially Designed Filter as a Solar X-ray Monitor on the NEAR Mission

V. V. Dmitrenko, A. M. Galper, V. M. Grachev, V. G. Kirillov-Ugryumov, S. V. Krivov, A. A. Moiseev, S. E. Ulin, Z. M. Uteshev, K. F. Vlasik, Yu. T. Yurkin 35
Gamma-Radiation Background Onboard Russian Orbital Stations

V. V. Dmitrenko, A. M. Galper, V. M. Gratchev, V. G. Kirillov-Ugryumov, S. E. Ulin, S. A. Voronov 39
New High Energy Electron Component of Earth Radiation Belt

C. Dyer, P. Truscott, H. Evans, L. Evans, J. I. Trombka 43
Comparison Between Predictions & Observations of Induced Radioactive Background in Interplanetary Missions

L. G. Evans, J. I. Trombka, R. Starr, W. V. Boynton, and S. Bailey 47
Continuum Background in Space-Borne Gamma-Ray Detectors

S. R. Floyd, J. I. Trombka, J. O. Goldsten, E. M. Fiore 51
Cosmic Ray Induced Degradation in X-Ray Detectors on Board the NEAR Spacecraft

A. Gerrish 53
A Monte-Carlo Ray-Tracing Program for Modeling Scintillators

A. Gerrish and L. van den Berg.....57
Perspectives on Mercuric Iodide as a Radiation Detector Material for Space Measurements

B. L. Graham, B. F. Phlips, J. D. Kurfess and R. A. Kroeger.....61
Simulation of HEAO 3 Background

G. P. Lasche, R. L. Coldwell, J. A. Nobel, A. C. Rester, J. I. Trombka.....65
Spectral Analysis in High Radiation Space Backgrounds with Robust Fitting

F. Lei, A. R. Green, A. J. Bird, c. Ferguson, A. J. Dean.....69
The INTEGRAL Mass Model and the GGOD M-C Simulation Suite

D. J. Morris, M. L. McConnell, J. M. Ryan, V. Schönfelder, M. Varendorff, G. Weidenspointner, H. Aarts, K. Bennett.....73
Activation in the COMPTEL Double-Scattering Gamma-Ray Telescope

R. C. Reedy.....77
Radiation Threats from Huge Solar Particle Events

R. C. Reedy, R. D. Belian, T. E. Cayton, M. G. Henderson, J. C. Ingraham, M. M. Meier, G. D. Reeves, and L. A. Weiss.....81
Long-Term Energetic Particle Databases from Geosynchronous and GPS Orbits

J. M. Ryan, S. Kappadath, M. McConnell, D. Morris, V. Schönfelder, M. Varendorff, G. Weidenspointner, W. Hermsen, K. Bennett.....85
The Prompt Cosmic-Ray -Induced Background in the Orbiting Compton Telescope COMPTEL

M. Schieber, A. Zuck, M. Braiman, J. Nissenbaum, R. Turchetta, W. Dulinski, D. Husson, and J. L. Riester.....89
Ceramic Mercuric Iodide Semiconductor Particle Counters

R. Starr, L. G. Evans, S. R. Floyd, J. I. Trombka, D. M. Drake, W. C. Feldman, S. W. Squyres, and A. C. Rester.....93
Induced Radioactivity Measured in a Germanium Detector after a Long Duration Balloon Flight

P. R. Truscott, C. S. Dyer, H. E. Evans, M. Cosby, C. E. Moss.....97
Analysis of Activation Effects in Space-Borne and Proton Beam Irradiated γ-Ray Detectors

A. L. Vampola.....101
Outer Zone Energetic Electron Environment Update

A. L. Vampola and M. Lauriente.....105
Using Cross-Correlations of SEUs and AP8 as a Diagnostic Tool

A. L. Vampola and M. Lauriente.....109
Solar Cycle Variation in the Inner Zone Proton Belt Configuration

V. P. Vasilyev, A. I. Kalinichenko, S. V. Vasilyev.....113
Estimate of Brittle Fracture Effects in Sensor Systems Exposed to Heavy Cosmic Ray Ions

C. B. Wunderer, D. Holslin, J. R. Macri, M. McConnell, J. M. Ryan.....115
SONTRAC - A Low Background, Large Area Solar Neutron Spectrometer

Conference On
High Energy Radiation Background In Space

July 22-23, 1997

Held in conjunction with the IEEE/NSREC Meeting, Snowmass, CO
July 21-25, 1997

Tuesday, July 22

8:45 a.m. Memorial to A. Carl Rester, Jr.
George Lasche, Constellation Technology Corporation

SESSION CHA - INDUCED ACTIVITY

8:55 a.m. Session Introduction
Chairman: Jacob I. Trombka, NASA Goddard Space Flight Center

CHA-1-9:00 a.m. AXAF Detector Backgrounds Produced by Cosmic Ray Protons
T. W. Armstrong, B. L. Colborn, SAIC; K. L. Dietz, S. L. O'Dell, and M. C. Weisskopf, NASA Marshall Space Flight Center
Backgrounds expected for x-ray detectors on the Advanced X-ray Astrophysics Facility from cosmic-ray proton bombardment have been determined by Monte Carlo simulations. Results include the time dependence of prompt and activation backgrounds.

CHA-2-9:15 a.m. Induced Radioactivity Measured in a Germanium Detector after a Long Duration Balloon Flight
R. Starr, Catholic University; L. G. Evans, Computer Sciences Corporation; S. R. Floyd, J. I. Trombka, NASA Goddard Space Flight Center; D. M. Drake, W. C. Feldman, Los Alamos National Research Laboratory; S. W. Squyres, Cornell University; and A. C. Rester, Constellation Technology Corporation
A 13-day long duration balloon flight carrying a germanium detector was flown from Williams Field, Antarctic in December 1992. After recovery of the payload the activity induced in the detector was measured.

CHA-3-9:30 a.m. The Prompt Cosmic-Ray -Induced Background in the Orbiting Compton Telescope COMPTEL
J. M. Ryan, S. Kappadath, M. McConnell, D. Morris, University of New Hampshire; V. Schönfelder, M. Varendorff, G. Weidenspointner, Max-Planck Institute; W. Hermsen, Space Research Organization Netherlands-Utrecht; K. Bennett, ESTEC
To perform a measurement of the cosmic diffuse gamma-ray flux one must overcome the background generated locally by cosmic rays. We report on the spectrum of the prompt component of this background.

9:45 a.m. ***BREAK***

CHA-4-10:20 a.m. Charged Particle Induced Radiation Damage of Germanium Detectors in Space: Two Mars Observer Gamma-Ray Detectors
J. Brückner, M. Koenen, Max-Planck Institut f. Chemie; L. G. Evans, Computer Sciences Corporation; R. Starr, Catholic University; S. H. Bailey, and W. V. Boynton, University of Arizona
Charged particle bombardment induces radiation damage in germanium crystals. The Mars Observer gamma-ray HPGe detector suffered energy resolution degradation in space. These data are compared with accelerator based results of a similar HPGe detector.

CHA-5-10:35 a.m. Analysis of Activation Effects in Space-Borne and Proton Beam Irradiated Gamma-Ray Detectors
P. R. Truscott, C. S. Dyer, H. E. Evans, M. Cosby, DERA-Farnborough; C. E. Moss, Los Alamos National Research Laboratory
Results are presented from Space Shuttle and proton beam (0.3 and 1 GeV) experiments in which BaF_2, GSO, and LSO gamma-ray detector materials were irradiated. These are compared with predicted effects of activation and detector response.

CHA-6-10:50 a.m. Activation in the COMPTEL Double-Scattering Gamma-Ray Telescope
D. J. Morris, M. L. McConnell, J. M. Ryan, University of New Hampshire; V. Schönfelder, M. Varendorff, G. Weidenspointner, Max-Planck Institut; H. Aarts, Space Research Organization Netherlands-Utrecht; K. Bennett, ESTEC
Comparison of spectra from the COMPTEL double-scattering telescope for different orbits and epochs during six years since launch of the Compton Gamma-Ray Observatory shows evidence of activation on a range of time scales.

CHA-7-11:05 a.m. Induced Background in the Mars Observer Gamma-Ray Spectrometer
W. V. Boynton, University of Arizona; L. G. Evans, Computer Sciences Corporation; R. Starr, Catholic University; J. Brückner, Max-Planck-Institut fur Chemie; S. H. Bailey, University of Arizona; and J. I. Trombka, NASA Goddard Space Flight Center
The Mars Observer gamma-ray spectrometer has provided data on background lines due to natural and cosmic-ray induced radioactivity. These data will help determine, for future missions, the detection sensitivity of gamma-ray lines of interest that are at or near the energy of background lines.

CHA-8-11:20 a.m. Cosmic Ray Induced Degradation in X-Ray Detectors on Board the NEAR Spacecraft
S. R. Floyd, J. I. Trombka, NASA Goddard Space Flight Center; J. O. Goldsten, E. M. Fiore, Johns Hopkins University/APL
The x-ray detectors on board the Near-Earth Asteroid Rendezvous (NEAR) spacecraft are argon gas filled proportional counters. Their resolution is checked periodically with an Fe-55 radioactive source. Low energy tailing and broadening of the 6 keV line is observed

SESSION CHB - ANALYSIS METHODS, MODELS, CATALOGS, AND DATA BASES

11:35 Session Introduction
Chairman: James M. Ryan, University of New Hampshire

CHB-1-11:40 a.m. Radiation Threats from Huge Solar Particle Events
R. C. Reedy, Los Alamos National Research Laboratory
One of the greatest radiation hazards away from the Earth's magnetosphere is solar energetic particles. Modern and ancient SEP measurements are reviewed and used together to set limits on possible huge solar particle events.

CHB-2-11:55 a.m. Long-Term Energetic Particle Databases from Geosynchronous and GPS Orbits
R. C. Reedy, R. D. Belian, T. E. Cayton, J. C. Ingraham, M. G. Henderson, M. M. Meier, G. D. Reeves, and L. A. Weiss, Los Alamos National Research Laboratory
Los Alamos has had energetic-particle instruments on many Global Positioning System and geosynchronous satellites for about 2 decades. Databases for electrons and ions measured by these instruments have been created to study space weather.

12:05 *LUNCH*

ANALYSIS METHODS, MODELS, CATALOGS, AND DATA BASES (continued)

CHB-3-1:35 p.m. Spectral analysis in High Radiation Space Backgrounds with Robust Fitting
G. P. Lasche, R. L. Coldwell, J. A. Nobel, A. C. Rester, Constellation Technology Corporation; J. I. Trombka, NASA Goddard Space Flight Center
Spectral analysis software is tested for its ability to fit spectra from space. The approach, which emphasizes the background shape function, is uniquely suited to identifying weak-strength nuclides in high-radiation background environments.

CHB-4-1:50 p.m. Comparison Between Predictions & Observations of Induced Radioactive Background in Interplanetary Missions
C. Dyer, P. Truscott, H. Evans, Space Department, DERA Farnborough; L. Evans, Computer Sciences Corporation; J. I. Trombka, NASA Goddard Space Flight Center
Predictions have been made of the cosmic-ray induced radioactivity in germanium, bismuth germanate and sodium iodide and are compared with data obtained from the Mars Observer and Near Earth Asteroid Rendezvous missions.

CHB-5-2:05 p.m. A Monte-Carlo Ray-Tracing Program for Modeling Scintillators
V. Gerrish, Constellation Technology Corporation
A new Monte-Carlo ray-tracing program useful for designing active scintillator shielding to reduce radiation background effects in space is described. Results are presented for a BGO anti-Compton shield and a CsI(Na) active collimator.

CHB-6-2:20 p.m. Simulation of HEAO 3 Background
B. L. Graham, George Mason University; B. F. Phlips, Naval Research Laboratory/USRA; J. D. Kurfess and R. A. Kroeger, Naval Research Laboratory
Gamma-ray background in the High Resolution Gamma-Ray Spectrometer on HEAO 3 has been Monte Carlo modeled. Decay of nuclei produced by spallation of cosmic rays, trapped protons and their secondaries was included.

CHB-7-2:35 p.m. The INTEGRAL Mass Model and GGOD M-C Simulation Suite
F. Lei, A. R. Green, A. J. Bird, C. Ferguson, A. J. Dean, Physics Dept., University of Southampton
A detailed ESA INTEGRAL gamma-ray satellite mass model is being built and is used as input to the Monte Carlo program GGOD. We present the preliminary background evaluations for the two main gamma-ray instruments and discuss the background minimization.

2:50 ***BREAK***

SESSION CHC - DETECTORS AND DETECTOR SYSTEMS

3:30 p.m. Session Introduction
Chairman: Jeffrey S. Schweitzer, State University of New York at Albany and University of Connecticut

CHC-1-3:35 p.m. SONTRAC - A Low Background, Large Area Solar Neutron Spectrometer
C. B. Wunderer, University of New Hampshire; D. Holslin, SAIC; J. R. Macri, M. McConnell, and J. M. Ryan, University of New Hampshire
SONTRAC will measure neutrons from solar flares using scintillator fibers viewed by CCD cameras to track neutron-proton scatters. SONTRAC rejects all background radiation except neutrons from the solar direction. A prototype is operational.

CHC-2-3:50 p.m. Ceramic Mercuric Iodide Semiconductor Particle Counters
M. Schieber, Hebrew University of Jerusalem and Sandia National Laboratories; A. Zuck, M. Braiman, J. Nissenbaum, Hebrew University of Jerusalem; R. Turchetta, W. Dulinski, D. Husson, and J. L. Riester, LEPSI (ULP/IN2P3)-Strasbourg
Mercuric iodide ceramic radiation detectors, which can act as nuclear particle counters, have been fabricated with single continuous and with linear strip electrical contacts and tested with different kinds of gamma and beta sources and a high energy beam at CERN.

CHC-3-4:05 p.m. Neutron Induced Backgrounds in the MIXE-X-Ray Detector at Balloon Altitudes
T. W. Armstrong,. B. L. Colborn, SAIC; K. L. Dietz, and B. D. Ramsey, NASA Marshall Space Flight Center

The MIXE X-ray astronomy detector has experienced high backgrounds on balloon flights although well shielded against atmospheric gamma-rays and charged particles. Monte Carlo simulations show that this is due to neutron-induced backgrounds from cosmic-ray and albedo sources.

CHC-4-4:20 p.m. Estimate of Brittle Fracture Effects in Sensor Systems Exposed to Heavy Cosmic Ray Ions
P. Vasilyev, A. I. Kalinichenko, S. V. Vasilyev, Kharkiv, Ukraine
A mechanism of brittle fracture in sensor system materials from powerful thermoelastic waves generated in a heavy ion track is studied. The probability of spacecraft sensor system damage is analyzed based on the concept of a damaged zone around the ion trajectory.

CHC-5-4:35 p.m. The Effectiveness of Proportional Counter with a Specially Designed Filter as a Solar X-ray Monitor on the NEAR Mission
P. E. Clark, Catholic University; S. R. Floyd and J. I. Trombka, NASA Goddard Space Flight Center
A proportional counter with a specially designed mask/filter (PCF) to enhance sensitivity at higher energies, and a Si PIN detector (SPD), are being used to measure solar flux on the Near Earth Asteroid Rendezvous (NEAR) mission. The complementary nature of their performances is considered.

CHC-6-4:50 p.m. Perspectives on Mercuric Iodide as a Radiation Detector Material for Space Measurements
A. Gerrish and L. Van den Berg, Constellation Technology Corporation
Mercuric iodide is semiconductor detector material that operates at room temperature, has high detection efficiency, and exhibits good energy resolution over the range 5 keV - 5 MeV. Low power requirements and radiation damage resistance make it well suited for space measurements.

5:05 p.m. End

Wednesday, July 23

SESSION CHD - SPACE ENVIRONMENT BACKGROUND

9:15 a.m. Session Introduction
Chairman: George P. Lasche, Constellation Technology Corporation

CHD-1-9:20 a.m. Continuum Background in Space-Borne Gamma-Ray Detectors
L. G. Evans, Computer Sciences Corp.; J. I. Trombka, NASA Goddard Space Flight Center; R. Starr, Catholic University; W. V. Boynton and S. Bailey, University of Arizona
Measurements of the gamma-ray continuum background made during the cruise portion of a number of planetary missions are compared. The effectiveness of different shield designs in reducing background is evaluated.

CHD-2-9:35 a.m. Solar Cycle Variation in the Inner Zone Proton Belt Configuration
A. L. Vampola, University Research Foundation, and M. Lauriente, NASA Goddard Space Flight Center
SEU data show an inward motion of the inner zone energetic proton flux from solar maximum to minimum. This change, which is due to the change in atmospheric scale height, is not present in the AP8MIN/MAX models.

CHD-3-9:50 a.m. Measurements of the Radiation Belts from MIR and STRV 1994-1997
P. Buhler, A. Zehnder, L. Desorgher, W. Hajdas, Paul Scherrer Institute, Switzerland; E. Daly, L. Adams, ESA/ESTEC, The Netherlands
Environment monitors were launched in 1994, in GTO and on MIR. GTO samples the equatorial regime; MIR the near atmospheric cut-off. The electron belt has had many injection events, including January 1997. MIR data show strong asymmetry. Results are compared with models.

10:05 a.m. ***BREAK***

CHD-4-10:45 a.m. New High Energy Electron Component of Earth Radiation Belt
V. V. Dmitrenko, A. M. Galper, V. M. Gratchev, V. G. Kirillov-Ugryumov, S. E. Ulin, S. A. Voronov, Moscow Engineering and Physics State Institute
The charge ratio, spatial, pitch-angle and energy distribution of the high energy (E_e>10 MeV) electron-positron component of trapped particles in Earth's Radiation Belt are presented. The probable mechanisms of particle generation and trapping are considered.

CHD-5-11:00 a.m. Using Cross-Correlations of SEUs and AP8 as a Diagnostic Tool
A. L. Vampola, University Research Foundation, and M. Lauriente, Goddard Space Flight Center
We demonstrate that spurious effects (SEUs, anomalies, noise in satellite systems) can be used in a 2-D (longitude and latitude) cross-correlation to evaluate AP8 and to indicate the energy of the protons that are producing the effects.

CHD-6-11:15 a.m. Gamma-Radiation Background on Board Russian Orbital Stations
V. V. Dmitrenko, A. M. Galper, V. M. Grachev, V. G. Kirillov-Ugryumov, S. V. Krivov, A. A. Moiseev, S. E. Ulin, Z. M. Uteshev, K. F. Vlasik, Yu. T. Yurkin, Moscow Engineering and Physics State Institute
Gamma-ray background measurements on board Russian orbital missions "Salyut-6", "Salyut-7," "Mir," "Soyuz," and "Progress" have been made since 1979. The dependence of background intensity, in the energy intervals 0.1-8 MeV and 30-600 MeV, on a mission's mass, telescope orientation, and rigidity cut off are presented. The background from man-made source's on the missions was investigated.

CHD-7-11:30 a.m. The Gamma-Ray Background of the Spacecraft with RTG Components Aboard
I. G. Mitrofanov, D. A. Ushakov, A. L. Alisov, A. K. Tonshev, Space Research Institute; C. Moss, R. Reedy, Los Alamos National Research Laboratory; L. Evans, Computer Sciences Corporation
High energy background was measured on the Russian Mars'96 spacecraft which had plutonium generators. Energy spectra up to 2 MeV are presented with high spectral resolution. Main nuclear peaks are resolved, and their photon fluxes are estimated.

CHD-8-11:45 a.m. Outer Zone Energetic Electron Environment Update
A. L. Vampola, Space Environmental Effects
Under ESA auspices, CRRES MEA data were used to train neural networks to predict energetic electron flux levels using 65 years of the Kp magnetic index as the input variable. A replacement environment for AE8 has been produced.

12:00 p.m. ***LUNCH***

CHS - SUMMARY AND DISCUSSION

1:45 p.m. G. P. Lasche, Constellation Technology Corporation; J. M. Ryan, University of New Hampshire; J. I. Trombka, NASA Goddard Space Flight Center; and J. S. Schweitzer, State University of New York, Albany

2:45 p.m. ***End of Conference***

Summaries

Page intentionally left blank

AXAF DETECTOR BACKGROUNDS PRODUCED BY COSMIC RAY PROTONS

T. W. Armstrong[1], B. L. Colborn[1], K. L. Dietz[2], S. L. O'Dell[2], and M. C. Weisskopf[2]

[1]Science Applications International Corporation (SAIC) - Prospect, TN 38477
[2]NASA Marshall Space Flight Center - Huntsville, AL 35812

One of the science instruments on the Advanced X-ray Astrophysics Facility (AXAF), planned for launch in 1998 into a highly elliptical (10,000 km x 140,000 km) orbit, is a microchannel plate High Resolution Camera (HRC) [1]. This detector is designed to provide imaging and spectroscopic observations of x-rays emitted by stellar sources in the 0.1 to 10 keV energy range. Described here are analyses made to determine the expected time-dependent detector background from prompt and delayed (activation) radiation initiated by galactic cosmic-ray (GCR) proton interactions in the spacecraft and payload.

Numerical simulations were made using the coupled set of Monte Carlo radiation transport codes, analysis software, and data bases shown in Fig. 1. The major codes are HETC [2] for nucleon-meson transport, EGS [3] for simulating electromagnetic cascades, and MORSE [4] for low-energy (< 15 MeV) neutron transport. The simulation follows the transport history of photons in the energy range from ~ 100 GeV down to ~ 0.1 keV due to gamma-ray sources from neutral pion decay, high-energy (spallation) collisions, and low-energy neutron inelastic scattering and capture reactions. Also included is radioisotope production and the tracking of gamma-rays, electrons, and positrons from induced radioactivity.

A detailed, 3-D mass model of AXAF (Fig. 2) was developed [5] and interfaced with the transport codes to take into account shielding effects. The CADrays program [6] was used to model and verify the geometry/material configuration and this description then translated to a combinatorial geometry format compatible with the transport code interfaces.

Fig. 3 shows the predicted prompt background in the HRC detector due to GCR proton irradiation at solar minimum. Normal detector operation is in anti-coincidence with counts in an active shield around the detector; a comparison of the two spectra in Fig. 3 indicates the effectiveness of the active shield. Integrated over detector efficiency, the predicted count rate for the prompt background with veto is 0.02 cts/cm^2-s.

The background due to decay radiation from induced radioactivity was computed taking into account the activation of various components — the detector multichannel plates (made of Si, O, Pb, K), detector support structure (Al_2O_3), detector collimator (Ta), and all major components in the Science Instrument Module (SIM) containing the detector. Since activation cross section data for spallation collisions are not available for the large number of different radioisotopes

produced (over 1000 for all materials), these cross sections were computed using the intranuclear-cascade-evaporation nuclear model contained in the HETC code.

The time dependence of the activation background and component contributions is shown in Fig. 4. The activation is dominated by short lived radioisotopes, so the time variation approximately follows the solar cycle variation of the GCR proton environment. Contributions to the total activation come from numerous radioisotopes and various components, indicating that a general simulation approach is needed for accurate predictions.

These results indicate that the prompt and activation x-ray backgrounds in the AXAF HRC detector from cosmic rays have about the same magnitude and time dependence, together contributing $\approx$ 0.04 cts/cm^2-s at solar minimum. This cosmic-ray background level is about the same as the intrinsic detector background expected from the decay of natural ^{40}K in the microchannel plate glass [5]. Including the prompt and activation cosmic-ray backgrounds, the intrinsic background, and non-imaged x-ray backgrounds [5], the total HRC detector background from all sources is predicted to be $\approx$ 0.1 cts/cm^2-s, which is small compared to signal strengths expected for planned measurement scenarios.

References

[1] M. C. Weisskopf, S. L. O'Dell, R. F. Elsner, and L. P. Van Speybroeck, "Advanced X-ray Astrophysics Facility: An Overview" in *X-Ray and Extreme Ultraviolet Optics*, Richard B. Hoover and Arthur B. C. Walker, Jr., Editors, Proc. SPIE **2515**, 312-330 (1995).

[2] T. W. Armstrong and B. L. Colborn, "HETC/LHI, A Thick-Target Radiation Transport Computer Code for Low-Mass Heavy Ion Beams", Nucl. Instr. Meth. **169**, 161 (1980).

[3] Walter R. Nelson, Hideo Hirayama, and David W. O. Rogers, "The EGS4 Code System", Stanford Linear Accelerator Center Report SLAC-265 (Dec. 1985).

[4] E. A. Straker, W. H. Scott, and N. R. Byrn, "The MORSE Code with Combinatorial Geometry", Science Applications Report SAI-72-511-LJ (1972).

[5] K. L. Dietz, R. F. Elsner, M. K. Joy, S. L. O'Dell, B. D. Ramsey, M. C. Weisskopf, T. W. Armstrong, B. L. Colborn, and N. Kanvec, "Shielding Simulations for the Advanced X-ray Astrophysics Facility (AXAF): in *EUV, X-Ray, and Gamma-Ray Instrumentation for Astronomy VI*, O. H. W. Siegmund and J. V. Vallerga, Editors, Proc. SPIE **2518** (1995).

[6] B. L. Colborn, S. J. Ringler, D. W. Potter, and T. W. Armstrong, "CADrays 3-D Mass Model of International Space Station Alpha", Science Applications Intl. Corp. Report SAIC-TN-9502 (Feb. 1995).

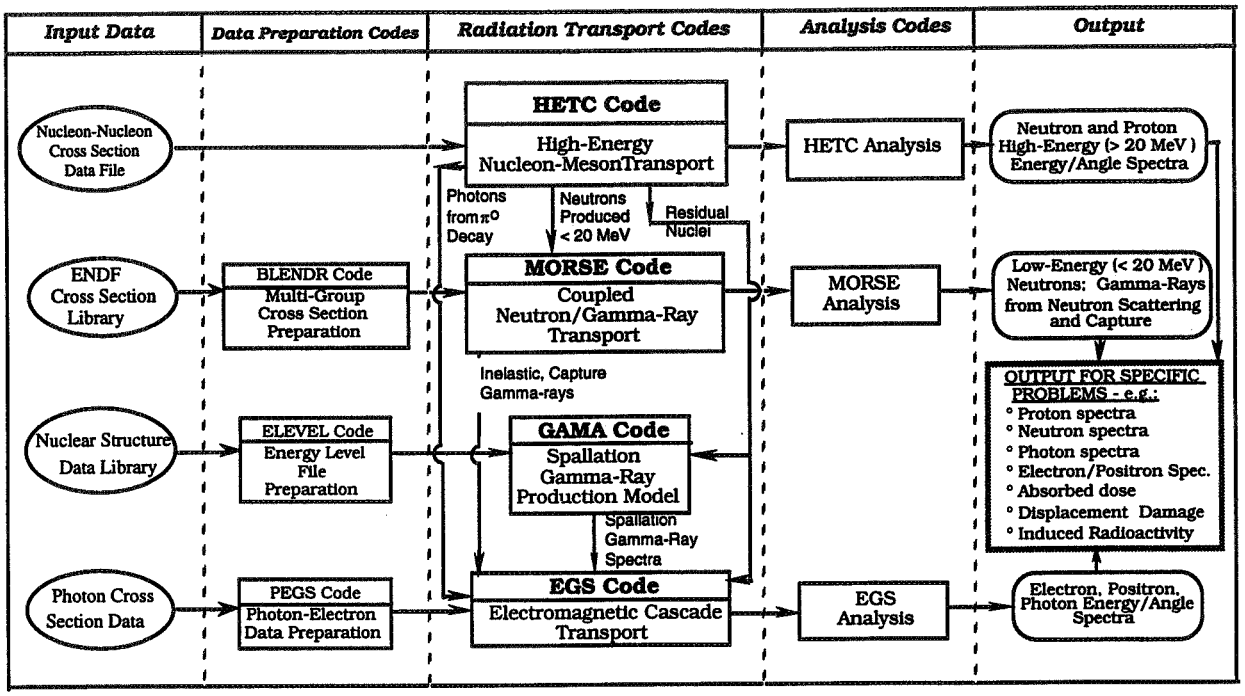

Fig. 1. Coupled Monte Carlo code system used for detector background simulations.

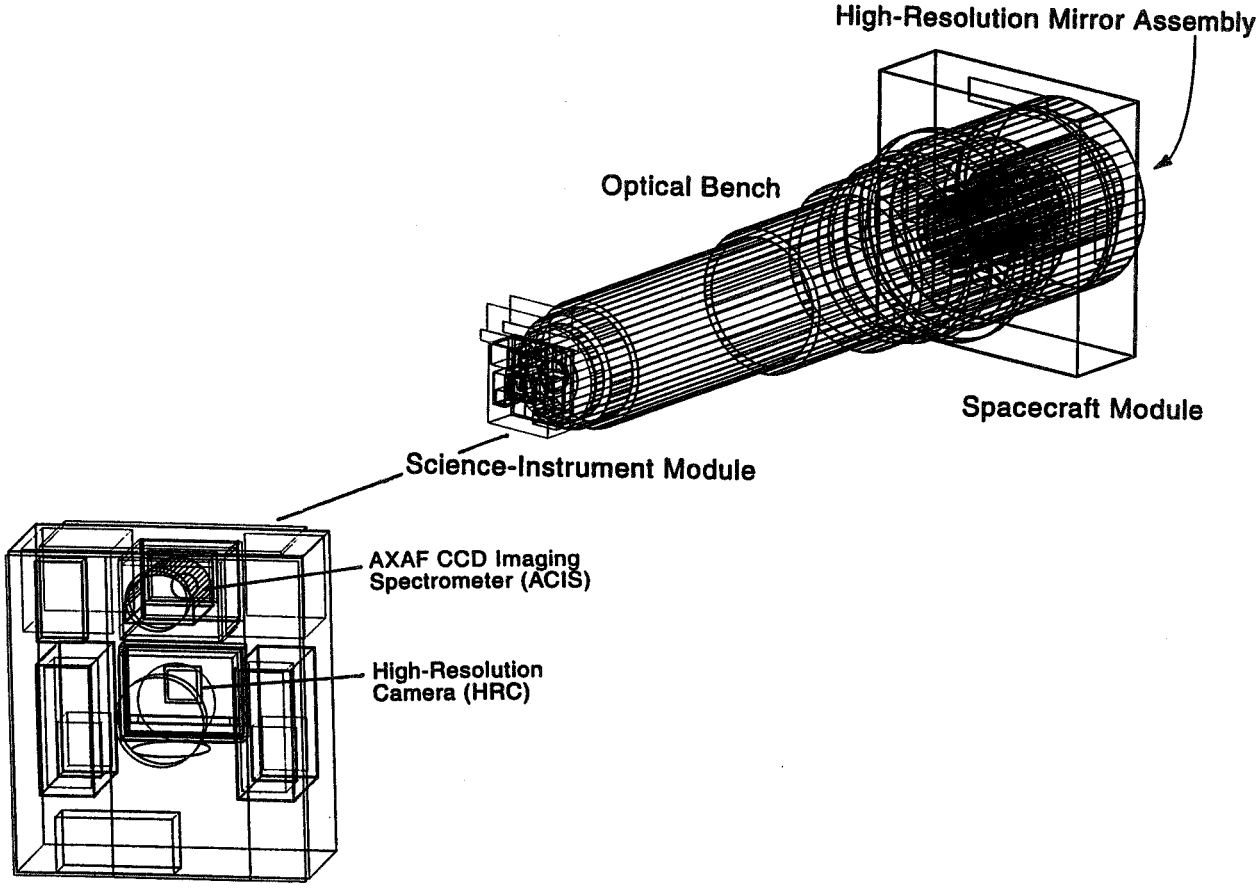

Fig. 2. CADrays mass model of AXAF used in detector background simulations.

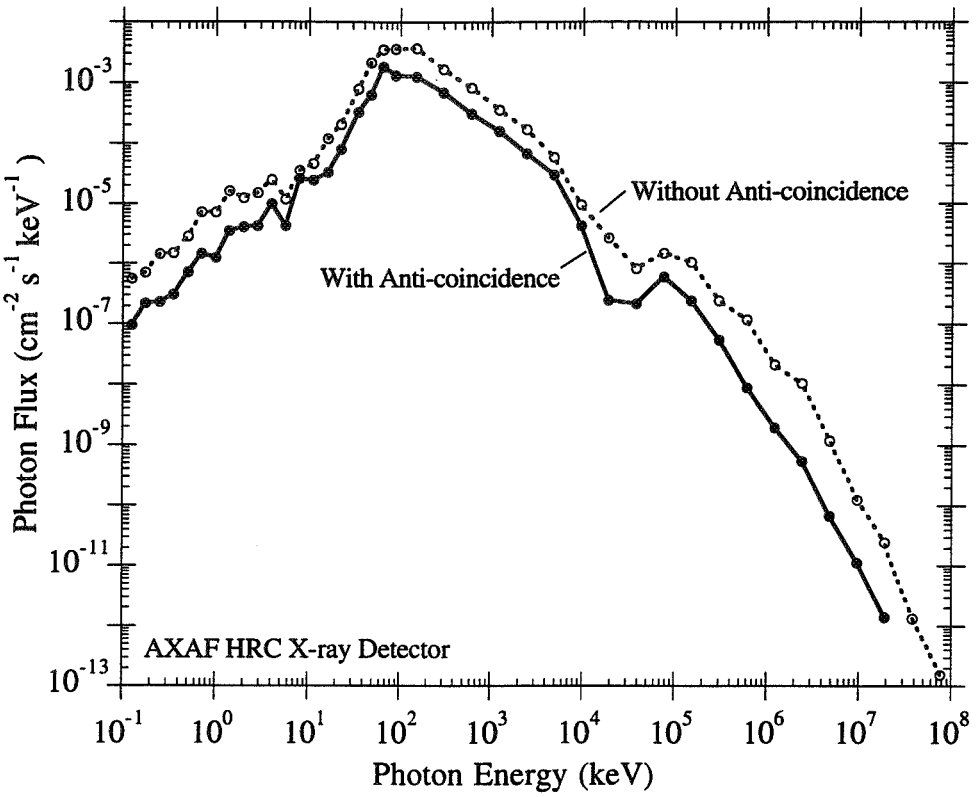

Fig. 3. Predicted prompt photon background spectrum in AXAF HRC x-ray detector due to galactic cosmic-ray proton environment.

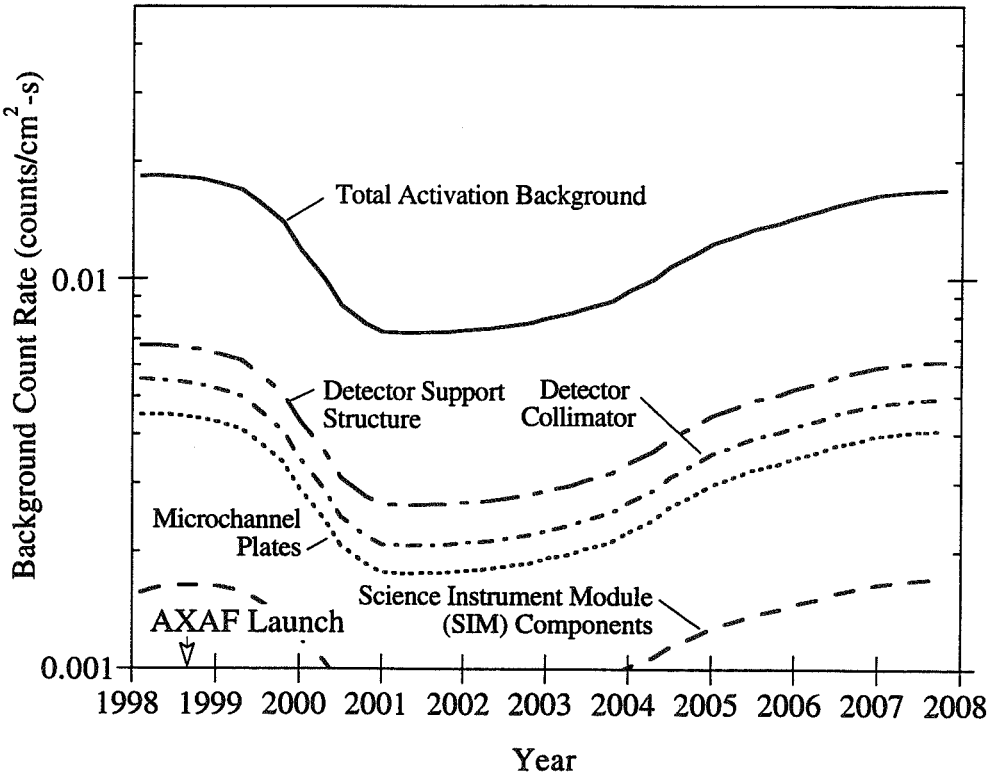

Fig. 4. Predicted time dependence of activation background in AXAF HRC x-ray detector due to galactic cosmic-ray proton environment.

NEUTRON INDUCED BACKGROUNDS IN THE MIXE X-RAY DETECTOR AT BALLOON ALTITUDES

T. W. Armstrong[1], B. L. Colborn[1], K. L. Dietz[2], and B. D. Ramsey[2]

[1]Science Applications International Corporation (SAIC) - Prospect, TN 38477
[2]NASA Marshall Space Flight Center - Huntsville, AL 35812

The MIXE detector developed at NASA/MSFC is designed for x-ray astronomy and consists of a multiwire proportional counter sensitive to photons < 150 keV. The detector has been flown on several balloon flights with higher than expected background levels observed [1]. Previous predictions [1] of the detector background due to atmospheric gamma-ray and cosmic diffuse sources were much less (factor of 3) than flight background measurements. The work reported here was undertaken to determine if the additional contribution from gamma-rays generated by albedo and cosmic-ray induced neutrons in the detector and payload assembly could account for the background levels observed.

Monte Carlo nuclear interaction and radiation transport simulations were made for the ambient cosmic-ray environment corresponding to a previous MIXE balloon flight at 3 g/cm^2 residual atmosphere and 42° N geomagnetic latitude. The omnidirectional albedo neutron spectrum (derived from [2]) and the GCR proton spectrum (derived from [3]) which were used as input to the calculations are shown in Fig. 1. For the albedo angular distribution, the predicted up/down flux ratio of 2.5 from [2] was used together with the angular dependence measured by Preszler, et al. [4].

The calculatons were made using a modified version [5] of the HETC code [6] for nucleon and pion transport and the MORSE code [7] for low-energy neutron and gamma-ray transport. Nucleon and pion production from high-energy nuclear collisions was determined using the intranuclear-cascade-evaporation model in HETC with the GAMA code [8] used to obtain gamma-ray spectra from spallation collisions. Cross sections for gamma-ray production from low-energy neutron capture and inelastic reactions are from the ENDF data library.

A 3-D mass model of the flight payload (Fig. 2) was used in the simulations. To take into account neutron production in materials surrounding the detector assembly, an accompanying flight experiment (named EXCITE) and the aluminum flange holding the experiments were included. The version of the MIXE detector assembly considered includes a molybdenum pressure vessel, miscellaneous structure, electronics, and other materials comprising the detector, a molybdenum collimator with stainless steel walls, and an electronics box. Since the detector is operated in anti-coincidence with counts in the outer regions of the sensitive detection volume, this anti-coincidence region was explicitly modeled.

Fig. 3 shows the predicted neutron induced gamma-ray flux spectra on the inside walls of the detector pressure vessel. (Additional photon transport calculations inside the pressure vessel to obtain the low-energy x-ray spectrum in the sensitive detection region are not yet completed.) Fig. 3 indicates that when operated in a veto mode about 50% of the neutron-induced gamma-ray background is from low-energy (< 20 MeV) capture and inelastic scattering reactions due to GCR secondary neutrons, 25% is from capture and scattering reactions by albedo neutrons, and 25% from high-energy (> 20 MeV) neutron (and some proton) induced spallation reactions (mainly of GCR origin). Significant neutron sources are from production in the pressure vessel walls and in the accompanying EXCITE experiment.

The background from albedo and GCR-induced neutrons is 2.6 times higher than the background from atmospheric gamma-rays (Fig. 4), which is consistent with flight observations. A detailed spatial mapping of the neutron production and associated background environment in the detector assembly has been made [9] to assist in design modifications for background reduction.

References

[1] C. R. Brown, K. L. Dietz, B. D. Ramsey, and M. C. Weisskopt, "Background in X-ray Astronomy Proportional Counters", IEEE Trans. Nucl. Sci. 38 [2] 585, April 1991.

[2] T. W. Armstrong, K. C. Chandler, and J. Barish, "Calculations of Neutron Flux Spectra Induced in the Earth's Atmosphere by Galactic Cosmic Rays", J. Geophys. Res. 78 (16), 2715 (1973).

[3] J. H. Adams, Jr., R. Silberberg, and C. H. Tsao, "Cosmic Ray Effects on Microelectronics, Part I: The Near-Earth Particle Environment", Naval Research Laboratory Memorandum Report 4506, August 1981.

[4] Alan M. Preszler, Shin Moon, and R. Stephen White, "Atmospheric Neutrons", J. Geophys. Res. 81 (25), 4715 (1976).

[5] T. W. Armstrong and B. L. Colborn, "HETC/LHI, A Thick-Target Radiation Transport Computer Code for Low-Mass Heavy Ion Beams", Nucl. Instr. Meth. 169, 161 (1980).

[6] T. W. Armstrong and K. C. Chandler, "HETC: A High Energy Transport Code", Nucl. Sci. Engr. 49, 110 (1972).

[7] E. A. Straker, W. H. Scott, and N. R. Byrn, "The MORSE Code with Combinatorial Geometry", Science Applications Report SAI-72-511-LJ (1972).

[8] T. W. Armstrong and B. L. Colborn, "GAMA, A Code for Predicting Gamma-ray Spectra from Spallation Collisions", unpublished.

[9] T. W. Armstrong and B. L. Colborn, "Predictions of Cosmic-ray Induced Backgrounds in the MIXE X-ray Detector at Balloon Altitudes", Science Applications Int'l Corp. Report SAIC-TN-96070, Oct. 1996.

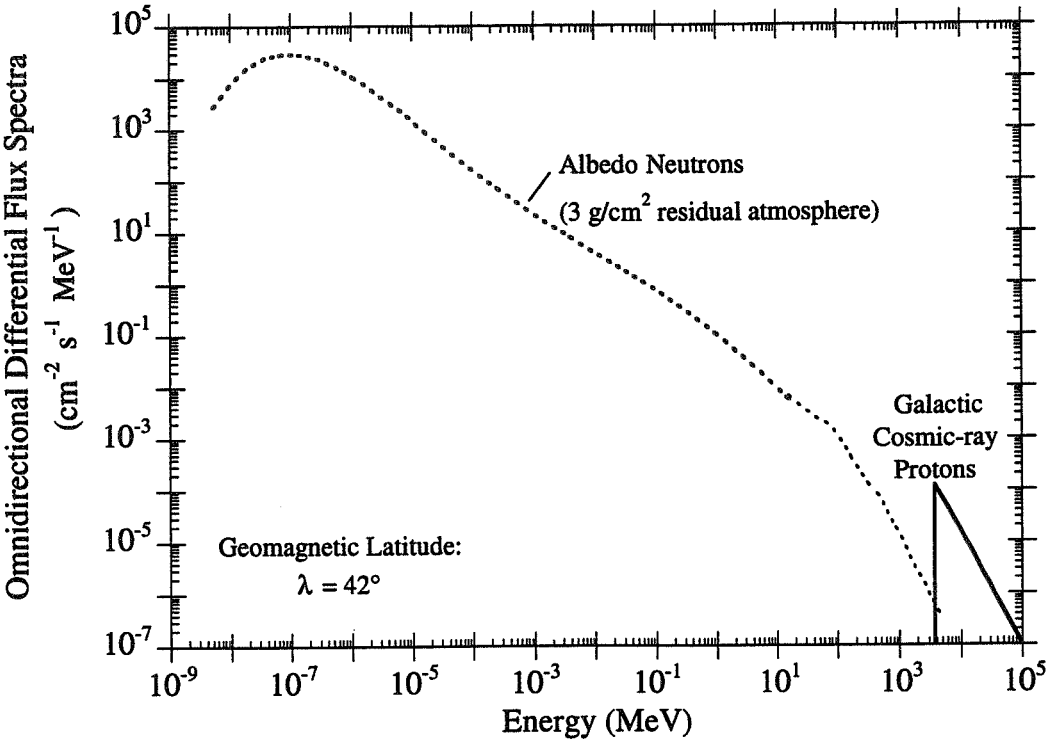

Fig. 1. Background environment used as input for simulations.

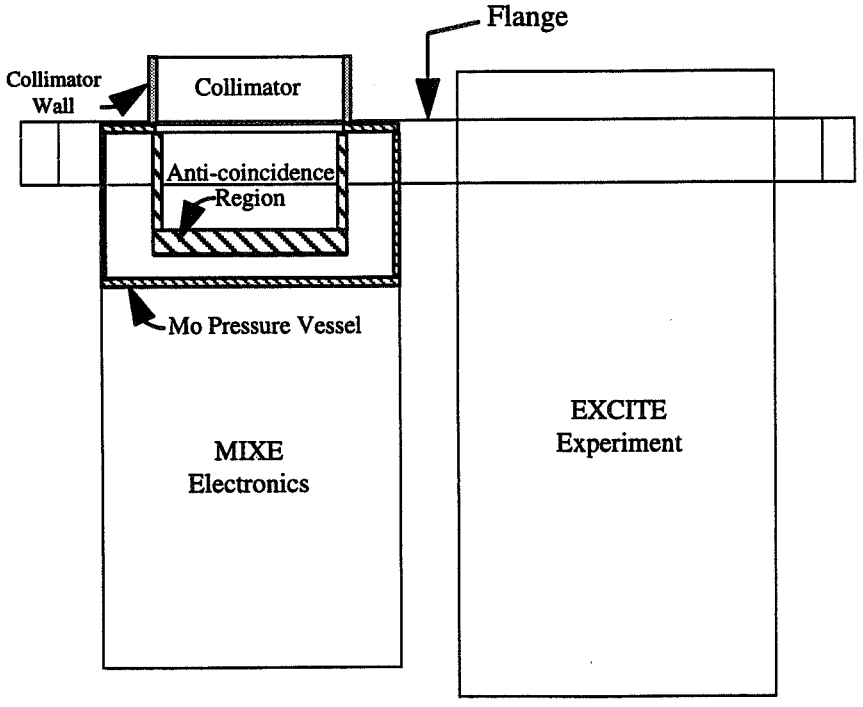

Fig. 2. MIXE detector and flight payload model.

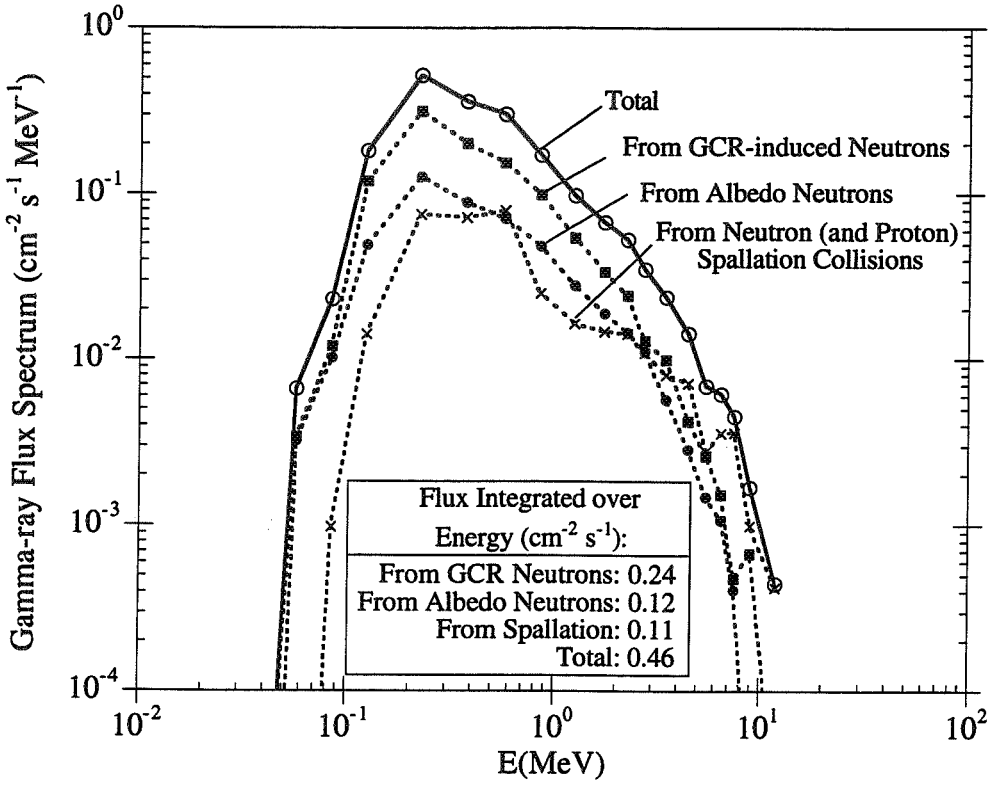

Fig. 3. Predicted contributions to gamma-ray background at inside walls of detector pressure vessel from neutron interactions due to albedo neutron and GCR environment.

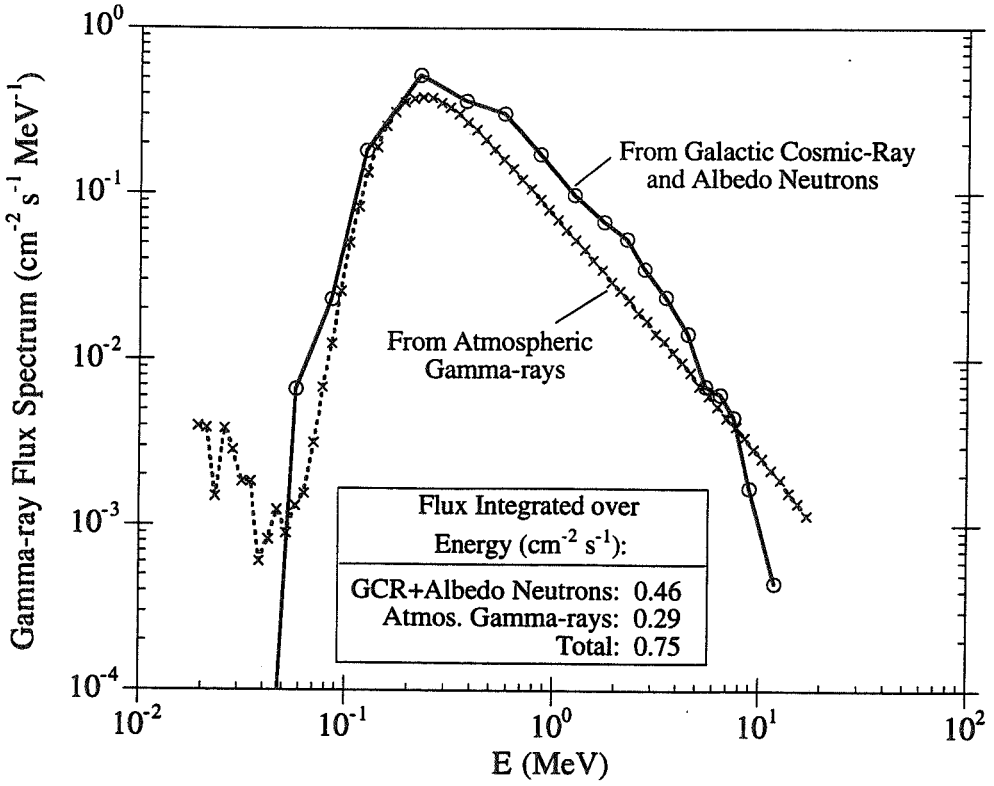

Fig. 4. Comparison of neutron induced background ("total" curve of Fig. 3) with background from atmospheric gamma-rays.

INDUCED BACKGROUND IN THE MARS OBSERVER GAMMA-RAY SPECTROMETER

William V. Boynton[1], Larry G. Evans[2], Richard Starr[3], Johannes Brückner[4], S. H. Bailey[1], and Jacob I. Trombka[5]

[1]Lunar and Planetary Laboratory, University of Arizona, Tucson AZ 85721, USA
[2]Computer Sciences Corporation, Science Programs, Lanham-Seabrook MD 20706, USA
[3]The Catholic University of America, Washington DC 20064, USA
[4]Max-Planck-Institut für Chemie, Mainz, FRG
[5]Code 691, NASA/Goddard Space Flight Center, Greenbelt MD 20771, USA

1. Introduction

Gamma-Ray Spectrometers in space must necessarily work in an environment of a background of lines due to natural and cosmic-ray-induced radioactivity and lines due to prompt emission following nuclear reactions caused by primary and secondary cosmic rays. The Gamma-Ray Spectrometer (GRS) on the Mars Observer mission has provided important data allowing one to estimate for future missions the extent of the background due to cosmic rays. These data will help in the design of instruments and in calculation of realistic background intensities that may effect the sensitivity of determining the intensity of lines of interest.

2. The Mars Observer mission

Mars Observer was launched on September 26, 1992 to arrive at Mars after an 11-month cruise. Shortly before arrival, on August 21, 1993, contact was lost with the spacecraft following the pressurization of the propellent tank for the orbital-insertion rocket motor. During much of the cruise to Mars, the GRS was actively collecting background data. The instrument provided over 1200 hours of data collection during periods of both quiescent sun and solar flares. These cruise data are the basis of this work.

3. The GRS instrument

The GRS is described in detail by Boynton et al. (1992). It used a passively cooled high-purity n-type germanium sensor to detect gamma-ray photons in the energy range of approximately 0.2 to 10 MeV. The sensor was a closed-end co-axial detector, 5.5 cm diameter by 5.5 cm long, and had an efficiency along its axis of 34 % at 1332 keV relative to a 76 mm by 76 mm NaI(Tl) detector. The detected energy of the events was digitized by a 14-bit analog-to-digital converter, but in order to reduce memory size, events greater than count 4095 we processed with an effective 13-bit ADC by dropping the least significant bit. Thus the gamma-ray spectrum is a histogram of events in which the top 12 k channels were compressed into 6 k channels yielding 10 k channels in the instrument memory. The spectra were taken with a very short duration (typically 20 s) and were combined on the ground to get reasonable statistics over long counting intervals. The instrument was built by Lockheed Martin Astronautics (then Martin-Marietta) in Denver for the Mars Observer Flight Investigation Team.

The sensor was surrounded by an active charged-particle shield using a thin (0.5 cm) plastic scintillator and four photo multiplier tubes. The Ge detector was normally operated in anti-coincidence with the shield to eliminate events caused by high-energy charged particles from contaminating the gamma-ray photon spectrum. We had the ability to disable this shield, and by doing so we found that the suppression ranged from a factor of three at 10 MeV to a factor of 2 at 5 MeV (Evans et al., 1997)

During the time of the cruise, the detector spectral resolution degraded due to radiation damage from 2.4 keV FWHM at 1332 keV shortly after launch to 5.5 keV 11 months later. The estimated fluence of charged particles was about 10^8 particles $cm^{-2}s^{-1}$. The GRS sensor radiator was designed to satisfy a 100 K requirement for the operating temperature (with a goal of 90 K), but unfortunately an unknown heat leak caused the performance to be about 30% worse than the design yielding temperatures that ranges from 113 K in the early parts of cruise when we were close to the Earth to 107 K as the spacecraft approached Mars. This higher temperature undoubtably contributed to the radiation damage, as it is known that lower operating temperatures contribute to a lower sensitivity to radiation damage (Pehl et al., 1978, Brückner et al., 1991).

The GRS was mounted on a boom that allowed the instrument to get away from the spacecraft to lower the intensity of the background gamma rays produced in the spacecraft. The boom could extend to a length of 6 meters, but during cruise, it was extended for only 1 meter. Thus background from the spacecraft was a greater contribution during cruise than it would have been at Mars.

4. Results

The spectra from the last portion of cruise were summed together (accumulation time of 724 hours) for this analysis. This period was a time of low solar-flare activity. A plot of the lower energy portion of the spectrum is shown in figure 1. A total of 45 prominent lines were found in the spectra returned from the GRS during cruise. The energy of the lines and their intensities are given in table 1. In addition to normal near-gaussian gamma-ray lines, we also observed irregular sawtooth-shaped lines with a sharp decrease in intensity at the low-energy side and a much more gradual decrease on the high-energy side. These lines can be seen in figure 2 and are due to interactions of energetic neutrons with Ge that have various amounts of recoil energy imparted to the nucleus which is added to the photon transition energy (Brückner et al., 1987).

In most cases the lines were identified based on their energy and our understanding of the target materials near the sensor. The composition of the entire sensor head was very well known, as we were planning on using this information in order to correct the spectra taken in the vicinity of Mars. As can be seen in table 1, most of the lines are from the germanium sensor itself, but some are due to Ti from the instrument structure and the encapsulation material for the sensor, H from the charged-particle shield and fuel in the spacecraft, Si from the photo multiplier tubes in the charged-particle shield, and Al from the structure of the spacecraft. In some cases we were also able to confirm our assignment of the transition by comparing the half-lives of the lines as they decayed away following the end of the large solar flare event which occurred shortly after launch on 1 November 1992. These data are shown in table 2.

5. Conclusions

The data show that there is a significant intensity of gamma line due to interactions in the germanium sensor. The other lines due to interactions in the surrounding materials are all significantly smaller except for the 983 keV line due to interactions with Ti. In all cases the lines are small compared with the continuum, so these lines are only important in reducing the sensitivity of lines that are close enough to the background lines that there is a spectral overlap; the increase in continuum due to these lines would be insignificant in reducing the signal-to-background ratio for lines that are not directly interfered.

References

Boynton, W.V., Trombka, J.I., Feldman, W.C., Arnold, J.R., Englert, P.A.J., Metzger, A.E., Reedy, R.C. Squyres, S.W., Wänke, H, Bailey, S.H., Brückner, J.L., Callas, J.L., Drake, D.M., Duke, P., Evans, L.G.,

Haines, E.L., McCloskey, F.C., Mills, H., Shinohara, C., and Starr, R. (1992) J. Geophys. Res., 97:7681-7698.

Brückner, J., Wänke, H. and Reedy, R.C., (1987) Proceedings of the 18th Lunar and Planetary Science Conference in J. Geophys. Res. 92:E603-E816.

Brückner, J, Korfer, M., Wänke, H., Schroeder, A.N.F., Filges, D., Dragovitsch, P., Englert, P. A. J., Starr, R., Trombka, J. I., Taylor, I., Drake, D. M., Shunk, E. R., (1991) IEEE Trans. Nucl. Sci., 38:209-217.

Evans, L. G., Trombka, J. I., Starr, R., Boynton, W. V., and Bailey, H., (1997) this conference.

Pehl, R. H., Varnell, L. S., and Metzger, A. E., (1978), IEEE Trans. Nucl. Sci., 25:409-417.

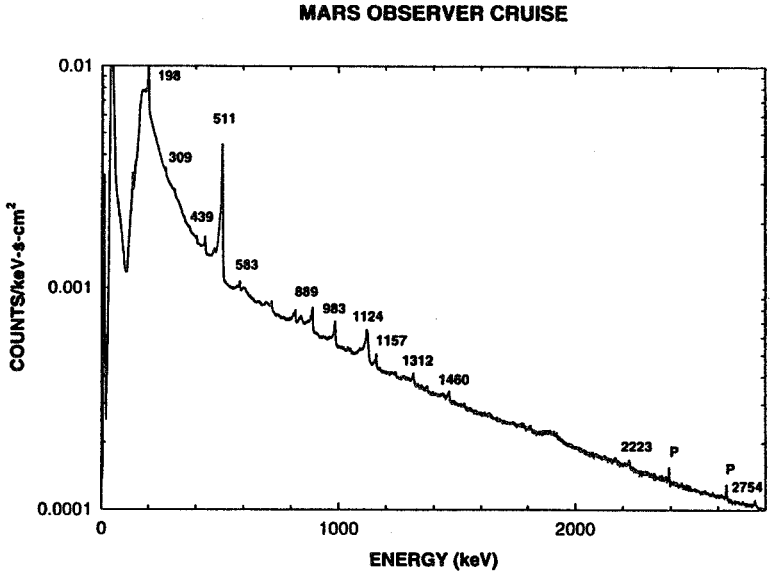

Figure 1. Low energy portion of the Mars Observer cruise spectrum with prominent peaks labeled in energy (keV) and two pulser peaks labeled with P.

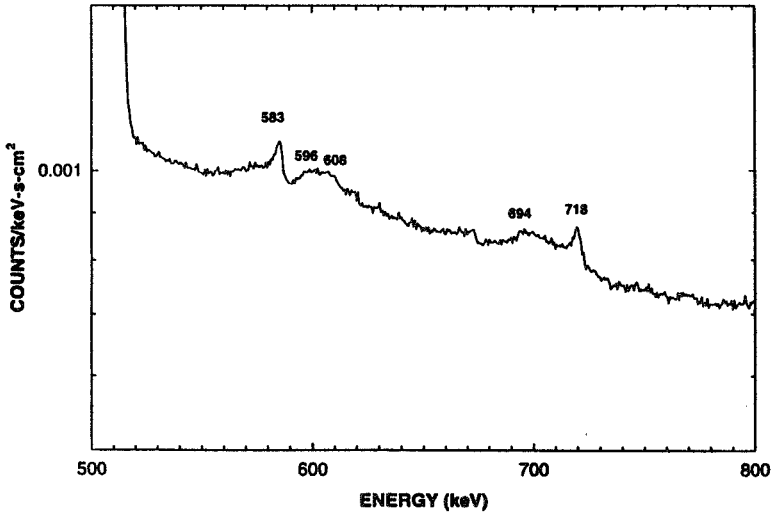

Figure 2. Details of spectrum including the saw-toothed peaks at 596, 608 and 694 keV.

TABLE 1

PROMINENT GAMMA-RAY BACKGROUND LINES IN MO GRS DATA

Energy	MO Cruise Count Rate[1]	Isotope	Half-Life	Reaction	Energy	MO Cruise Count Rate[1]	Isotope	Half-Life	Reaction
125	0.0070[2]	^{65}Ga	15 m	spallation	835		^{54}Mn	312 d	spallation
130	0.060[2]	^{57}Co	270 d	spallation	841	0.010	^{54}Mn	312 d	spallation
140	0.022[2]	^{75m}Ge	48 s	^{76}Ge(p,p'n)	846	0.0083	^{56}Mn	2.6 h	spallation
144	0.012[2]	^{57}Co	270 d	spallation	883	0.010	^{69}Ge	39 h	^{70}Ge(p,p'n)
160	0.042[2]	^{65}Ga	15 m	spallation	889	0.033	^{74}Ge	prompt	^{74}Ge(n,n')
186	0.035	^{71}As	65 h	^{72}Ge(p,2n)	983	0.040	^{48}V	16 d	^{48}Ti(p,n)
194	0.076	^{67}Ga	78 h	^{70}Ge(p,α)			^{48}Sc	1.8 d	^{48}Ti(n,p)
198	0.51	^{71m}Ge	20 ms	^{72}Ge(p,p'n)	1039	SAW	^{70}Ge	prompt	^{70}Ge(n,n')
271	0.020	^{44m}Sc	59 h	spallation			^{66}Ga	9.4 h	^{70}Ge(p,nα)
309	0.0.009	^{67}Ga	78 h	^{70}Ge(p,α)	1049	0.0035	^{66}Ga	9.4 h	^{70}Ge(p,nα)
373	0.003				1087	0.005	^{68}Ga	68 m	^{72}Ge(p,nα)
403	0.0076	^{67}Ga	78 h	^{70}Ge(p,α)	1117	0.017	^{69}Ge	39 h	^{70}Ge(p,p'n)
439	0.039	^{69m}Zn	14 h	spallation	1124	0.013	^{65}Zn	241 d	spallation
478	0.0090	^{7}Be	53 d	spallation	1157	0.012	^{44}Sc	3.9 h	spallation
500	0.121				1312	0.0073	^{48}V	16 d	^{48}Ti(p,n)
511	0.532.	e^+e^-		annihilation			^{48}Sc	1.8 d	^{48}Ti(n,p)
583	0.013	^{69}Ge	39 h	^{70}Ge(p,p'n)	1368	0.0025	^{24}Na	15 h	^{27}Al(n,α)
596	SAW[3]	^{74}Ge	prompt	^{74}Ge(n,n')	1435	0.0026	^{52m}Mn	21m	spallation
		^{74}As	18d	^{74}Ge(p,n)			^{52}Mn	5.6d	spallation
608	SAW	^{74}Ge	prompt	^{74}Ge(n,n')	1460	0.0066	^{40}K	natural radioactivity	
		^{74}As	18d	^{74}Ge(p,n)	1525	0.0022			
694	SAW	^{72}Ge	prompt	^{72}Ge(n,n')	1778	0.0026	^{28}Al	2.2 m	^{27}Al(n,γ)
718	0.0079				1809	0.0029	^{26}Al	$7x10^5$ y	
811	0.0066	^{58}Co	71d	spallation	2223	0.0040	^{2}H	prompt	^{1}H(n,γ)
818	0.018	^{58}Co	71 d	spallation	2754	0.0013	^{24}Na	15 h	^{27}Al(n,α)
835	SAW	^{72}Ge	prompt	^{72}Ge(n,n')	2758		^{66}Ga	9.4 h	^{70}Ge(p,nα)

Notes: 1 - Count rate (counts per second) during final cruise portion of the mission (9-10 months after launch).
2 - Energies below approximately 180 keV were below the low-level discrimator energy, and the count rates are not a true measure of the intensity.
3 - SAW: saw tooth peaks from direct neutron interactions in Ge crystal.

TABLE 2

ISOTOPE IDENTIFICATION MEASURMENTS

Energy	Isotope	Half-Life	Measured Half-Life MO Post-Flare[1]
186	^{71}As	65 h	66 h
194	^{67}Ga	78 h	73 h
271	^{44m}Sc	59 h	57 h
309	^{67}Ga	78 h	57 h
403	^{67}Ga	78 h	56 h
583	^{69}Ge	39 h	32 h
983	^{48}V	16 d	18 d
1312	^{48}V	16 d	12 d

1 - Measurements taken with the MO detector after a solar particle event on 1 November, 1992.

Charged Particle Induced Radiation Damage of Germanium Detectors in Space: two Mars Observer Gamma-Ray Detectors

J. Brückner [1], M. Koenen [1], L. G. Evans [2], R. Starr [2], S. H. Bailey [3], and W. V. Boynton [3]
[1] Max-Planck-Institut f. Chemie, Postfach 3060, D-55020 Mainz, Germany; [2] Goddard Space Flight Center, Greenbelt, MD, US; [3] University of Arizona, Tucson, AZ, US.

The Mars Observer Gamma-Ray spectrometer (MO GRS) was designed to measure gamma-rays emitted by the Martian surface. This gamma-ray emission is induced by energetic cosmic-ray particles penetrating the Martian surface and producing many secondary particles and gamma rays. The MO GRS consisted of an high-purity germanium (HPGe) detector with a passive cooler [1]. Since radiation damage due to permanent bombardment of energetic cosmic-ray particles (with energies up to several GeV) was expected for the MO GRS HPGe crystal, studies on radiation damage effects of HPGe crystals were carried on earth. One of the HPGe crystals (paradoxically called FLIGHT) was similar to the MO GRS crystal. Both detectors, MO GRS and FLIGHT, contained closed-end coaxial n-type HPGe crystals and had the same geometrical dimensions (5.6 x 5.6 cm). Many other parameters, such as HV and operation temperature, differed in space and on earth, which made it somewhat difficult to directly compare the performance of both detector systems. But among other detectors, detector FLIGHT provided many useful data to better understand radiation damage effects.

Detector FLIGHT consisted of a temperature variable cryostat (TVC) to investigate the expected temperature range of MO GRS in space. Since an operational lifetime for MO GRS of at least 3 years in space was planned, we had to expose detector FLIGHT to an equivalent particle fluence. Since cosmic rays consist mainly of protons (ca. 90 %), we limited our studies to the exposure of HPGe detectors to energetic protons (1 to 1.5 GeV). We performed several irradiation experiments at the French accelerator SATURNE. Three large-volume n-type HPGe detectors together with detector FLIGHT were positioned on movable carts in the beam line of the accelerator [2]. Several proton flux detectors were place in the beam line to control the accelerator performance and to measure the accumulated proton dose for each HPGe crystal. The irradiation was performed incrementally, i.e. after each proton irradiation step, where a chosen proton fluence had been accumulated, the proton beam was interrupted and several gamma-ray measurements were carried out to determine the degradation of the energy resolution as function of proton fluence. We are aware that a short-term high-flux proton irradiation (10^5 protons per cm^2 and sec) at an accelerator does not simulate correctly long-term low-flux irradiation in space (3 to 4 particles per cm^2 and sec), but, it is a first order approximation, especially if the detectors are kept at operation temperature, all the time.

In the laboratory, detectors have operating temperatures ranging typically between 95 and 105 K depending on cryostat performance and quality of vacuum. In space, any temperature below 130 K is acceptable for measurements, but, not advantageous, especially, if radiation damage is accumulated. The reason is that for radiation damaged n- and p-type detectors there is

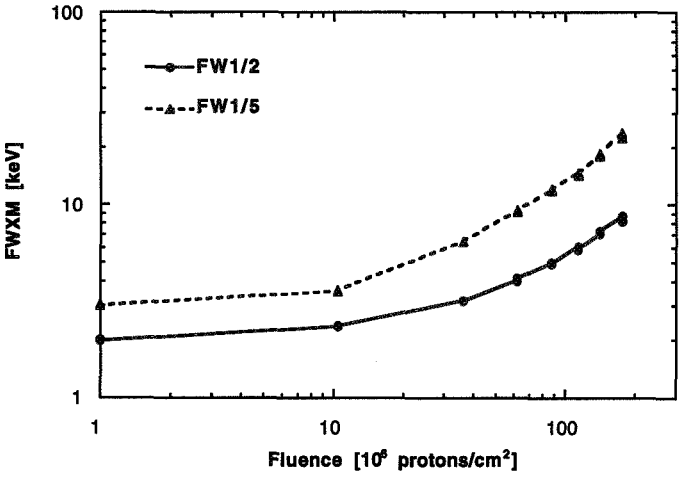

Fig. 1: Energy resolution degradation (FWXM with X= 1/2 and 1/10) of detector FLIGHT as function of received proton fluence after each incremental irradiation.

a strong dependence of the energy resolution degradation on the operation temperature and even past temperature history [2, 3].

In Fig. 1, the degradation of energy resolutions of detector FLIGHT as function of received proton fluence are shown. The resolution is given as full-width-at-half-maximum (FW1/2) and full-width-at-fifth-maximum (FW1/5). Under the given conditions, FW1/2 increases from 2 to 8 keV, while FW1/5 from 3 to 23 keV. This shows that for n-type detectors the lower part of the peak is relatively stronger affected by radiation damage than the upper part. This asymmetrical broadening of the peak, low-energy tailing, reduces the signal-to-noise ratio performance of the detector with time. Detector FLIGHT was operating at a temperature of 110 K during the (second) radiation damage experiment.

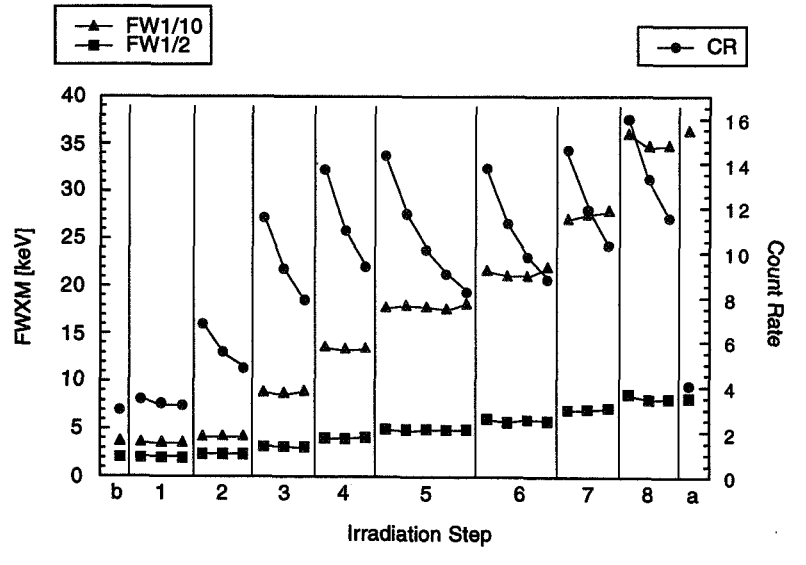

Fig. 2: Energy resolutions (FW1/10 and FW1/2) and count rates of detector FLIGHT after each incremental proton irradiation step (no. 1 to 8). Key: b = before irradiation, a = after last irradiation step.

In Fig. 2, the resolutions and the count rates of detector FLIGHT are presented as repetitive measurements after each incremental proton irradiation. The count rates decreased after each proton irradiation due to the decay of induced short-lived radio nuclides. In spite the fact that higher count rates improve the resolution of a damaged detector, the resolution was relative constant over a time frame of half an hour except for the step 7 and 8. This figure illustrates that the resolution measurements were rather reproduci-

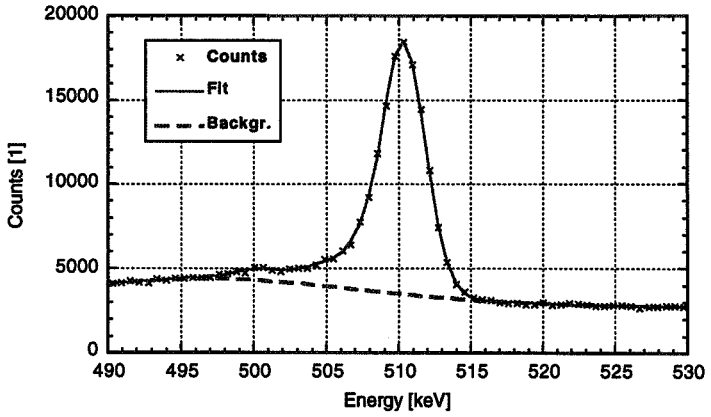

Fig. 3: MO GRS peak shape in early cruise phase (C3), ca. 1 month in space: almost symmetrical peak form.

ble within the relatively short measurement time. However, it should be mentioned, that resolution transients also can be observed if proper arrangements are taken and sufficient time after a proton irradiation are available. Transients can always be observed with radiation damaged detectors as a result of equilibrium processes of charged carrier (hole) trapping and detrapping [3].

In contrast to a rather fast radiation damaging process of detectors at an accelerator, the irradiation in space is very weak, but, also the induced gamma-ray flux on board of MO spacecraft was very low. Therefore, one had to sum many gamma-ray spectra taken over several days to check the performance of the MO detector. Fig. 3 shows a still symmetrical shape of the 511-keV peak after having been in space for a few weeks (launched on Sep. 25, 1992; accumulation of spectra lasted from Oct. 16 to Nov. 7, 1992): FW1/2 of 3.7 keV, FW1/5 of 6.2 keV, and asymmetry of 1.03.

After having been 7.5 months in space, many spectra were accumulated in the period from Jun. 10 to Aug. 1, 1993, by MO GRS. The energy resolution of the 511-keV line degraded to FW1/2 of 5.3 keV, FW1/5 of 12.5 keV, and asymmetry of 1.7, i.e. strong low-energy tailing, see Fig. 4. This tailing results from charge collection deficiency.

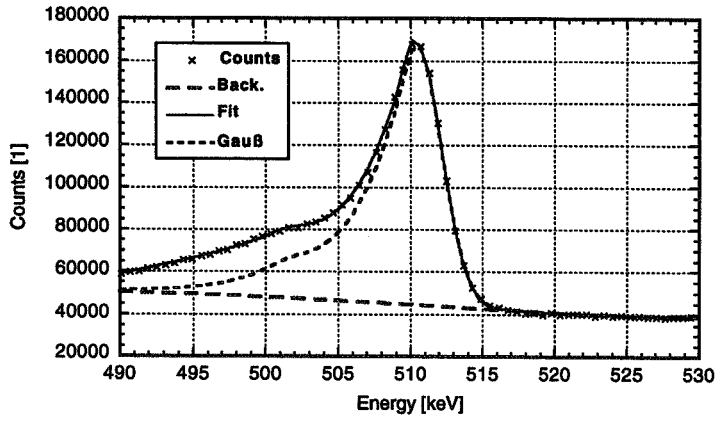

Fig. 4: MO GRS peak shape in late cruise phase (C11), ca. 7.5 months in space: strong low-energy tailing.

After the production of electron-hole pairs by absorption of a gamma-ray, applied bias (HV) separates the carriers according to their charge. In n-type detectors, holes travel to the outer electrode, while electrons to the inner. Measurements with damaged coaxial n- and p-type detectors revealed that holes are predominantly trapped by defect sites. Depending where in the detector volume the gamma-ray is absorbed, the holes have different

long paths to reach the electrode and their probability of being trapped increases with longer travel paths. Would a large majority of electrons also be trapped, the peak centroid would rapidly move to lower energies in contrast to what is observed: the peak centroid moves slightly to lower energies, while the low-energy shoulder spreads over a region those width is a function of received proton fluence. The combined effect produces peaks with increased FWHM and characteristic tailing, which is different for n- and p-type detectors [4]. This reduced sensitivity increases the detection limit, i.e. the ability of the instrument to detect a line in the general background; a fact that is counter productive to planetary gamma-ray spectroscopy.

Comparing the two detectors under the aspect of built-up of radiation damage and performance, they seemed to have had behaved in the same manner. An explicit analogy cannot be established as long as other parameters, such as temperature, high voltage, hole flux, etc., cannot be converted to one set of standard parameters that uniquely describes radiation damage and performance. The mean free path of holes, corrected for many external parameters, would be a step in the right direction.

References

[1] Boynton W. V., J. I. Trombka, W. C. Feldman, J. R. Arnold, P. A. J. Englert, A. E. Metzger, R. C. Reedy, S. W. Squyres, H. Wänke, S. H. Bailey, J. Brückner, J. L. Callas, D. M. Drake, P. Duke, L. G. Evans, E. L. Haines, F. C. McCloskey, H. Mills, C. Shinohara, and R. Starr (1992), "Science Applications of the Mars Observer Gamma Ray Spectrometer", J. Geophysical Research, Vol. 97, No. E5, 7681-7698, May 25.

[2] Brückner J., M. Körfer, H. Wänke, A. N. F. Schroeder, D. Filges, P. Dragovitsch, P. A. J. Englert, R. Starr , J. I. Trombka, I. Taylor, D. M. Drake, and E. R. Shunk (1991), "Proton-induced radiation damage in germanium detectors", IEEE Trans. Nucl. Sci., 38, pp. 209-217.

[3] Koenen M., J. Brückner, M. Körfer, I. Taylor, H. Wänke (1995), "Radiation Damage in Large-Volume N- and P-Type High-Purity Germanium Detectors Irradiated by 1.5 GeV Protons", IEEE Trans. Nucl. Sci., 42, pp. 653-658.

[4] Koenen M., J. Brückner, U. Fabian, H. Kruse, H. Wänke, A. N. F. Schroeder, R. Starr, L. G. Evans, J. I. Trombka, D. M. Drake, P. A. J. Englert, J. Dempsey (1996), "Analysis of Radiation Damaged HPGe Detectors with a new Algorithm", IEEE Trans. Nucl. Sci., 43, pp. 1570-1575.

Measurements of the Radiation Belts from MIR and STRV 1994-1997

P. Buhler, A. Zehnder, L. Desorgher , W. Hajdas, Paul Scherrer Institute, Switzerland
E. Daly, L. Adams, ESA/ESTEC, 2200 AG Noordwijk, The Netherlands

Introduction

High energy radiation belt particles are becoming a more serious threat to spacecraft and their payloads. Upsets in electronics, radiation background, degradation, electrostatic charging and astronaut hazard are among the effects. The need for small monitors is becoming clearer, both for better mapping of the environment and as an on-board resource for operations use and future mission planning purposes. The REMs on STRV are simple single shielded silicon diode detectors. Despite the problems of contamination and discrimination inherent in such devices, they are cheaper and easier to construct and accommodate than more discriminating, uncontaminated instruments. The results presented here from the REM instruments operating for almost 3 years in two very different orbits show that highly valuable results can be derived if care is taken with calibration and simulation. These data, and those expected from follow-on monitors will be a valuable data resource for modelling the radiation belts and monitoring the magnetospheric environment while many sensitive missions are flying, including space-based astronomy, communications constellations and the space station. Current static models are inadequate for many contemporary needs.

The Radiation Environment Monitor

REM has been built for monitoring the high energy particle environment on spacecraft. It accumulates energy transfer spectra of charged particles in two silicon detectors and is sensitive to protons in with energies E > 30 MeV and to electrons with energies E >1 MeV. The energy transfer spectra are accumulated for typically 100 sec (32 sec. on MIR) and binned into 16 detector channels. The main aperture of the instrument is defined by a cone of 45°. However, due to weight restrictions the surrounding shielding is not as high as ideally required. This allows protons to penetrate from the sides. For a full description of the instrument see Buhler et al., 1995.

A difficulty in building electron detectors is to prevent the count rates from becoming contaminated by high energy protons. Electrons in the MeV range deposit close to the minimum ionizing energy in silicon (~0.37 keV/micron) – the energy protons with E > 300 MeV deposit. Therefore from dE measurements alone these particles cannot be distinguished. This problem can be solved by using stacks of different detectors and active shielding, which complicates the system. The idea behind the construction of REM is to accept that electron channels can be contaminated by protons, but to measure the proton flux independently and to use this information to deduce the proton contribution in the electron channels. Therefore REM consists of two detectors. Each detector uses one silicon diode which is shielded by a spherical dome of a few mm aluminium. One detector is shielded with an additional layer of tantalum which lowers the penetration of MeV electrons considerably, although can not eliminate it totally. However, by using the simultaneous measurements of both detectors, information on the electron and proton fluxes can be gained. An important input for the spectral deconvolution of the measured

dE histograms are the energy-dependent geometric factors. Special efforts have been taken to determine the geometric factors of the REM detectors. The flight instruments have been calibrated with protons and electrons at various energies and in addition extensively numerically simulated, including realistic mass distribution models of the spacecraft.

The UK micro-satellite STRV-1B is in a Geostationary Transfer Orbit, GTO, with 250 km perigee, 36000km apogee, a 7° inclination, and a 10½ hr. period. An EVA in late 1994 was used to fix another model to the outside of the Russian space station Mir, which orbits the earth in a circular Low Earth Orbit, LEO (400 km, 51.6° inclination, 90 min period).

GTO Radiation Belt Measurements

We observe strong influences on the radiation belts by solar-heliospheric events. The period of time covered with REM measurements is in the declining phase of the solar 11-year activity cycle. Due to an absence of eruptive events, the solar wind arriving at the magnetopause is characterized by recurrent fast wind streams. We also see recurrent effects due to the 27-day solar rotation period. Figure 1 shows 1 MeV electron fluxes measured by REM on STRV-1B at L=4.5 as a function of time. The large flux peaks are associated with the occurrence of fast solar wind streams impinging on the earth's magnetosphere. The difference solstice an equinox periods can be accounted for by a semiannual variation of effectiveness of the solar-wind magnetosphere interaction.

Repeated rapid depletions and increases with a characteristic period of 27 days are clear. We see that the arrival of a fast solar wind stream at the earth first causes a depletion of the outer belt high energy electron population within about a day, followed by a rapid (~few days) increase where the level reached depends on the wind peak velocity. A slow decay then ensues. Figure 2 shows how the large electron injection of January 1997 was seen by the REM on STRV. Each panel represents half an orbit (~5¼ hrs.), either the inbound or outbound passage. The period before this event was extremely quiet, with essentially no outer zone. The build-up by over 4 orders of magnitude in a matter of hour is clear. The transport of the belt is also seen, but care must be taken because of aliasing of time and space variations. Figure 3 summarises the orbital dose measurements, emphasising the dynamicism of the electron environment.

MIR Low Altitude Measurements

The radiation environment of Mir is dominated by protons in the inner radiation belt. The largest proton fluxes are encountered around L=1.4 at low B values, in the South Atlantic anomaly. In Figure 4 the daily average dose measured in the SAA by Mir--REM is plotted versus time. In the same figure also the three month averaged 10.7 cm solar radio flux, $F_{10.7}A$ is shown. We use here the solar radio emission as measure for the solar EUV and X--ray emission which is responsible for the heating of the upper atmosphere. Around the middle of 1995 the SAA dose increased by 25%. At the same time the solar radio flux decreased by about the same factor. Calculations show that this decrease of heating power

causes a lowering of the atmospheric density in the SAA region by typically 20% which could be responsible for the enhanced SAA doses.

The atmosphere is also responsible for an anisotropy of the proton fluxes in the SAA. Large radius cyclotron motion of protons in the SAA, where the dip angle is ~50° means the guiding center of particles arriving from the east at the detector is below the point of observation, for particles arriving from the west it is above. Particles coming from east experience denser parts of the atmosphere than those from the west and will be more absorbed. The resulting difference between eastward and westward proton fluxes is called east--west effect [Heckman, 63]. On Mir the REM is shielded from the back by the massive space station. Thus sorting the observations by the orientation of the detectors with respect to the local magnetic field it was possible to measure the east--west effect [Buehler 96]. In Figure 5 Mir--REM count rates in the high energy proton channels at L=1.4 are plotted as function of B for eastward (asterisks) and westward (dots) orientation of the detectors, respectively. The average ratio between west and east is 4.3. Recently a model for the anisotropic proton flux has been included in ESA's radiation belt model software UNIRAD [Heynderickx, 96].

Conclusions

Many interesting features are observed by REMs on MIR and STRV. The January 1997 event is the subject of on-going study. Unique East-West asymmetry measurements have been made on MIR.

References

Heckman 1963: East-East Asymmetry in Flux of Mirroring Particles, J.Geophys.Res.68(8):2117

Buhler P. et al 1995: "The Radiation Environment Monitor" Nucl..Ins.Methods. 368:825

Buhler 1996: REM Measurements on-Board MIR in 1995, Cospar GA,1996, accepted Adv. Sp. Res.

Heynderickx et al, 1996: New Features and Models in UNIRAD, ESA Conf. Proceedings ESA-SP392

Fig. 1: 1 MeV electron dynamics

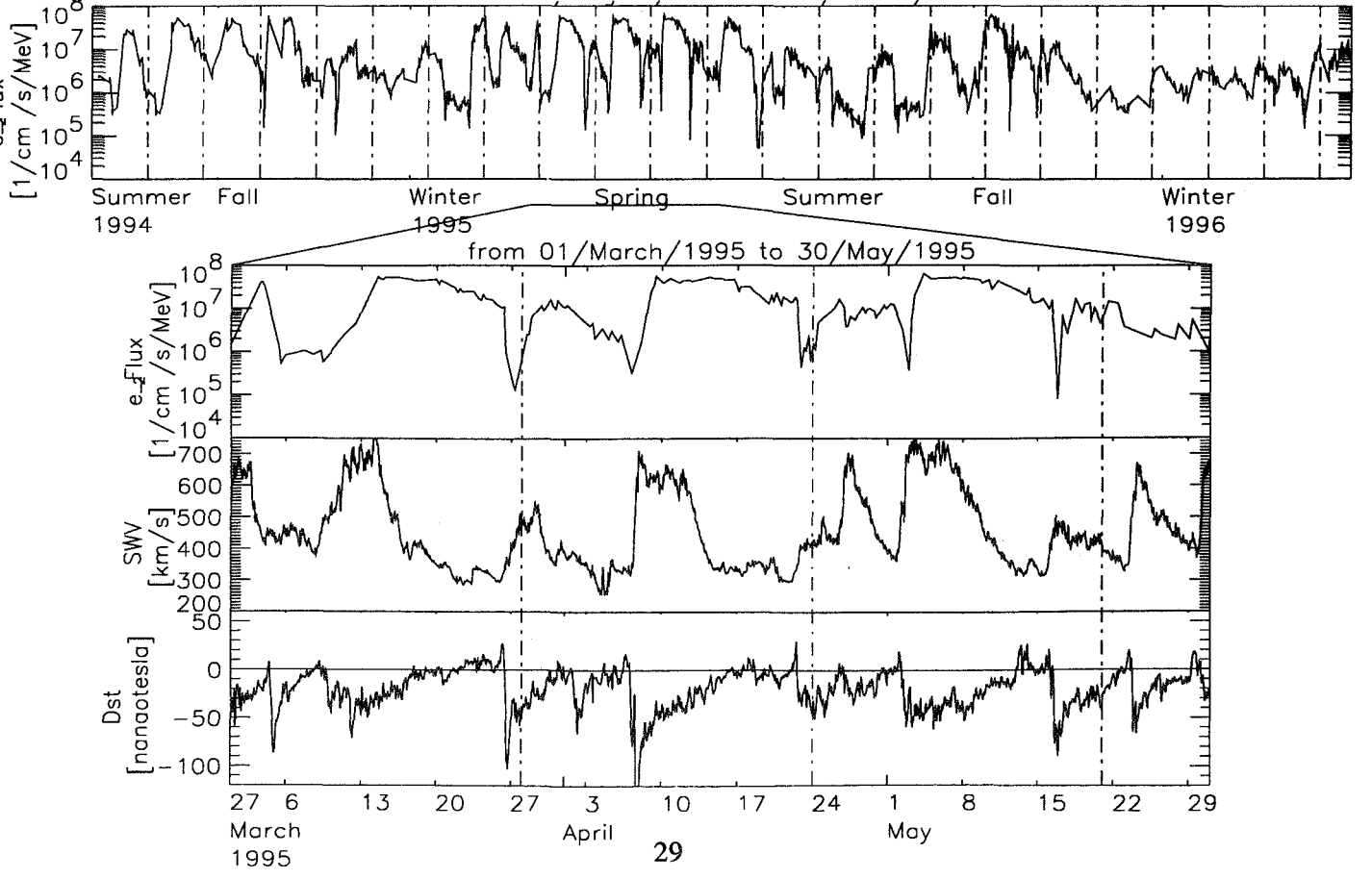

Fig. 2: The large electron event of Jan. 1997 as captured by STRV's REM

Fig. 3: Measured dose variations in GTO

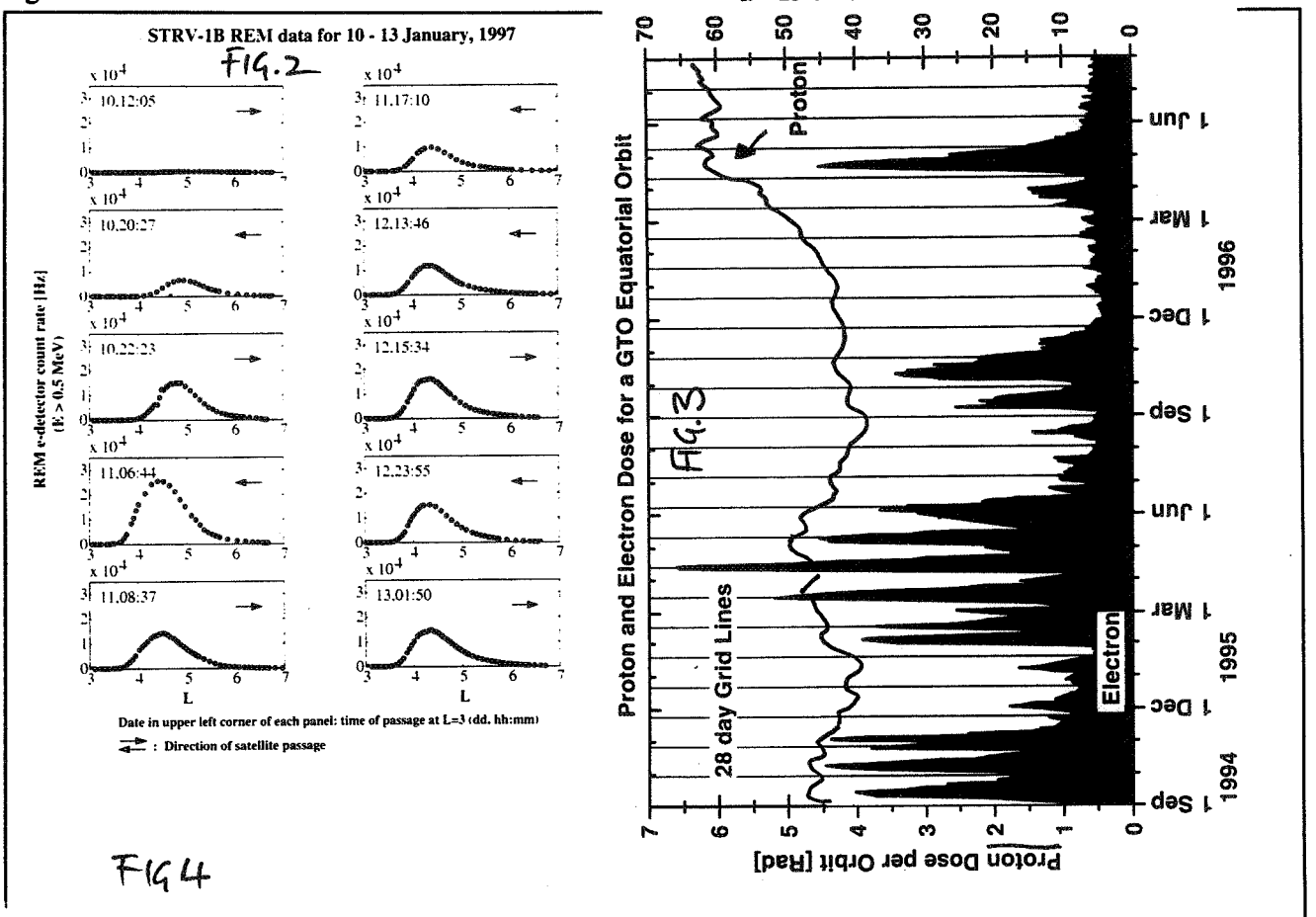

FIG 4

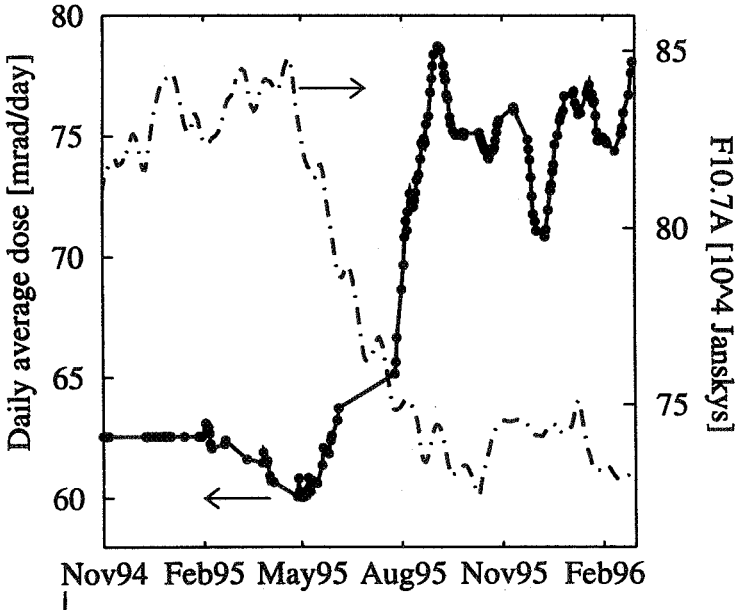

FIG 5

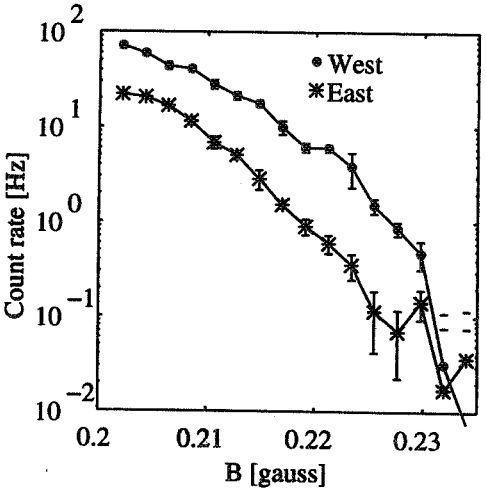

Fig. 4: Dose variations measured by the MIR along with solar flux variations

Fig. 5: East--west effect measured with Mir REM at L=1.4.

The Effectiveness of the Proportional Counter with a Specially Designed Filter as a Solar X-ray Monitor on the NEAR Mission

P.E. Clark
Catholic University of America, Washington DC
P.E. Clark, Catholic University of America, Washington DC

S.R. Floyd and J.I. Trombka
code 691, NASA/GSFC, Greenbelt, MD

The X-ray instrument package on the Near Earth Asteroid Rendezvous (NEAR) spacecraft is designed to provide direct measurements of the major elemental abundances for the asteroid 433 Eros. These will be the first such measurements ever made for a 'primitive' body. For this task to be performed, simultaneous measurements must be provided of both the X-ray lines characteristic of major elements at the asteroid's surface as well as the solar flux, which is the source of these lines (1,2). The solar flux consists of a continuum which is generated by thermal bremstrahlung and radiative recombination, with superimposed major lines which result from emission due to transitions in H and He-like ions. The relative contribution of each component of the solar flux varies as the level of solar output changes, and thus solar output must be monitored to correct for varations in surface data caused by the changing levels of solar output.

In order to accomplish this task, two solar monitors, using different technologies, were included as part of the experiment package (3). These monitors are designed to be able to operate over three orders of magnitude of solar output, and two to three orders of magnitude variation in the spectral intensity from 1 to 10 kev. One monitor, a detector type not previously flown on planetary missions, is a solid state PIN detector with a 1.2 square millimeter window. It was anticipated that the PIN detector would degrade with radiation exposure. Therefore, an anneal capability was built into this system and another solar monitor of different technology was included in the instrument package. This monitor, which is discussed in detail here, is a sealed, gas-filled proportional counter, similar to ones flown on previous planetary missions, but with an additional custom designed mask/filter. One of the challenges of the design process was to create a filter which would selectively enhance the higher energy spectrum, while retaining a sufficient portion of the lower energy spectrum. The filter, placed on the 25 square centimeter 1 mil thick Be window, consists of a sandwich of the following layers, centered from bottom to top:

a) 62.5 mils of Delren with a .01 square centimeter opening;

b) 4 mils of Beryllium with a .005 square centimeter hole over the Delren opening;

c) 15 mils of Al with a 1.5 by 1.5 centimeter hole, which effectively reduces the maximum useable window area to 2.25 square

centimeter by attenuation;

d) a 1 mil layer of kapton which acts as a thermal shield.

The filter effectively operates as a graded shield in two modes: the 'thinner', inner hole is sensitive to the lower energy spectrum which has an intrinsically higher flux. The small size of the inner hole reduces the contribution from this part of the spectrum, attenuating this portion of the spectrum sufficiently so that the detector is not saturated. A 'thicker', outer area, surrounded by the Alumimum shield effectively suppresses the lower energies while selectively enhancing the higher energies over a much larger effective window area. The resulting spectrum actually consists of a bimodal spectrum, with two components, one from each area of the window, superimposed on one another. The filter was designed to prevent saturation of the detector under all but the most active solar flare conditions. On the other hand, sufficient signal must be generated over the integration interval so that data is useable for removing solar variations from asteroid data. The limits were set at a maximum of 10000 counts per second to avoid degradation of the digital electronics, and a minimum of 10 counts per channel to get adequate spectral shape. One solar monitor may be operated at a time in one of two modes: either continuous operation of one monitor, or alternate operation of both monitors.

The NEAR spacecraft was launched in February of 1996, and is now in deep space 'cruise' mode on the way to the asteroid. We have been allowed to turn the instrument on periodically for calibration, and now have approximately 70 days worth of solar measurements. Despite the sun's quiescence during this time, which is near or at solar minimum, measurements have fortuitously been made during a few small flares. The 10 counts per channel limit has normally been met. Cosmic-ray induced backgrounds for the proportional counter have made determination of spectral shape difficult at times of lower solar output. On the other hand, although both detectors were initially assumed to have spectral resolutions of about 1 Kev at 5.9 Kev, the resolution of the PIN detector proven to be about a fact or two better, and actually has allowed the identification of discrete line structures (particularly Fe lines at 6.4 to 6.6 KeV) in the spectra for a few of the more energetic sub-flares detected. These structures are only marginally identifiable in proportional counter spectra, due to induced background.

The three proportional counters that are not sun-facing, and will eventually be asteroid-pointing, are used as indicators of cosmic-ray induced background, which has now been removed from spectra from the sun-facing proportional counter for a typical range of solar outputs. The resulting spectra have been correlated with Si PIN spectra. Differences in spectral shape and intensities are consistent with detector efficiency characteristics resulting from different external filters and internal cross-sections of the two detectors.

REFERENCES: (1) Adler and Trombka (1977) PHYS CHEM EARTH 10: 17-43; (2) Clark (1979) Chapter 6: In CORRECTION, CORRELATION, AND THEORETICAL CONSIDERATION OF LUNAR X-RAY FLUORESCENCE INTENSITY RATIOS. U. Maryland Diss; (3) Clark, Trombka, and Floyd (1995) LUN PLAN SCI XXVI, 253-254.

Page intentionally left blank

GAMMA-RADIATION BACKGROUND ONBOARD RUSSIAN ORBITAL STATIONS.

V.V. Dmitrenko, A.M. Galper, V.M. Gratchev, V.G. Kirillov-Ugryumov, S.V. Krivov, A.A. Moiseev, S.E. Ulin, Z.M. Uteshev, K.F. Vlasik, Yu.T. Yurkin.

Moscow Engineering and Physics State Institute,
31 Kashirskoe Shosse, Moscow 115409, Russia.

SUMMARY

Large manned space flight missions have several advantages for carrying out astrophysical and cosmic ray experiments, including the ability to install heavy instruments with large dimensions, increased electrical power and telemetry capacity, and the operation of fixed instruments by qualified personnel (astronauts).

The main disadvantage in the use of heavy orbital stations for these experiments is the high level of background radiation generated by the interaction of station material with primary cosmic rays, high energy particles that exist in the magnetosphere of Earth, and albedo radiation from Earth. In some cases, additional radiation may originate from man-made radiation sources installed at the stations.

For many years MEPhI have maintained experiments onboard manned Russian space flight missions to study primary gamma-rays at two energy intervals: 0.1 - 8 MeV [1] and 30-600 MeV [2] and electrons with energy more than 30 MeV [3]. During these experiments significant time was spent investigting high energy background radiation onboard the stations.

To measure 30-600 MeV gamma-rays, the gas-Cherenkov-scintillation telescope *Elena* [4] was used. The angular view of this telescope was 10°, with a geometrical factor of 0.5 cm^2sr. This telescope was operated onboard the orbital stations *Salyut-6* and *Salyut-7*. Usually these stations were operated together with the space missions *Soyuz* and *Progress*. For background measurements, cosmonauts installed the telescope at various locations on *Salyut, Soyuz* and *Progress*, and oriented it in various directions respectively to the station's axes. During these experiments, the orbital stations were not oriented.

The distribution of materials inside the station was very nonuniform. To differentiate the dependence effect of gamma-ray background from the mass we used "effective mass" along the axis of telescope:

$$M = \sum_{i=0}^{n} \int_{r_i}^{r_{i+1}} \frac{\rho_i}{r^2} dr,$$

where:

r_i- the distance from telescope to edge of i-layer material with the constant density;

ρ_i - density of i-layer material.

The data reduction of these measurements showed that the intensity of gamma-ray background with energy 30-600 MeV on the board of orbital complex "Salyut"-"Soyuz"-"Progress" during the flight at the altitude 300-350 km can be described by equation:

$$I_\gamma = (3.5 \pm 1.5) \cdot 10^6 \, R^{-(1.0\pm0.1)} \cdot E^{-(1.8\pm0.2)} \cdot M \, (m^2 \cdot s \cdot sr \cdot MeV)^{-1},$$

where:

E - energy of gamma-rays in MeV;

R - cut off of rigidity in GV

A special experiment on the orbital station *Salyut 7* was carried out to estimate the role of high energy neutrons for the generation of secondary gamma-rays with energy 30-600 MeV.

To make this measurements the lead disk with diameter 100 mm and thickness 12.6 mm surrounded by 10 mm scintillator was assembled in front of telescope "Elena" mentioned above [5]. The lead disk with the anticoincidence scintillator housing is a model of coded aperture unit which is often used for improving of angular resolution of gamma-telescopes.

The following table demonstrate how the additional flux of high-energy gamma-rays I_{add} generated at the lead plate depends from cut off of rigidity (two intervals: 2-8 GV and 8-16 GV) and from orientation of telescope (0°, 90°, 180°), where 0° - corresponds to zenith direction. Gamma-ray flux registrated without of lead disk in front of telescope "Elena" is I_0. It is mostly secondary gamma-rays generated at the material of station plus secondary gamma-rays from atmosphere and primary gamma-rays.

Table

θ degree	I_0 $(m^2 s\ sr)^{-1}$	I_{add} $(m^2 s\ sr)^{-1}$	I_0 $(m^2 s\ sr)^{-1}$	I_{add} $(m^2 s\ sr)^{-1}$
	R=2-8 GV	R=2-8 GV	R=8-16 GV	R=8-16 GV
0	22±6	43±21	12±5	11±11
90	174±51	74±7	84±39	52±16
180	152±19	88±29	71±20	48±11

The main process responsible for I_{add} is the interaction of high energy (E_n> 200 MeV) neutrons with the lead disk and accordingly generation of π^0 which give pairs of gamma-rays.

The measurements of gamma-rays background in the energy range 0.1- 8 MeV were carried out on the board of orbital station "Mir" (altitude ~ 400 km, inclination ~ 52 °). High pressure Xenon gamma-ray telescope "Ksenia" [6] was used for this purpose . This telescope has sensitive volume ~ 1 liter of Xenon with density ~ 0.5 g/cm^3 (pressure ~ 50 atm). This telescope was installed at the research module "Kristall". As this telescope had a very wide aperture ~ 3 π ster it meant that the telescope was measuring the secondary gamma-rays from significant part of orbital station "Mir". It was shown that the gamma-ray background with the energy 0.1- 8 MeV on the orbital station "Mir" in few times higher than the flux of the secondary atmospheric gamma-rays with the same energy at 3.5 g/cm^2 of residual atmosphere for the vertical direction [7]. The flux of gamma-ray background on the surface of "Appolo" at the almost same energy range is very close to the background registrated on the orbital station "Mir".

The dependence of the gamma-ray flux on the orbital station "Mir" from latitude follows the similar dependence of primary cosmic rays. Atmospheric gamma-line with energy 511 keV is very well recognizable at these background spectra.

Unpredicted bump at the energy range 170-260 keV was discovered during some measurements. The analysis of behavior of this bump for different position of mission "Soyuz" relatively to orbital station "Mir" allows to conclude that the nuclear source is located at this mission. The intensity in the energy range 170-260 keV with this mane-made source was 2-3 times higher than without this source [7]. This source is the Cs^{137} at the Uranium dome. It is used for soft landing of missions.

The detailed measurements of gamma-radiation background at the heavy orbital stations show that these missions are not good objects for astrophysical and cosmic-ray experiments. The gamma-ray background is too high to make this kind of experiments fruitful, although the measurements of gamma-ray bursts, sun flares and another transient events can be carried out successfully.

References

[1] Bolotnikov A.E., Chernisheva I.V., Dmitrenko V.V. et al., 23 Intern. Cosmic Ray Conf., 1(1993) 109. [2] Galper A.M., Gratchev V.M., Dmitrenko V.V. et al., Izv. Akad. Nauk. SSSR Ser.Fiz., 34 (1970) 2275.
[3] Galper A.M. , Gratchev V.M. , Dmitrenko V. V. et al. , Pisma v Journal Experimentalnoy i Teoreticheskoi Fiziki, 38 (1983) 409.
[4] Galper A.M., Gratchev V.M., Dmitrenko V.V. et al., 17 Intern. Cosmic Ray Conf., 10 (1981) 262.
[5] Aleksandrov A.P., Berezovoy A.N., Galper A.M. et al., Kosmicheskie Issledovania, 22 (1984) 950.
[6] Bolotnikov A.E., Chernisheva I.K., Dmitrenko V.V. et al., Intern. Conf. of Liquid Radiation Detectors, Tokyo, 710 April, (1992) 462.
[7] Galper A.M., Gratchev V.M., Dmitrenko V.V. et al., Kosmicheskie Issledovania, 33 (1995) 1.

Page intentionally left blank

NEW HIGH ENERGY ELECTRON COMPONENT OF EARTH RADIATION BELT

V.V.Dmitrenko, A.M.Galper, V.M.Gratchev, V.G.Kirillov-Ugryumov, S.E.Ulin, S.A.Voronov.

Moscow Engineering and Physics State Institute
31 Kashirskoe shosse, Moscow 115409, Russia

SUMMARY

The Earth Radiation Belt (ERB) was discovered in the course of the first flights of Russian and American satellites with conventional instruments (gas discharge and scintillation counters), which made it possible to investigate many characteristics of trapped particles and simulate adequate radiation belt models [1,2]. However, the experimental and theoretical evidence accumulated over recent time, needs more elaborate measurements for its interpretation. These measurements became feasible after the development of devices based on more perfect detectors (solid and gas-filled Cherenkov detectors, magnetic spectrometer, scintillation time-of-flight systems).

The evidence requiring new direct measurements in the ERB was obtained in the late 1960s in the course of balloon flights carried out by Cosmophysics Laboratory of the Moscow Engineering and Physics Institute. In these flights a correlation between the high energy electron flux in the upper atmosphere and perturbations of the Earth's magnetosphere was established [3,4].

This phenomenon could be explained assuming there exist high energy electron fluxes in the ERB. High energy electron fluxes in the ERB were recorded for the first time in the direct experiments carried out on board orbital station "Salyut-6" [5,6] (orbit altitude - 350 km, inclination 51.6°). A scintillation-Cherenkov telescope "Elena" controlled by cosmonauts was preset to different programmed positions. The measurements were made in the periphery of the ERB, namely, in the part which goes as low as several hundred km in the Brazil Anomaly Region (BRA). The flux of electrons with energies above 30 MeV was up to 10^4 $(m^2 s\ sr)^{-1}$.

A more detailed study of the trapped electrons was undertaken with "Intercosmos-Bulgaria-1300" satellite, the orbit altitude and the inclination being ~ 900 km and 81°, respectively. The instrument axis in this case was perpendicular to the orbit plane. A scintillation-Cherenkov telescope, "Electron", with parameters similar to that of "Elena" was used. Geometry factors of both the instruments were about 0,5 $cm^2 sr$, the threshold electron energy was $\geq$ 30 MeV for "Elena" and $\geq$ 20 MeV for "Electron".

Energetic electrons in ERB were recorded because of the fact that the "Elena" and Electron telescopes have a low sensitivity to the proton background and a narrow acceptance aperture thanks to the gas-filled Cherenkov counters. Both devices have a similar scheme but "Elena" has an anticoincidence counter and a converter installed in the part of the device for gamma-quanta recording. The device consists of 6 scintillators and a gas Cherenkov counter Ch, which is filled with SF_6 up to 6 atm and has a threshold Lorentz-factor ~ 11. While in channels with Ch counter the electrons are separated from the protons only by the gas Cherenkov counter which eliminates the protons with energy $\leq$ 10 GeV in channel with anticoincidence scintillation counters, besides this their separation is based on the fact that electrons and protons have different transmissions through lead absorbers Pb_1 and Pb_2.

The third stage of the study of electron component was principle new one. A new type of the instrument was developed in 1985: the time-of-flight magnetic spectrometer "Maria". This instrument was delivered on the board of orbital station "Salyut-7". At first time a magnetic spectrometer is used outside atmosphere for separate observation of high energy (20-200 MeV) electrons and positrons[7]

It should be mentioned that the main characteristics of all above listed devices were examined at different accelerators in proton and electron beams and in a beam of tagged gamma-quanta and at neutron

reactor [8,9]. The generalized parameters of the devices were calculated by the Monte Carlo method during computer simulation.

The experimental data on flux of electrons and positrons are obtained in a wide enough range of latitude, longitudes and altitude (wide range of B, L). Some results indicating the existence of a stable belt of high energy trapped electrons are discussed here.

1. Obtained with various instruments spatial distribution of trapped electrons flux at different altitudes and temporal intervals agree among themselves and show that the trapped electrons concentrate on the L = 1.1-1.8 and have intensity of flux more than $10^4 (m^2\ s\ sr)^{-1}$[10].

2. Measured charge ratio between electrons and positrons demonstrates that the flux of trapped particle are mainly electrons and largely determines the choice between various origin of trapped flux.

3. The total energy spectra of trapped (pitch-angle more than 70°) electrons and positrons in energy range 20-200 Mev confirm the practical absence of trapped positrons in measured flux of positrons and electrons. Estimation of the proton contribution to the given spectra is not more than 10 %.

Nowadays there are several models of high energy electrons origination in ERB : acceleration processes on various type of plasma fluctuation [11], radial diffusion [12], high energy electrons from interactions between the trapped belt's protons and the residual atmosphere [13], between primary cosmic ray nuclei and the residual atmosphere of the Earth and from high energy albedo neutrons. The choice between models, applying on the explanation of this phenomenon should base on listed experimental data.

The obtained results of experimental research indicate that:

- there is a stationary flux of electrons trapped by magnetic field of the Earth with energy range from 20 up to 200 MeV;
- the flux of trapped electrons locates on magnetic shells L = 1,1-1,8;
- its absolute intensity can exceeds $10^4\ (m^2 s\ sr)^{-1}$;
- hence, the flux of trapped electrons is a significant part of trapped protons with the same penetration ability (several percents in the center of BAR and much more value on its boundary).

Of course, for complete understanding of a physical nature of a stationary belt of high energy trapped electrons it is necessary to continue as experimental as theoretical researches. But now it's obviously that available model of the Earth Radiation Belt must be completed with new experimental data on electrons with energy more than 10 MeV and it is necessary to take into account this new component of ERB for background and radioactive doses estimation and simulation during cosmic research.

References

[1] S.N.Vernov, A.E.Chudakov, I.V.Vakulov et al., Izv. Akad. Nauk SSSR. Ser. Fiz., 28 (1964) 2058.
[2] V.Hess. The radiation belt and the magnetosphere. Atomizdat, Moscow, 1972.
[3] A.M.Galper and B.I.Luchkov. Trudi YI Vsesojuznoi eshegodnoi zimney shkoli po kosmophysike. Izd.Kol'skogo filials A.N., SSSR, Appatiti (1969).
[4] A.M.Galper, V.V.Dmitrenko, V.G.Kirillov-Ugryumov et al. Izv.Akad.Nauk. SSSR, Ser.Fiz. 34 (1970) 2275.
[5] A.M.Galper, V.M.Gratchev, V.V.Dmiternko et al. Izvestya Akademii Nauk, Ser.Fiz., SSSR, 45 (1981) 637.
[6] A.M.Galper, V.M.Gratchev, V.V.Dmiternko et al., Kosmich issledov.,19 (1981) 645.
[7] A.M.Galper, S.A.Voronov et al., Pribory I Technika Experimenta №2 (1986) 35.
[8] A.M.Galper, V.M.Gratchev, V.V.Dmitrenko et al., Preprint ITEF, №145 (Moskva, 1982).
[9] A.M.Galper, V.M.Gratchev, V.V.Dmitrenko et al.,Sb. Elementarnye chastisi I kosmicheskie izlucheniy (Energoizdat, Moskva,1982) p.26
[10] A.M.Galper, V.M.Gratchev, V.V.Dmitrenko et al., Pisma v Journal Teoreticheskoi i Experimentalnoi Fiziki, 38 (1983) 409.
[11] V.N. Tsytovich. Geomagnetism i Aeronomia, 3 (1963) 616.
[12] V.V.Dmitrenko, B.A.Tverskoi, V.B.Komarov. Kosmicheskie issledovania, 31 (1993) 83.
[13] A.A.Gusev, G.A.Pugacheva. Geomagnetism i aeronomia 23 (1982) 912.

Page intentionally left blank

COMPARISON BETWEEN PREDICTIONS & OBSERVATIONS OF INDUCED RADIOACTIVE BACKGROUND IN INTERPLANETARY MISSIONS

Clive Dyer, Peter Truscott, Howard Evans
Space Department, DERA Farnborough,
Hants GU14 0LX, England

Larry Evans,
Computer Sciences Corporation, Science Programs,
Lanham-Seabrook, MD 20706, USA

Jacob Trombka
Code 691, NASA/Goddard Space Flight Center,
Greenbelt, MD 20771, USA

SUMMARY

I. INTRODUCTION

Radioactivity induced in detector materials and their immediate surroundings is the major source of discrete-line, gamma-ray background and an important source of continuum background in the performance of remote-sensing, gamma-ray spectroscopy of planetary bodies. In interplanetary space the dominant sources of particles are cosmic rays and their secondaries arising from interactions with the spacecraft and the surface of the target body. In addition, certain future gamma-ray astronomy missions, such as INTEGRAL, are to be located so as to perform their observations in interplanetary space rather than in the traditional low earth orbits. Such location removes contributions from the earth's atmosphere and inner radiation belt at the expense of increased exposure to cosmic rays and solar particle events. Accurate prediction of the activation of key materials by cosmic rays is of the utmost importance for detector design and data interpretation.

II. CALCULATIONS

Over a number of years, an evolving series of calculations has been performed. These were initially based on semi-empirical spallation cross-sections and Monte-Carlo simulations of response functions and this technique was successfully employed to interpret the data from gamma-ray spectrometers carried on the OSO 7-8 and Apollo 15-17 missions [1]. In addition, this technique was used to predict the background to be expected in germanium spectrometers [2]. Unfortunately data for comparison has been long awaited but was in part realised by the data obtained during the interplanetary cruise phase of the Mars Observer [3]. Predictions can also be based on ground irradiation data [4].

More recently the Integrated Radiation Transport Suite (IRTS) has been applied to make successful predictions of the radioactive background observed in the Oriented Scintillation Spectrometer Experiment carried on the Compton Gamma Ray Observatory [5] and to interpret the data obtained from a variety of scintillator materials carried on the Space Shuttle [6]. In both cases the enhancement in radioactivity due to secondary neutrons is extremely important, providing a factor 20 for CGRO and 3 for shuttle. One of the new materials extensively studied in the shuttle flights, as well as by ground irradiations, is bismuth germanate [7]. Predictions for this material are thus available for comparison with current (NEAR) and future (INTEGRAL and Lunar Prospector) missions.

©British Crown Copyright 1997/DERA
Published with the permission of Her Britannic Majesty's Stationery Office

III. OBSERVATIONS

A. MARS OBSERVER

Although the Mars Observer was lost prior to insertion into Mars orbit, several periods of background data were obtained during the interplanetary cruise phase. Details of the gamma-ray spectrometer and the background data are presented in a companion paper [3]. The essential features to note here are that the spectrometer comprised an intrinsic germanium crystal of diameter and height 55mm, surrounded by a plastic, particle-anticoincidence mantle, while the housing to the detector container was largely titanium. By means of a boom the assembly was positioned at 1 metre from the spacecraft in order to reduce the background from spacecraft emissions. The background data set to be examined here comprised 2.6 million seconds obtained between 10 June and 20 August 1993, some 8 to 10 months after launch and a considerable time after the October 1992 solar particle event which produced a small background increase. Hence the observations are essentially of activation in equilibrium with cosmic rays.

B. NEAR

The Near Earth Asteroid Rendezvous mission was launched in February 1996 and will orbit the asteroid 433 EROS in 1999. Amongst the complement of instruments is a gamma-ray spectrometer comprising a central cylindrical crystal of sodium iodide, 25.4mm in diameter and 76.2mm in length inside a cup shield of bismuth germanate of outer diameter 89mm. A description of the instrument and modes of operation is given in [8]. Activation data are obtainable from the raw BGO counts, from the NaI in anticoincidence with the BGO, and from NaI in coincidence with 0.511 MeV in the BGO or 1.022 MeV in the BGO. During the interplanetary cruise phase there are occasional periods of operation, enabling the background to be obtained. The early data presented here were obtained in April 1996. By the time of the conference additional accumulation periods will have been added.

C. LUNAR PROSPECTOR

This spacecraft is scheduled for launch into a lunar polar orbit in October 1997. A gamma-ray spectrometer will be carried on a 1.9m boom and comprises a cylindrical BGO crystal of diameter and height both 76.2mm, within a plastic anticoincidence shield which is boron-loaded in order to serve additionally as a neutron detector [9]. No flight data will be available in time for the conference but predictions will be made based on calculations and ground irradiations.

IV. COMPARISONS

A. MARS OBSERVER

Some examples of the strongest lines observed in the backgound spectrum are given in Table 1 together with predictions for spallation products produced in a 55mm Ge crystal in a cosmic-ray flux of 3 cm^{-2} s^{-1}. A full list will be given at the conference and in the final paper. In general there is good agreement to within a factor of two. For ^{71m}Ge there is a probable contribution from secondary neutrons including capture, which are not included in the calculation. The 1157 keV line from ^{44}Sc is probably produced in the titanium housing. Although this nuclide is generated within the germanium at a level of 3.6 per minute, the predicxted line at 1160 from electron capture has a low branching ratio. The branch in coincidence with beta-plus decay is smeared out internally but would feature strongly in the escaping spectrum.

C. LUNAR PROSPECTOR

The internal spectrum of activation in a 76.2mm BGO crystal has been predicted for an incident cosmic ray flux of 1 cm^{-2} s^{-1} using the IRTS, and the build-up between 10 minutes and 2 years of flight is shown in the curves of Figure 2. Multiplication by the cosmic-ray flux to be expected in late 1997 (approximately a factor 4) gives the predicted activation background for the Lunar Prospector.

V. REFERENCES

[1] C S Dyer, J I Trombka, S M Seltzer and L G Evans,"Calculation of radioactivity induced in gamma-ray spectrometers during spaceflight," Nuc. Inst. and Meths., 173, pp 585-601, 1980.

[2] C S Dyer,"Calculation of energy deposition spectra for radioactivity induced in germanium gamma-ray spectrometers by various space environments," IEEE Trans. Nuc. Sci., NS-31, 6, pp 1061-1065, dec 1984.

[3] W V Boynton et al., this conference.

[4] A K Entwhistle, C S Dyer, J J Quenby, A J Evans, M Joshi,"Measurement of neutron and proton induced background for germanium gamma-ray spectrometers for use in a space environment," Journal of Physics E: Scientific Instruments, 22, pp601-611, 1989.

[5] C S Dyer, P R Truscott, H E Evans, N Hammond, C Comber, S Battersby, "Calculations and observations of induced radioactivity in spaceborne materials," IEEE Trans. Nuc. Sci. NS-41, 3, pp 438-444, June 1994.

[6] P R Truscott, H E Evans, C S Dyer, C L Peerless, J C Flatman, P Knight, C Moss, "Comparison of activation effects in gamma-ray detector materials," IEEE Trans. Nuc. Sci., NS-43, 3, pp 1510-1515, June 1996.

[7] P R Truscott, C S Dyer, P S Haskins, J E McKisson,"Activation of spaceborne bismuth germanate gamma-ray detectors," IEEE Trans. Nuc. Sci., NS-42, 4, pp 946-955, Aug 1995.

[8] L G Evans, R Starr, J I Trombka, J Bruckner, S H Bailey, J Goldsten, R McNutt,"Performance of the gamma-ray detector system for the NEAR mission and application to future missions," Proceedings of the IAA Second International Conference on Low-Cost Planetary Missions (IAA L-0905P), April 1996.

[9] W C Feldman, A B Binder, G S Hubbard, R E McMurray,Jr., M C Miller, T H Prettyman, LPS XXVII, p 355, 1996.

[10] P R Truscott and C S Dyer, "Induced radioactive background in space-borne gamma-ray detector materials," Proceedings of the INTEGRAL Workshop, St Malo France, Sept 1996.

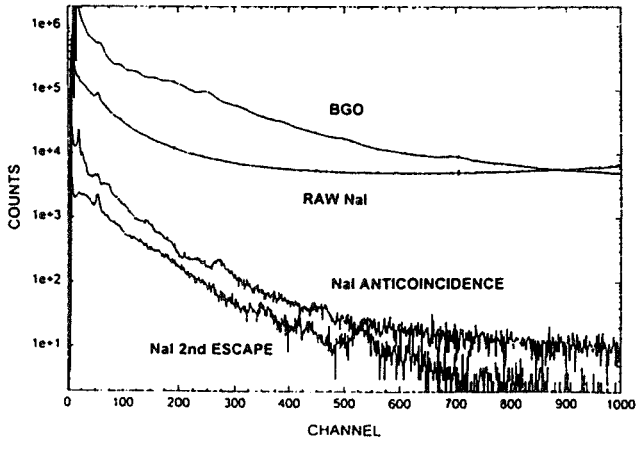

FIG.1 Energy deposition spectra in NEAR GRS 2 months after launch

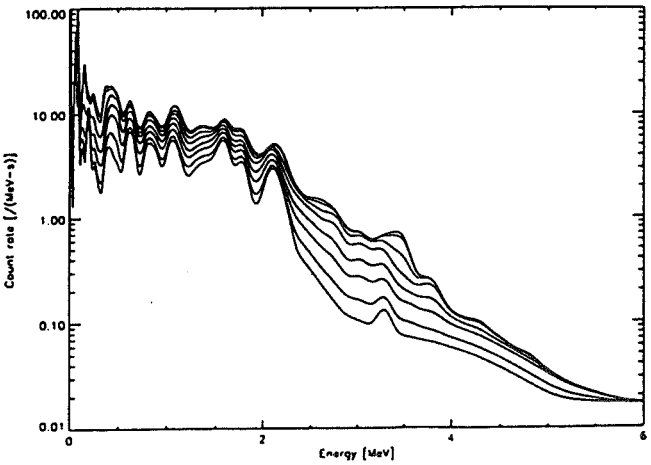

FIG.2 Predicted build-up of BGO activation for Lunar Prospector under unit cosmic ray flux

TABLE 1

Line Energy keV	Nuclide	Half-Life	Observed count rate per minute	Predicted count rate per minute	Comment
194	^{67}Ga	78 h	4.6	2.8	
198	^{71m}Ge	20 ms	31.0	7.8	Secondary production
271	^{44m}Sc	2.4 d	1.2	1.2	
439	^{69m}Zn	14 h	2.4	1.7	
583	^{69}Ge	38 h	0.8	0.3	
1049	^{66}Ga	9.4 h	0.3	0.3	
1117	^{69}Ge	38 h	1.0	0.4	
1157	^{44}Sc	3.9 h	0.6	0.03	Possibly Ti housing

B. NEAR

The first background accumulation was taken over a 48 hour period on 15 April 1996, some 60 days after launch, and the various spectra are presented in Figure 1. Strong features at around channels 54 and 458 are ascribed to the annihilation line (511 keV) and carbon excitation line (4430 keV) respectively and are used to improve the calibration. Some of the strong features observed in the sodium iodide spectrum in anticoincidence with the BGO are presented in Table 2, together with identifications. The usual strong features from sodium iodide activation products [1] (eg iodine-123,124,126) are seen, together with escape lines from BGO [7,10]. By the time of the conference quantitative comparisons will be made.

TABLE 2

Channel	Energy keV	Possible Nuclide A	Line Energy A	Possible Nuclide B	Line Energy B
16	142	^{206m}Bi	140	^{75m}Ge	140
19	175	^{71m}Ge	175	^{198}Pb	173
26	242	^{198m}Bi	249	^{127}Xe	236
31	294	^{121m}Te	294	^{198}Pb	291
47	449	^{111}In	443		
65	622	^{124}I	635		
73	697	^{126}I	698		
143	1374	^{124}I	1357		
151	1457	^{126}I	1452		

Continuum Background in Space-Borne Gamma-Ray Detectors

Larry G. Evans[1], Jacob I. Trombka[2], Richard Starr[3], William V. Boynton[4] and S. Bailey[4]
1.Computer Sciences Corporation, Science Programs, Lanham-Seabrook MD 20706
2.NASA Goddard Space Flight Center, Code 691, Greenbelt, MD 20771
3.The Catholic University of America, Department of Physics, Washington, DC 20064
4. University of Arizona, Lunar and Planetary Laboratory, Tucson, AZ 85721

I. INTRODUCTION

The background measured with space-borne gamma-ray spectrometers (GRS) in the 100 keV-10 MeV energy region consists of both discrete lines and continuum. The discrete lines originate in the decay of radioactive species. The continuum originates from a number of different processes and can be an important factor in the detection, for example, of weak gamma-ray lines from a planetary surface. Measurements of the gamma-ray background have been made during the cruise portion of a number of planetary missions. The three missions described here are the Apollo 15 and 16 missions each of which carried a 7 cm X 7 cm NaI scintillation detector, the Mars Observer (MO) mission which used a 5.5 cm X 5.5 cm high-purity germanium (HPGe) detector, and the Near Earth Rendezvous Asteroid (NEAR) mission that has a 2.54 cm X 7.6 cm NaI detector. A comparison of the intensity and spectral shape of these background spectra can be useful to help understand how these backgrounds vary with spacecraft size, detector position, and detector size. The use of shields to reduce the background components on these three missions is a test of the effectiveness of different shield designs.

II. BACKGROUND COMPONENTS

A detailed study of the backgrounds measured during the Apollo GRS experiments identified these major components in the cruise phase [1]: (1) direct charged-particle interactions, (2) natural radioactivity in the materials surrounding the detector, (3) gamma-rays due to cosmic-ray interactions in the spacecraft, (4) electron bremsstrahlung in the materials surrounding the detector, (5) cosmic-ray induced radioactivity in the detector, (6) secondary neutron induced radioactivity in the detector, (7) radioactivity induced in materials surrounding the detector, and (8) the cosmic gamma-ray spectrum. On Apollo, the most important background components were: at low energies (< 1 MeV) the cosmic gamma-rays and those from the spacecraft; at medium energies (1-5 MeV) the bremsstrahlung and cosmic rays; and at higher energies (>5 MeV) the spacecraft and bremsstrahlung. However, these results may be directly applicable only to the Apollo data since the size and mass of the spacecraft can have a significant effect on the intensities of many of the background components.

To reduce some of these background components, each of the three planetary GRS used a shield to reduce, among other things the charged particle background. Since each of these shields is of a different design, first the measurements without using the shield will be reviewed. Also, the Apollo and MO detectors were placed on booms to reduce the spacecraft contribution by moving the detector away from the spacecraft. However, only for Apollo were measurements made with the detector at the fully deployed position and at intermediate positions. MO measurements were only made at the first deployed position (approximately 1 m). The NEAR detector is body mounted directly onto the spacecraft. A comparison of the background measurements for Apollo (at 1 m from the spacecraft), for MO, and for NEAR are shown in Figure 1. To account for the different detector sizes, the count rate is normalized by the area of each detector. All three spectra have some similar features. Each spectrum decreases with increasing energy up to about 5 MeV. Above 5 MeV, each spectrum flattens out, except for the NEAR which increases in intensity between 5 and 10 MeV. Models of the background components indicate that the charged particle background

probably accounts for this increase in intensity with energy. Measurements made with the charged particle interactions excluded, described below, seem to confirm this identification.

III. SHIELDS

Because of the importance of discrete gamma rays in the energy range 5-10 MeV for planetary missions, the Apollo GRS included an anti-coincidence (AC) shield to reject interactions in the central detector due to charged particles. The effectiveness of the AC shield was tested periodically by inhibiting the electronic rejection of charged particles. Figure 2 shows two Apollo cruise spectra, one with the AC-on and the other with the AC-off. A comparison of the two indicates a reduction in the background continuum of a factor of 8 at 5 MeV and greater than a factor of 20 at 10 MeV. The Apollo AC shield consisted of a cylinder of plastic, 1 cm thick, completely surrounding the NaI detector, except in the direction where the photo multiplier (PMT) was located [2]. The small inefficiency measured in the AC-on spectrum resulted from both occasional unfavorable particle paths from which insufficient light was produced in the shield and from the open end of the plastic shield that might allow a small fraction of the charged particles to stop in the crystal without triggering an anticoincidence pulse [3].

The MO mission also used plastic as an AC shield and also as a neutron detector [4]. The necessity for cooling HPGe detectors required the use of a radiative cooler subsystem for MO. The passive V-groove cooler design had the AC shield located outside of the cooler vanes at some distance from the central detector. The AC-on and AC-off spectra for MO are shown in Figure 3. Only limited data was taken during cruise with the AC off and the resulting spectra had such large fluctuations that when plotted with the AC-on spectrum, the latter could not be seen. Therefore, smoothing was done on the AC-off spectrum to reduce the statistical fluctuations and so both spectra could be identified on a single plot. The reduction of continuum in the MO measurements were about a factor of 2 at 5 MeV and a factor of 3 at 10 MeV. This reduction is significantly less than that measured on Apollo, and was also less than that measured in the laboratory during calibration. The cause of this poor background reduction is possibly related to either the geometric relationship between the shield and the detector or the some inefficiencies in the flight electronics or both.

The NEAR system was designed to be mounted directly on the spacecraft and required a shield, not only to reduce the charged particle background, but to reduce the background signal from the spacecraft [5]. Bismuth Germanate (BGO) was used as the shield material. In addition to reducing the two background components, the BGO was also used to reduce the Compton continuum due to incomplete absorption in the central detector. The design of the NEAR system included 2.5-3 cm of BGO completely surrounding the central NaI detector, except in the viewing direction [6]. The flight measurements are shown in Figure 4. Reduction of continuum is substantially greater due to the Compton reduction; a factor of about 175 at 5 MeV and about 700 at 10 MeV.

IV CONCLUSIONS

It has long been suggested that a heavy spacecraft produces substantial hard photon continuum and secondary neutrons that are difficult to shield against [1], therefore requiring a boom to move the detector away from the spacecraft. This difference can be seen in the Apollo and MO background taken at approximately the same distance from the spacecraft. Restraints on mass in the future Discovery missions may often preclude the use of booms. The body mounted NEAR detector has a background continuum (AC-off) higher than either Apollo or MO. However, the use of the BGO shield reduces this background continuum to levels less than that of Apollo, even at the fully extended position and that expected for MO if it had been deployed to its maximum distance. Reductions in continuum of this magnitude along with separation of full-energy spectra from first and second escape peak spectra [6] are expected to allow the

NEAR mission GRS to achieve sensitivities, while not as good as a HPGe detector system, sufficient to achieve the scientific objectives of the mission [5].

Measurements of the effectiveness of AC shields in conjunction with passively cooled HPGe detectors, such as MO, indicate that these shields may be much less effective than either Apollo or NEAR in reducing the high-energy background. An issue for future planetary missions, such as Mars Surveyor 2001, is whether this modest improvement in continuum reduction measured on MO is worth the effort and cost in designing an AC shield that is compatible with the cooler design and does not compromise the low temperature that can be reached without the shield.

It should be noted that while this discussion considered the continuum background during cruise, the majority of the background component expected during orbital mapping around a solid body will come from scattering and other interactions in the topmost surface materials which is not affected by the detector design. On Apollo this component made up over half the continuum measured around the moon [7].

V. REFERENCES

1. C. S. Dyer, J. I. Trombka, S. M. Seltzer, and L. G. Evans, "Calculation of radioactivity induced in gamma-ray spectrometers during spaceflight", Nucl. Inst. and Meth., *173*, pp 585-601, 1980.
2. T. M. Harrington, J. H. Marshall, J. R. Arnold, L. E. Peterson, J. I. Trombka, and A. E. Metzger, "The Apollo gamma-ray spectrometer", Nucl. Inst. and Meth., *118*, pp 401-411, 1974.
3. J. I. Trombka, C. S. Dyer, L. G. Evans, M. J. Bielefeld, S. M. Seltzer, and A. E. Metzger, "Reanalysis of the Apollo cosmic gamma-ray spectrum in the 0.3 to 10 MeV energy region", Astrophys. J., *212*, pp 925-935, 1977.
4. W. V. Boynton, J. I. Trombka, W. C. Feldman, J. R. Arnold, P. A. J. Englert, A. E. Metzger, R. C. Reedy, S. W. Squyres, H. Wanke, S. H. Bailey, J. Bruckner, J. L. Callas, D. M. Drake, P. Duke, L. G. Evans, E. L. Haines, F. C. McCloskey, H. Mills, C. Shinohara, and R. Starr, "Science applications of the Mars observer gamma-ray spectrometer", J. Geop. Res., *97*, pp 7681-7698, 1992.
5. J. I. Trombka, S. R. Floyd, W. V. Boynton, S. Bailey, J. Bruckner, S. W. Squyres, L. G. Evans, P. E. Clark, R. Starr, E. Fiore, R. Gold, J. Goldsten, and R. McNutt, " Compositional mapping with the NEAR x-ray/gamma-ray spectrometer", J. Geophys. Res., in press, 1997.
6. L. G. Evans, R. Starr, J. I. Trombka, J. Bruckner, S. Bailey, W. V. Boynton, J. Goldsten, and R. McNutt, "Performance of the gamma-ray detector system for the NEAR mission and application to future missions", proceedings of the IAA Second International Conference on Low-Cost Planetary Missions (IAA L-0905P), April, 1996.
7. M. J. Bielefeld, R. C. Reedy, A. E. Metzger, J. I. Trombka, and J. R. Arnold, "Surface chemistry of selected lunar regions", Proc. Lunar Sci. Conf. 7th, pp 2661-2676, 1976.

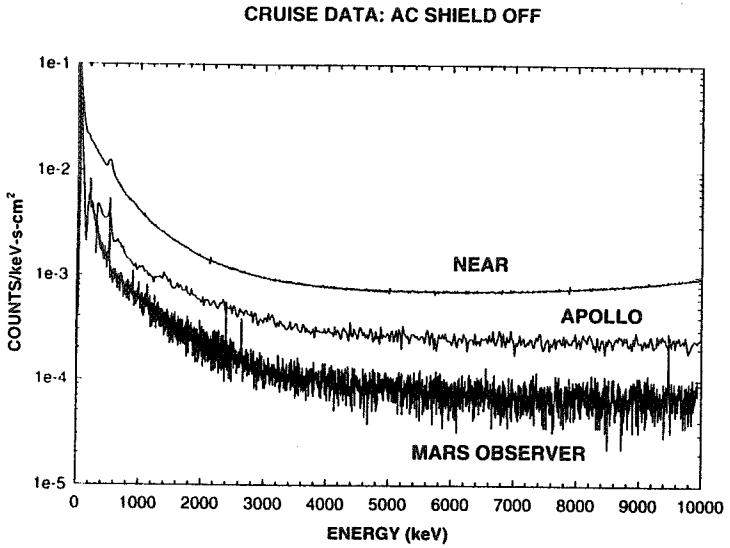

Figure 1. Comparison of three background spectra with AC shield off.

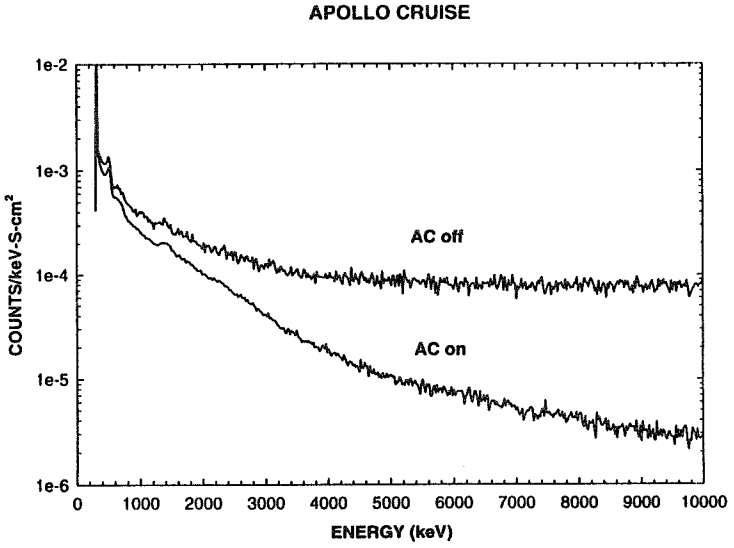

Figure 2. Comparison of Apollo background spectra with AC shield on and off.

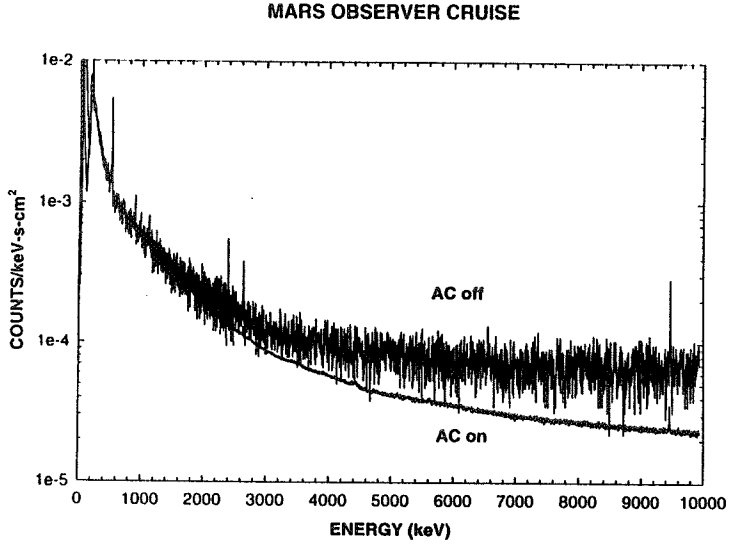

Figure 3. Comparison of Mars Observer background spectra with AC shield on and off.

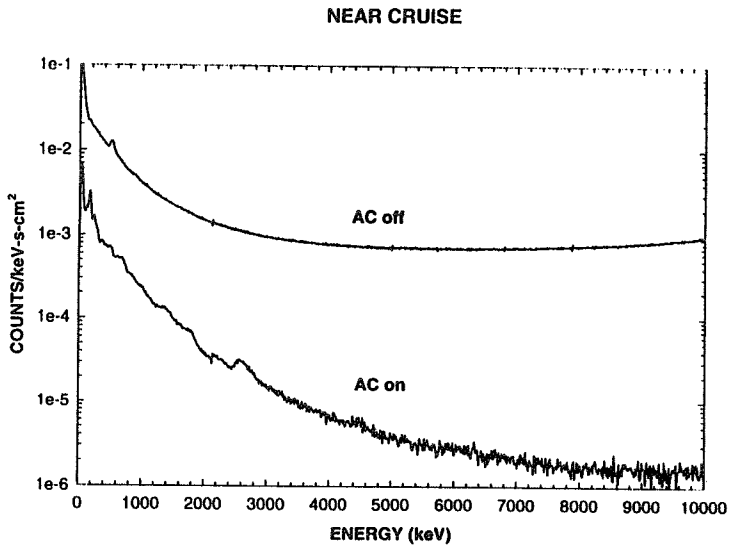

Figure 4. Comparison of NEAR background spectra with AC shield on and off.

Cosmic Ray Induced Degradation In X-Ray Detectors On Board The Near Earth Asteroid Rendezvous Spacecraft

S. R. Floyd, J. I. Trombka, NASA's Goddard Space Flight Center, Greenbelt, Maryland 20771
J. O. Goldsten, E. M. Fiore, Johns Hopkins University Applied Physics Laboratory, Laurel, Maryland 20723-6099

The Near-Earth Asteroid Rendezvous (NEAR) mission is the first in NASA's new Discovery Program to explore the solar system. Launched in February 1996, the NEAR spacecraft will take a long cruise flight arriving at the asteroid 433 Eros in January 1999 for a one year orbiting survey operation. This long exposure to the space environment has already proven to be an additional complication for the x-ray spectrometer.

The asteroid pointing detectors for the x-ray spectrometer are three gas-filled proportional counters with resolving power in the range of 1 keV. Therefore, to resolve the important but closely spaced magnesium, aluminum and silicon k alpha lines(1.255, 1.487, 1.739 keV respectively), magnesium and aluminum balanced filters are used on two of the detectors. The x-ray florescence from the surface of Eros is stimulated by solar x-rays. A proportional counter and a silicon PIN detector are used to monitor the solar incident x-ray flux.
The proportional counters are single wire gas filled beryllium lined steel tubes operating at about 1100 volt. The 25 cm^2 optical window is one mil. thick beryllium. To define the detector's active region, two boron nitride disks were incorporated in the tube just outside window area. It appears from the space flight data that the space environment is creating a charge on these boron nitride disks which ultimately distorts the tube gain and resolution. This broadening of the photo peak makes it more difficult to identify weak peaks and so degrades the statistical accuracy for some very important elements such as sulfur, calcium and iron (2.307, 3.690, 6.403 keV respectively). If the broadening is severe enough in the low energy region, counts will be lost as the photo peak spreads below the lower level discriminator (0.7 keV).

Laboratory tests using flight spare proportional counter detectors and laboratory detectors without the disks have verified the anomaly. The window area of a degraded detector was mapped for gain using a collimated Fe-55 source. The data clearly shows a decreasing gain from the center of the window toward the edges parallel with the central wire electrode. These laboratory tests show that the gain near the central part of the window is essentially that of a fresh detector. With a non collimated source onto a full window area, this is seen as a low energy tailing of the gaussian peak because a portion of the detector is processing photons with a lower gain. In the laboratory the degradation was induced using higher energy sources such as Cd-109 and Co-60. The flight data indicates that although gamma radiation is contributing to the charging, the charged particle flux seems to be the major contributor.

The asteroid pointing detectors were designed with an Fe-55 sources which can be rotated into the window position for energy calibration. These sources are used to evaluate the anomaly. Laboratory data shows a resolution degradation plateau in the twelve to fourteen hour range. Some of the flight data supports a plateau in this time frame, but other data indicate a longer time. Fortunately, the detectors recover fully in a few minutes (30 to 40 minutes in the lab) with the high voltage off. Every opportunity is being taken to evaluate cruise flight data and compare to laboratory data. All of these findings will be considered in the development of the science data taking operational mode for the x-ray spectrometer system at Eros.

Page intentionally left blank

A Monte-Carlo Ray-Tracing Program for Modeling Scintillators

Amanda Gerrish
Constellation Technology Corporation
P.O. Box 3687
Seminole, FL, 33775-3687

Abstract: A new Monte-Carlo ray-tracing program useful for the design of active scintillator shielding to reduce radiation background effects in space is described along with results for a BGO anti-Compton shield and a CsI(Na) active collimator.

Introduction. High energy gamma-ray radiation often deposits only a random part of its energy in detector materials due to a Compton scattering event, contributing unwanted background noise to the spectrum. One of the key techniques for reducing Compton-scattered radiation background effects is to surround the detector with scintillating detector material so that a scattered gamma-ray from a Compton event might be simultaneously detected in the scintillating materials and electronically identified for rejection. Another technique for reducing background radiation effects is to provide a collimator to limit the detector's field-of-view, thus rejecting unwanted background signal from sources other than the intended source. The use of an active collimator consisting of a scintillator detector material ensures that gamma-rays which scatter from the collimator are rejected and do not contribute to the Compton background. In space applications, these techniques carry with them a high price in overall detector system weight. It becomes important, therefore, to optimize the geometry of the scintillator shield and collimator design so that the greatest overall advantage is gained for the least volume of material.

In our recent development of a man-portable germanium spectrometer, which incorporates a BGO anti-Compton shield and a CsI(Na) active collimator, both coupled to miniature photo-multiplier tubes (PNTs), added weight from an active shield and collimator was also a principal concern. To optimize the light collection properties of these devices, we have developed a new Monte-Carlo ray tracing program, SCINTSIM, written in the Mathematica interpretive programming language. Mathematica was used because of the simplicity of coding the complicated geometry and mathematical calculations, and because calculational speed was not particularly critical. SCINTSIM simulates the transport of photons generated by random gamma-ray interactions within a scintillator volume coupled to one or more PMTs. Using this code it is possible to predict the variation in light collection efficiency for various scintillator size and shapes, surface reflectivities, and PMT placements. Plots are shown of the variation in light collection efficiency for particular anti-Compton shield, and active collimator, configurations. Based on these simulations, the shield and collimator were designed and built, and they are now being used with the man-portable Ge spectrometer. Response uniformity data from the (actual) shield and collimator are also presented.

Description of SCINTSIM. SCINTSIM is intended to model photon transport in a cylindrical solid have diffuse reflecting surfaces. In addition, light absorbing regions on the surfaces were added to simulate PMTs, and the light absorption at these regions is calculated to determine the light collection efficiency. The coordinates for the scintillator surfaces are specified in cylindrical coordinates which allows much greater simplicity for modeling cylindrical shapes. Even so, it was possible to models an active CsI(Na) collimator which did not have perfect cylindrical symmetry. Diffuse reflecting surfaces

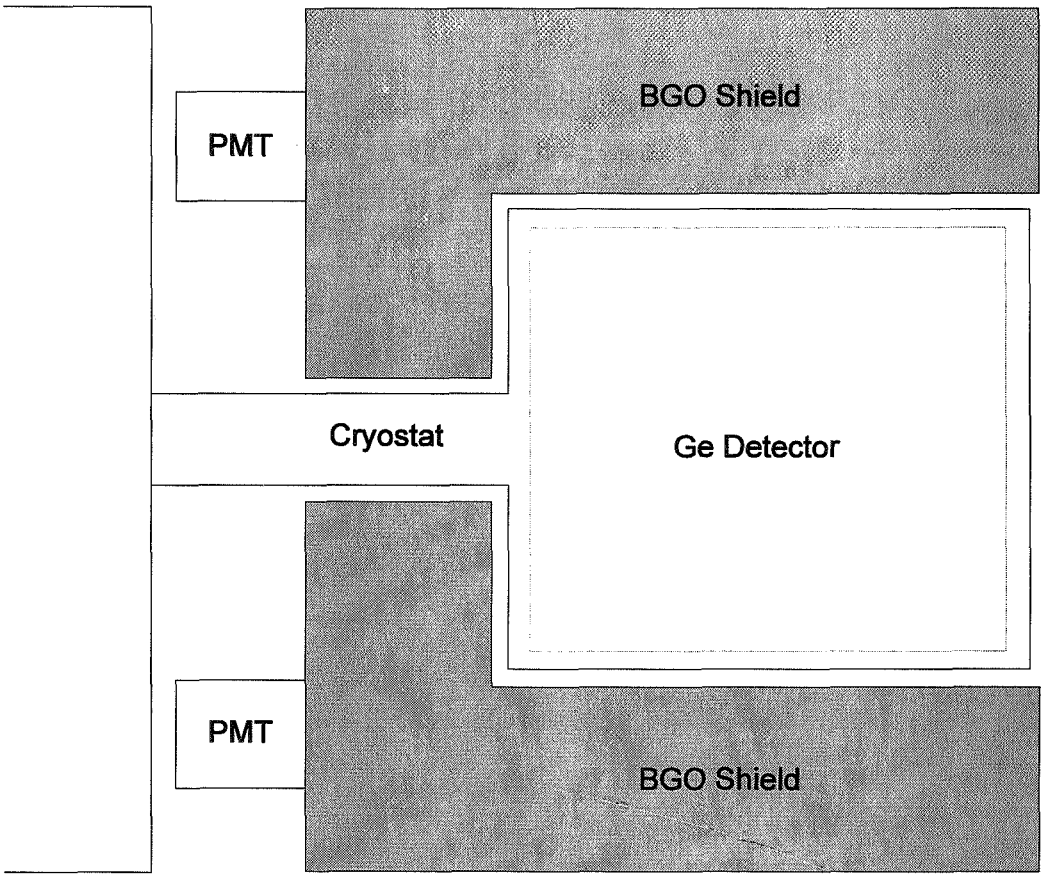

Figure 1. Cross-sectional view of Ge detector, cryostat, and BGO anti-Compton shield.

shield were assumed since scintillation detectors are normally coated with a white diffuse reflector (such as MgO powder). Reflective losses in the range 0.01 to 0.04 were used in this study. SCINTSIM generates rays at points within the volume as specified by the user. In this study, the spatial variation in charge collection efficiency was determined by generating many randomly oriented rays along a uniform grid in a cross-sectional slice of the scintillator volume. SCINTSIM determines the total distance each ray travels before striking an absorbing surface, and the number of reflections it undergoes. From this, attenuation and reflective losses are calculated. SCINTSIM calculates, stores, and plots the light collection vs. gamma-ray interaction position data, and can also produce plots of individual ray paths through the solid.

Collimator modeling with SCINTSIM. Figure 1 shows a drawing of the Ge detector, cryostat, and BGO anti-Compton shield. (All of the components are cylindrical and the drawing shows a cross-sectional slice.) Figure 2 shows the light collection efficiency of the upper half of the BGO shield shown in Figure 1 for uniform gamma-ray irradiation. Four percent reflective losses were assumed along with negligible transmission losses.

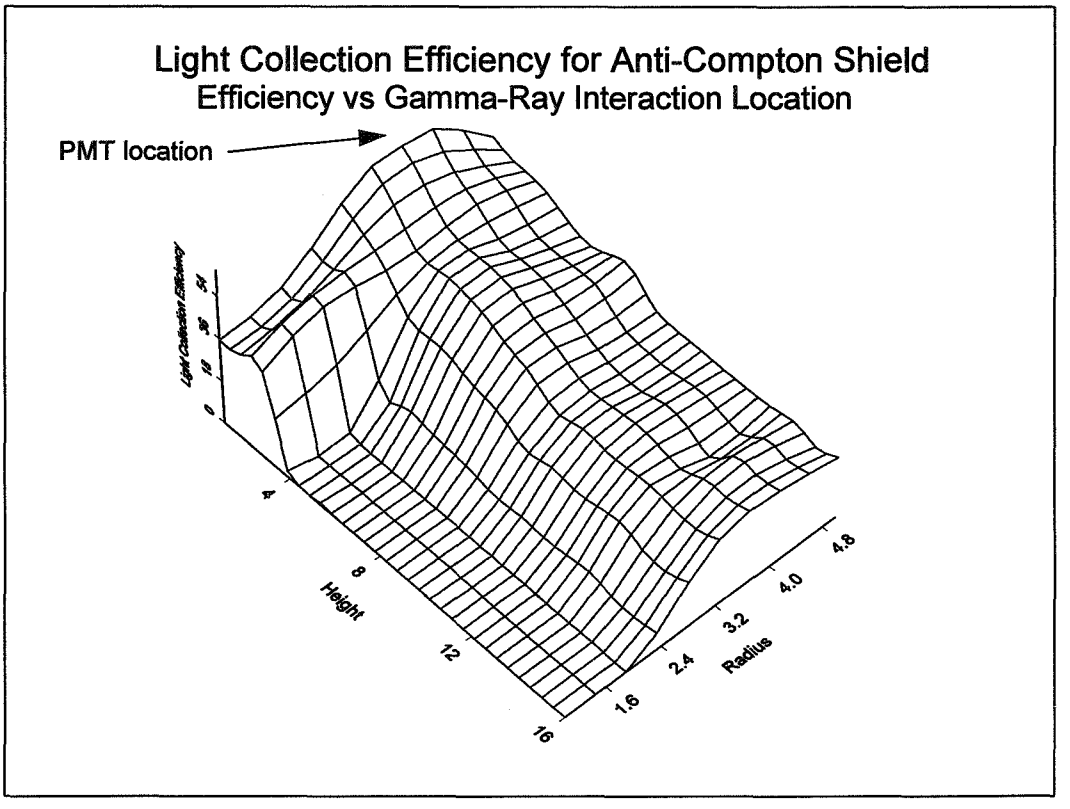

Figure 2. Light collection efficiency vs. gamma-ray interaction location for BGO anti-Compton shield.

The PMTs were located as shown in the figures and, as expected, the region of the shield near the PMTs exhibits the highest response. The light collection efficiency varies from 65% near the region where PMTs were located to about 22% near the end of the shield furthest from the PMTs. The standard deviation in the light collection efficiency is 31%. These numbers were found to be very sensitive to the actual losses in the scintillator (which are difficult to determine experimentally.) As a comparison, a BGO anti-Compton shield of similar dimensions and PMT placement was recently fabricated for use with a Ge detector. It was tested for uniformity by illuminating different areas of the shield (at 40 separate locations) using a collimated gamma-ray source. The standard deviation in the measured light collection efficiencies was 40%.

Using SCINTSIM, it was found that using a tapered shield had little effect on the light collection efficiency provided that the total reflective surface area of the shield did not

change. This allowed us to design a shield which had better anti-Compton characteristics (for the same weight of material) without compromising the light collection properties.

Conclusions. SCINTSIM was found to be a useful tool for modeling the light collection of various scintillator configurations, and aided our design of and anti-Compton shield and active collimator. Additional data will be presented for a 7-hole CsI(Na) collimator. This collimator was designed and modeled with SCINTSIM, and was recently fabricated and tested.

Perspectives on Mercuric Iodide as a Radiation Detector Material for Space Measurements

Amanda Gerrish and Lodewijk van den Berg

Summary

Mercuric iodide is one of the room-temperature semiconductor detector materials which have become available recently, and is particularly well suited for space applications. The main advantages of this material are the high electronic bandgap (2.1 eV), high density (6.3 gm/cm^3) and high atomic number of its constituent elements. A disadvantage is the relatively poor transport properties of the electronic charge carriers, which is common to all known room-temperature detector materials.

Single crystals of mercuric iodide are grown from the vapor by physical vapor transport. Since this process takes place in evacuated, closed ampoules, the size of the crystals is determined by the amount of material originally loaded in the ampoule. The total growth process, including nucleation of a single crystal seed, takes approximately six to eight weeks. Single crystals up to 1000 g. in weight and with approximate dimensions of 6 x 5 x 5 cm^3 have been grown by this process.

Detectors of various dimensions can be fabricated from these crystals by cutting, polishing, and electrode application. Slices of a desired thickness can be cut from a crystal using a cotton thread saturated with a potassium iodide solution. Square or rectangular pieces can be cut out of each slice. After polishing and etching the pieces on both sides to remove cutting irregularities, selected areas are masked off for electrode application. The most commonly used electrode material is palladium, which is thermally evaporated onto the masked piece in a vacuum system. Thin palladium contact wires are attached to the electrodes, the finished detector is mounted on a ceramic support for mechanical stability, and the complete assembly is encapsulated in parylene for environmental protection.

The standard gamma ray detector fabricated by Constellation Technology Corporation is 2.5 x 2.5 x .3 cm^3. The dynamic range of these detectors is approximately 30 keV to 5 MeV. The applied bias to these detectors is normally 2000 volts. The resulting high field is necessary to collect the electrons and holes which are generated almost homogeneously throughout the volume of the detector, especially at high radiation energies. The lower end of the energy range is determined by the leakage current through the detector, which at this high bias is of the order of 100 pA. The higher end is somewhat artificial and is chosen by us to reflect the decreased efficiency of the detector at these higher energies. A good quality detector of this size often has an energy resolution of < 5% FWHM over the whole range.

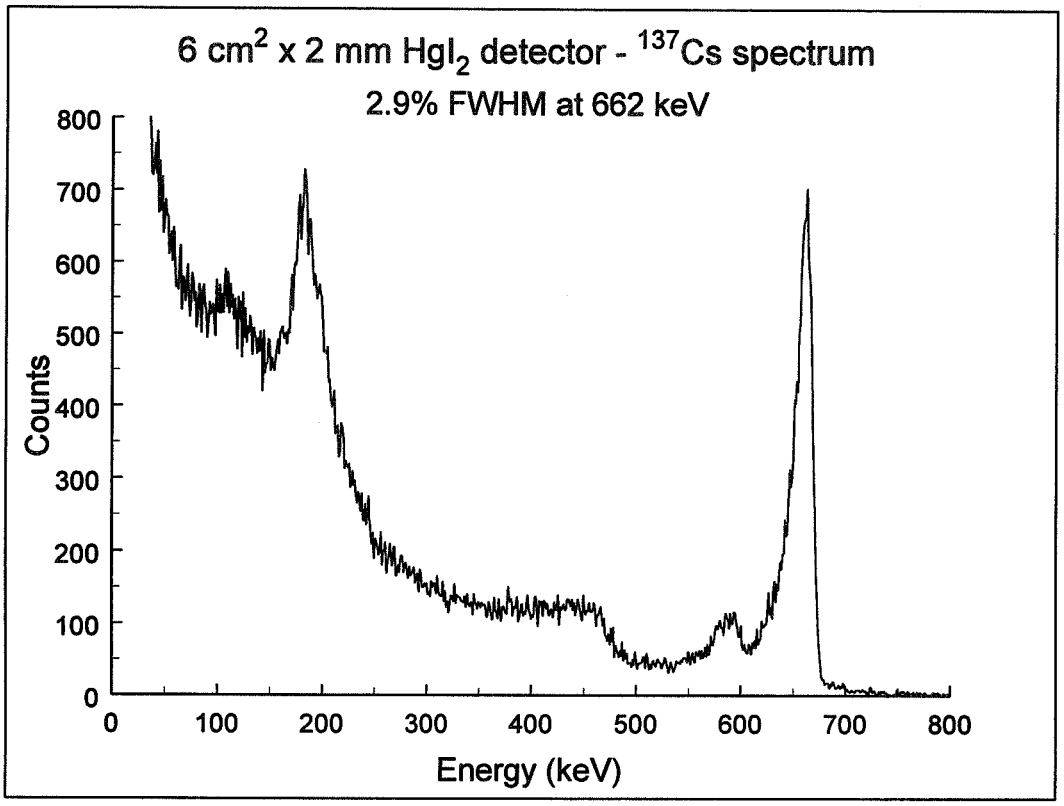

Figure 1. Plot of ^{137}Cs spectrum from a 6 cm^2 x 2 mm HgI_2 detector.

X-ray detectors vary in size, but for our own internal evaluations we prefer to work with 1 x 1 x .1 cm^3 detectors. At x-ray energies the radiation is absorbed close to the entrance surface of the detector and the slow positive charge carriers do not have to travel through the whole detector to reach the proper electrode, the bias can be reduced to approximately 500 Volts. This reduces the leakage current to about 1 - 5 pA. As a result the lower energy range of the detector is around 700 eV. The energy resolution of these detectors can be less than 500 eV in the range of 1 to 10 keV. For higher energies the resolution is approximately 5%. If one wants to increase the area of these detectors, then noise associated with the detector capacitance degrades the performance. To compensate, the thickness of the detector will have to be increased which can lead to incomplete collection of the electrons and loss of spectral resolution.

Experiments in accelerators with charged particles and high intensity neutron beams have shown that the damage threshold of mercuric iodide detectors is higher than for other semiconductor detector materials such as Ge. This makes mercuric iodide an ideal candidate for active anti-coincidence shields to reduce the Compton scattering signal from a detector. The active detector can be surrounded by slabs of mercuric iodide in a compact, rugged, and lightweight configuration.

Room temperature semiconductor detectors such as HgI_2 are used for x-ray fluorescence measurements[1], medical imaging[2,3], industrial and environmental monitoring of radiation[3,4,5,6], geological exploration[3], astrophysical measurements[7,8,9], and high energy physics research[4,10]. X-ray fluorescence spectrometers using HgI_2 are produced commercially and are used for elemental analysis and lead paint detection[11]. Also, HgI_2 arrays have been fabricated up to 32 x 32 pixels and were used in a portable gamma-ray imaging camera[4].

As an illustration, Figure 1 shows a ^{137}Cs spectrum acquired with a large volume mercuric iodide gamma-ray detector. The energy resolution at 662 keV is 2.9% FWHM with a peak-to-valley ratio of 15:1. The peak efficiency of this detector is about 11% at this energy. If required, HgI_2 detectors of this size can easily be stacked so as to provide higher efficiency without sacrificing energy resolution. In addition, much larger HgI_2 detectors can be fabricated for use as counters in anti-coincidence shields. HgI_2 detectors have been fabricated as large as 5 x 5 x 1 cm^3 and work well as counters but exhibit poor energy resolution due to incomplete hole collection. For background radiation measurements in space, a Ge spectrometer or scintillation spectrometer could be surrounded by large volume HgI_2 detectors for anti-coincidence shielding. Due to the low power requirements and high efficiency of HgI_2 detectors, they are well suited for space measurements.

---

[1] Warburton, W.K., Iwanczyk, J.S., Dabrowski, A.J., Hedman, B., Penner-Hahn, J.E., Roe, A.L., Hodgson, K.O., and Beyerle, A. (1986), *Nucl. Instr. and Meth.* **A246**, 558.

[2] Barber, H.B., Barrett, H.H., Hickernell, T.S., Kwo, D.P., Woolfenden, J.M., Entine, G., and Baccash, C. (1991). *Med. Phys.* **18**(2), 373.

[3] Entine, G., Waer, P., Tiernan, T., and Squillante, M.R. (1989), *Nucl. Instr. and Meth.* **A283**, 282.

[4] Patt, B.E., Beyerle, A.G., Dolin, R.C., Ortale, C. (1989), *Nucl. Instr. and Meth.* **A283**, 215.

[5] Droms, C.R., Langdon, W.R., Robison, A.G., and Entine, G. (1976) *IEEE Trans. Nucl. Sci.* **NS-23**(1), 498.

[6] Friant, A., Mellet, J., Barrandon, G., and Csakvary, E. (1989), *Nucl. Instr. and Meth.* **A282**, 227.

[7] Ricker, G.R., Vallerga, J.V., and Wood, D.R. (1983), *Nucl. Instr. and Meth.* **213**, 133.

[8] Bradley, J.G., Conley, J.M., Albee, A.L., Iwanczyck, J.S., Dabrowski, A.J., and Warburton, W.K. (1989) *Nucl. Instr. and Meth.* **A283**, 348.

[9] Economou, T., and Iwnaczyk, J. (1989), *Nucl. Inst. and Meth.* **A283**, 352.

[10] Becchetti, F.D., Raymond, R.S., Ristinen, R.A., Schnepple, W.F., and Ortale, C. (1983), *Nucl. Instr. and Meth.* **213**, 127.

[11] TNT Technologies, Round Rock, TX, 1994 product brochure.

Page intentionally left blank

Simulation of HEAO 3 Background

B. L. Graham (George Mason University)
B. F. Phlips (NRL/USRA)
J. D. Kurfess and R. A. Kroeger (NRL)
Code 7650
Naval Research Laboratory
4555 Overlook Ave. SW
Washington DC 20375

Abstract

Gamma-ray background in the High Resolution Gamma-Ray Spectrometer on HEAO 3 has been Monte Carlo modeled. Decay of nuclei produced by spallation of cosmic rays, trapped protons and their secondaries was included in this model.

1 Summary

A Monte Carlo technique for modeling background in space-based γ-ray telescopes has been developed. The major background components included in this modeling technique are the diffuse cosmic γ-ray flux, the Earth's atmospheric flux, and decay of nuclei produced by spallation of cosmic rays, trapped protons and their secondaries, the decay of nuclei produced by neutron capture and the de-excitation of excited states produced by inelastic scattering of neutrons. The method for calculating the nuclear activation and decay component of the background combines the low Earth orbit proton and neutron spectra, the spallation cross sections from Alice91 [1], nuclear decay data from National Nuclear Data Center's (NNDC) Evaluated Nuclear Structure Data File (ENDSF) [2], database, and three-dimensional γ-ray and β transport with Electron Gamma-ray Shower version 4 (EGS4) [3] using MORSE-CG. The background in HEAO 3 was modeled for the active and passive components of the HEAO 3 instrument. Actual background from the HEAO 3 space instrument are used to validate the code. This Monte Carlo code handles the following decay types: electron capture, β^-, β^+, meta-stable parents and short lived meta-stable daughters, and isotopes that have branchings to both β^- and β^+. The code follows a cascade of photons to the ground state of the daughter, and propagates these photons and appropriate accompanying β simultaneously. The Monte Carlo code does not propagate α particles or model α decays. This simulation for HEAO 3 does not include elastic neutron scattering.

2 Data Input

The configured information base used for this model contains the HEAO 3 geometry, the orbital average cosmic ray flux and trapped protons, the cross sections for neutron and proton activation, and the β spectrum and branching ratios for both the βs and the cascade of γ-rays to the ground state of the daughter nuclei for the decay of activated isotopes.

A mass model, which describes geometry and composition, was made for the components of HEAO 3. HEAO 3 consisted of four Ge co-axial detectors in a CsI anti-coincidence shield. Each of the Ge detectors was 5.4 cm in diameter and 4.5 cm thick, with a $\sim$300 μm thick dead layer on the surface. The detectors were held in a thin aluminum cup that was $\sim$0.4 mm thick. These were all contained in an aluminum cryostat which had 0.5 mm thick windows over the detectors and was 4 mm thick elsewhere. There was $\sim$1 cm thick aluminum cold plate between the detectors and

the cold finger. The cold finger was a 6.4 mm diameter silver rod. There also was a 0.5 cm thick stainless steel baseplate. This baseplate was made of type 304 stainless steel which is nominally composed of 10% Nickel, 20% Chromium and 70% Iron. The cryostat was surrounded on all sides by a 6.6 cm thick CsI shield, with holes in the upper lid of the shield which collimated the field of view to 30° [4]. The decays of isotopes produced from components of the instrument that were made of Ge, Al, CsI, Fe (with Cr, Ni) and Ag were modeled. Components of the spacecraft outside the shield were not included in the mass model for this work.

The activation of the detectors and surrounding materials was due to a flux mostly composed of secondary neutrons and protons produced by cosmic rays and trapped protons incident on the spacecraft. In this work, the neutron and proton flux used was an approximation based on an orbit of 500 km at an inclination of 44° [4]. The proton and neutron flux used was scaled from the flux for a 300 km, 28.5° orbit according to the scaling method used by Gehrels [5] which was based on data from the ballon instrument, Low Energy Gamma-ray Spectrometer (LEGS) [6].

The cross-sections for spallation, from neutrons and protons incident on the detectors, shields and support structures were taken from Alice91. The reported error on the Alice91 spallation cross-sections was less than 30% [1]. The NNDC's Evaluated Nuclear Data File (ENDF) database contains measured cross-sections for neutron capture and resonance.

The model used the γ-ray spectra from the Earth's atmosphere as measured by the Solar Maximum Mission (SMM) [7]. This spectrum was folded through both the open collimator response and the response to shield leakage. A ^{40}K calibration source was modeled inside the cryostat and was fitted to the measured data only at the 1.46 MeV line. The cosmic diffuse γ-ray background is from the Peterson model [8]. This flux is also folded through the open collimator response and the response to shield leakage.

The ENDSF database was used for β branchings and half-lives for β-unstable parent isotopes, and for energy levels and gamma-ray branching ratios for daughter isotopes, as well as the half-lives of intermediate states of daughter isotopes. Also included in NNDC databases are the x-ray fluorescence yields and energies of the characteristic x-ray(s) for each isotope [2].

3 Method and Tools

EGS4 is a Monte Carlo transport code that was used for β and gamma transport. Included in EGS4 are routines for the following photon interactions: photo-electric absorption; Compton scattering and pair production, as well as routines for the scattering of electrons; ionization energy losses; Möller; Mott and Bhabha scattering. The combinatorial geometry package MORSE-CG was used, allowing for full three-dimensional propagation of βs and γs.

A user-defined routine was designed and implemented for initializing EGS4 to model a nuclear decay, one decay at a time. The βs and the γ-rays produced for a given isotope in a single decay follow a single series of branchings in a cascade to the ground state of the daughter for each decay modeled via Monte Carlo. This cascade is produced starting from the β-unstable parent isotope and ends at the ground state of the daughter. At the β-unstable parent a β branch or Electron Capture (EC) energy or Internal Transition (IT) is chosen from the branchings available (or appropriate) for that parent isotope via Monte Carlo selection from the branching ratios. If a β branch was selected then the β endpoint energy for that branch was used with the probability distribution formula for the β spectrum to determine the energy of the β. Then the β endpoint energy, or the EC energy, was subtracted from the ΔQ value for the decay of that parent isotope to determine the energy level of the daughter isotope for start of the γ-ray cascade. At each energy level of the daughter isotope a γ-ray was randomly selected from the possible γ-rays for that energy level according to

their branching ratios. The next energy level was determined by subtracting the energy of the γ-ray selected from the value of the previous energy level until the ground state of the daughter isotope is reached.

For each parent unstable isotope a number of decays were modeled. For every decay the energy deposited by each interaction in the detectors or the shield was summed for each detector and the shield. The energy resolution was applied to the summed energy for each active element. Then a histogram was made of all decays of a parent isotope where the energy deposited in the detector is above the detector threshold, and the energy deposited in the shield was below the shield's threshold. The histograms were summed together with appropriate normalization for the decay rate of each isotope and summed with the cosmic diffuse γ-ray flux and the Earth's atmospheric gamma-ray flux, and was compared to the measured background rate.

The production rate for each β-unstable isotope j is

$$R_{prod_j} = \sum_i \int F_n(E)\sigma_{n_{j,i}}(E)a_i\rho_i\frac{N_o}{A_i}V\,dE + \sum_i \int F_p(E)\sigma_{p_{j,i}}(E)a_i\rho_i\frac{N_o}{A_i}V\,dE \qquad (1)$$

Where i is a stable isotope in volume V, a_i is its fractional abundance, ρ_i the density, N_o is Avogadro's number, A_i is the atomic weight, $\sigma_{n_{j,i}}$ and $\sigma_{p_{j,i}}$ are the cross-sections for neutron and proton spallation, respectfully, to β-unstable isotope j from isotope i, and F_p and F_n is the cosmic-ray proton and neutron flux [5]. The fractional abundance a_i was calculated for the isotopic fraction for each element in each material.

A daily SAA exposure of 220 minutes per day was used. An assumption of 10 SAA passages per day was used resulting in an average of 22.0 minutes for each SAA passage. The detectors on HEAO 3 were turned on starting from 600 s after an SAA passage until the beginning of the next SAA passage. The average production rate for the time variable component relative to the constant component is $D_R = R_{saa} - R_{non-saa}$.

For each isotope the total decay rate is

$$R_{decay} = R_{prod_{non-saa}}(1 - e^{-\lambda t}) + \frac{\sum_{i=0}^{t_i \le t}\sum_{k=i}^{t_{start_{k+1}}=t} D_R t_{saa}(e^{-\lambda(t_{on_k}-t_{in_i})} - e^{-\lambda(t_{start_{k+1}}-t_{in_i})})}{\sum_{i=0}^{t_{start_{i+1}}=t}(t_{start_{i+1}} - t_{in_i})} \qquad (2)$$

Where t_{start_i} is the start of an SAA passage, t_{in_i} is the end of an SAA passage, t_{on_i} when the detectors are turned on after an SAA passage is over and i is over all SAA passages and k is over all periods between SAA passages following the i^{th} SAA passage for up to 12 half lives. This total decay rate is calculated for each β-unstable isotope using its half-life and production rates (both SAA and non-SAA).

4 Results

Figure 1 shows the background spectrum modeled for HEAO 3 summed over all components modeled (solid line) and compared to the measured data (dashed line) taken from the first 50 days of operation [4, 9]. Included in the model were all unstable isotopes of with production >0.1% of the most abundantly produced from Ge (44 isotopes), all unstable isotopes of with production >1.0% of the most abundantly produced from Al (9 isotopes), steel (30 isotopes) and CsI (36 isotopes), and all unstable isotopes of with production >10.0% of the most abundantly produced from Ag (9 isotopes).

The model captures most of the major line features and shape of the continuum background. Agreement is good throughout the background spectrum suggesting that the essential physics is

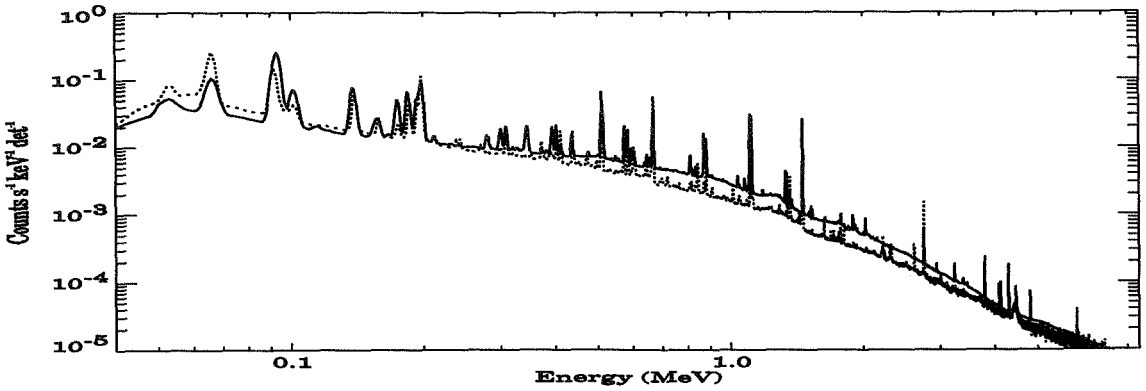

Figure 1: Resultant Model Spectrum vs. Measured Data from the HEAO 3 Background

being modeled correctly. The errors in the model is due to errors in the cross sections and errors in the secondary neutron and proton spectra. The error in the continuum at 1.0 MeV is due to over production of a few isotopes, ^{70}Ga, ^{68}Ga and ^{75}Ge, that have signifcant β spectra. Another difference is in the doublet ^{69}Ge lines at 573, 872, 1107 and 1337 keV which are due to a 53.9% x-ray fluorescence yield, but measured data from HEAO 3 shows clearly that the fluorescence yield is dependent on the line energy. There are 133 lines observed in the data from HEAO 3. Fifty-seven of these lines are not observed in the model, of which 14 are from U, Pb, Tl and Th contaminates (not modeled). Seventy-seven lines were observed in the model that agreed with lines in the data, of which 5 were mis-identified by Wheaton et.al [9]. There were also 5 significant lines in the model that were not in the data. Of the observed 77 lines, 6 were significantly over represented (by more than a factor of 2), and 4 were significantly under represented (by more than a factor of 2).

References

[1] "Global test of Modified pre-compound decay models" Blann and Vonach *Phys Rev* **28** (1983) p 1475.

[2] NNDC, National Nuclear Data Center, Brookhaven National Laboratory, Brookhaven, NY.

[3] "The EGS4 code system" W.R. Nelson et.al. *SLAC-265* (Stanford University), 1985.

[4] "The HEAO 3 Gamma-ray Spectrometer" W. Mahoney et.al. *NIM* **179** (1980) p 363.

[5] "Instrumental Background in gamma-ray spectrometers flown in low Earth orbit" N. Gehrels, *NIM A* **313** (1992) p513.

[6] "Instrumental Background in Balloon-borne gamma-ray spectrometers" N. Gehrels, *NIM A* **239** (1985) p324.

[7] "Satellite Observation of Atmospheric Nuclear Gamma Radiation" J. Letaw, et.al. *J. Geophys. Res.* **94** (1989) p 1211.

[8] "Measurement of Diffuse Cosmic Gamma-Rays by HEAO-1" L. E. Peterson, et.al. *Presented at INTEGRAL workshop* (St. Malo, 1996).

[9] "The HEAO 3 Background: Spectrum Observed by a Large Germanium Spectrometer in Low Earth Orbit" W. Wheaton et.al. *"High Energy Radiation Background in Space"* American Institute of Physics (1989) p 304.

Spectral Analysis in High Radiation Space Backgrounds with Robust Fitting

G. P. Lasche, R. L. Coldwell, J. A. Nobel, A. C. Rester
Constellation Technology Corporation
P. O. Box 3687
Seminole FL, 33775-3687
J. I. Trombka
Goddard Space Flight Center, Code 691
Greenbelt, MD 20771

Abstract. Spectral analysis software is tested for its ability to fit spectra from space. The approach, which emphasizes the background shape function, is uniquely suited to the identification of weak-strength nuclides in high-radiation background environments

Introduction. Spectral analysis software under development at Constellation Technology Corporation is tested for its ability to fit spectra from high radiation background environments in space. The approach, which emphasizes the identification of the background shape function, is uniquely suited to the identification of weak-strength nuclides in high radiation background environments. Compared to earlier work in robust fitting,[i,ii] this approach significantly reduces the required computational time, enhances sensitivity and accuracy at the high energy portion of the spectrum where statistics are low, and incorporates relative line strength data and x-ray data to significantly increase the ability to identify specified radionuclides. A "standard" background function containing up to 120 adjustable parameters is determined by fitting a high count spectrum. This function is then parameterized in terms of only a few (1-8) adjustable constants. A modified chi-square which is minimized with respect to these parameters thus allows low count spectra to be fitted to the high count background. The foreground is made up of a group of peak shapes, an efficiency curve, and a table of gamma ray lines. This response function is linear in each nuclide, but also contains non-linear parameters giving the energy calibration, the peak widths, and corrections to the efficiency in the form of "absorption" coefficients. The total counts for each nuclide divided by its standard deviation, which is also determined by the software, gives the statistical certainty of detection of the nuclide.

The first assumption in this fitting technique is that with the aid of robustness, for a systematic method for decreasing the weights on data far from the developing fit, the only assumption needed to fit the background is the continuity of the background function and its first and second derivatives throughout the region being fitted. The second assumption is that a few peak shape templates with variable locations, widths and heights can represent the response of the detector to radiation coming from the sample. Frequently a single Gaussian will suffice for these shapes, but the code currently fits the best of up to ten shapes, which it can define based on actual data provided by the user. A third assumption is that the relative strengths of the gamma rays from each element are those found in the *Table of Radioactive Isotopes*[iii].

The background. The background is fitted to either a cubic spline

$$b(x) = \sum_{i=0}^{3} c_i x^i + \sum_{j=1}^{M} d_j \left(k_j - x\right)_+^3$$

$$(x)_+^3 = x^3 \quad x > 0$$
$$= 0 \quad x \le 0$$

Eqn 1

or to the exponential of a cubic spline. The advice of de Boor[iv] is ignored and the knot locations are made parameters so that the robustly-modified chi-square is minimized with respect to the *c*'s, the *d*'s and the *k*'s in Equation 1. Minimizing with respect to the knots is not a fast procedure, but it has the potential for giving a much better curve fit owing to the fact that it optimizes the locations of the third derivative discontinuities in the background representation. It is not recommended that one try to completely fit the background before any peaks are introduced, though it works remarkably well. The recommended procedure which is implemented in the code is to get a reasonable fit to the background with a few constants, then to allow the large peaks to be introduced, then to refit the background with a few more constants, and then to allow smaller peaks and so on.

The peak shape. The code is designed to allow the user to select a large peak that has been fitted with one shape, to remove all but a single component, and to fit the residual as a new peak shape. In practice this can require a few iterations to converge on the optimal peak shape.

The response function. The nuclides of interest are put in a file consisting of their names. Each name refers in turn to a file consisting of either the elemental K lines and their intensities ordered by energy, or the nuclide's gamma-ray lines and their intensities ordered by energy. These files, along with a template for the detector's response to an individual line enable a complete response function to be formed. This response function contains constants representing the energy calibration, the full width at half maximum, and the efficiency/absorption calibration. This last can be turned on and off for individual nuclides. An initial crude calibration based on peaks known to be present is needed to start the fit. An estimate of the full width at half maximum accurate to within an order of magnitude is also necessary to start the fit. The fit also needs three energies associated with large peaks so that the minimization can improve the initial calibration sufficiently to start the fit.

Absorption and efficiency. The absorption (*ie*, the attenuation of line strength due to absorption of radiation by intervening matter) is fitted as the exponential of a linear term plus a two knot spline with variable knots. The efficiency has the same form with the opposite sign. The difference is that the efficiency is not varied in the process of fitting. The log of the efficiency is given by 9 constants in the form

$$leff(E) = cE + \sum_{j=1}^{4} d_j \left(k_j - E\right)_+^3 \qquad \textbf{Eqn 2}$$

where the limitation to a linear form at large energy values incorporates the theoretical form and gives the most accurate extrapolation.

Determination of the standard background. After typically starting with a fit to the background by making the efficiency a fixed function, the background and the response functions are iteratively fitted with an increasing number of constants until all potential peaks with strengths greater than a desired sensitivity in terms of the standard deviation in the underlying background are added. The resulting background along with the energy coefficients is then placed in a standard background file. The constants in this file become a function which is fitted to the data in terms of an overall constant, energy parameters and absorption coefficients.

Example fit. An example fit using this technique on a low-resolution is given below:

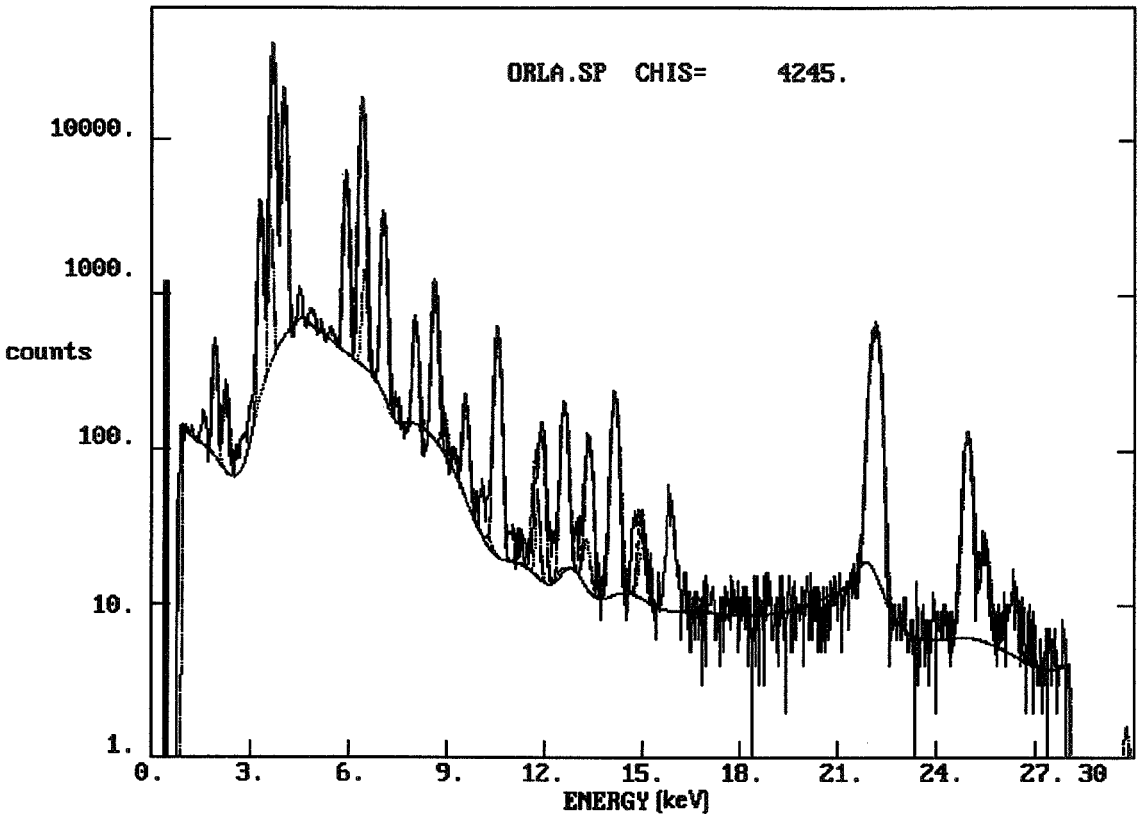

Figure 1 Example robust fit of low-resolution background and line data provided by W. Maenhaut.

Conclusion and timings. The background fits are the most time consuming. The quadratic radius of convergence of the chi-square becomes very small when the knots are included and this means a lot of steps. The time required goes approximately as the 4th power of the total number of knots. Typically 4 hours or more on a IBM 486 DX2 is required for the 56 and 60 background fits. The absorption/efficiency fits also involve moving knots, these typically require 1/2 to 1 hour. The fit to the response function, the addition of well separated peaks and the modifying of the background is relatively fast. The final fits typically require 5 to 10 minutes.

Once a method of taking data has been determined, a data set with a large number of counts can be taken. Extensive work can then be done to determine a standard background and an efficiency curve. These combined with the files containing the K_α, K_β, and gamma-ray lines and intensities can then be used to quickly fit any spectra that are taken. Since the information used is maximized and the number of parameters are minimized with this approach, the ability to identify lines from noise is optimized.

---

[i] R.L. Coldwell, *Nucl. Instr. and Meth.* **A242** (1986) 455

[ii] R.L. Coldwell and G.J. Bamford, *The Theory and Operation of Spectral Analysis Using Robfit*, AIP, New York (1991) pp. 50-58

[iii] E, Browne and Richard B. Firestone; V.S. Shirley, Editor *Table of Radioactive Isotopes*, John Wiley, New York (1986) pp. C-19, C-24.

[iv] C. de Boor, *A Practical Guide to Splines*, Springer-Verlag, New York (1978) p.180

Page intentionally left blank

The INTEGRAL Mass Model and the GGOD M-C Simulation Suite

F. Lei, A.R. Green, A.J. Bird, C. Ferguson, A.J. Dean

Dept. of Physics and Astronomy,
University of Southampton, Southampton, SO17 1BJ, UK

Abstract:

A detailed mass model of the ESA INTEGRAL gamma-ray satellite is being built. It is used as geometric inputs to the comprehensive M-C simulation suite GGOD to form the INTEGRAL mass model simulation software. We present the current status of the mass model project and preliminary background evaluation results for the two main gamma-ray instruments and the use of simulation data-sets in the detector design optimisation process.

1) Introduction:

The INTErnational Gamma Ray Astrophysics Laboratory (INTEGRAL) is the next ESA M2 mission scheduled for launch in the year 2001. It is dedicated to the fine spectroscopy and imaging of celestial gamma-ray sources in the energy range 15 keV to 10 MeV. There are four separate but co-aligned instruments on board: SPI the germanium based spectrometer and IBIS the CdTe/CsI based imager, both coded mask telescopes; the other two are JEM-X, an x-ray monitor, and OMC an optical monitoring camera.

One of the major problems with gamma-ray astronomy is the very low signal to noise ratio, hence the instrument designs need to be optimised to achieve a high detection efficiency to the source photons while maintaining a low background noise level. As with any space based project detailed modelling and Monte Carlo simulation is used as an effective tool in this optimisation process. For example, the detection efficiency can be optimised by modelling the instrument response to various source forms and the instrument background noise can be optimised by modelling the instruments response to the radiation environment to which it has been exposed. For this reason an accurate mass model of the instrument payload and the satellite is crucial as the accuracy of the outcome of the simulation is directly dependent on the precision of the mass model being used.

For the case of INTEGRAL the need for a mass model is not only restricted in the area of simple performance and background modelling. As three of the four instruments are code mask imaging telescopes, the spatial variations in background and detection efficiency across the positional detector planes are important factors in determining the sensitivity of the telescope. Shadowing is another problem that needs to be tacked using a detailed mass model. Due to the penetrating nature of gamma-rays, some of the supporting structure is semi-transparent and so a bright source off-axis may cast a shadow of the support structure, or other instruments, across the detection plane. This super-imposed shadow, if not removed, will ultimately reduce the sensitivity of the telescope.

The production of detector response matrix is another important area in which a detailed mass model is required. The response of SPI and IBIS detectors will be both energy and directional dependent. They will be affected by the existence of the each other as well as the other payloads and the spacecraft platform and structure. It is anticipated that the detailed mass model will be used in the instrument calibration simulation software and the response matrix generation software.

Other usages of the INTEGRAL mass model and simulation software are in the complementarity study and post-launch diagnosis. The four instruments on board are built by different collaborations and the fact that some of the best science will be achieved by combining the data from all instruments. This makes a strong case for an independent assessment of the complementarity and interaction between the instruments. Unlike previous missions there will be no INTEGRAL flight spare, so if problems do arise after launch there will be no physical test-bed. Instead, there will be only the computer based simulation tools. It is an aim of the INTEGRAL mass model to be as detailed as possible by launch to enable testing of new algorithms and trouble-shooting if problem do appear.

2) The INTEGRAL Mass Model - TIMM

2.1 The Spacecraft and Payload Model

A single model down to the millimetric precision is unrealistic to start with, instead different models based on the level of geometrical detail required are defined:

i) The Major Component Model involves detailed modelling of the active detector components and crude modelling of the support structure and non-active components.

ii) The Minor Component Model is similar to the Major Component Model except that material around the detection plane and the spacecraft is modelled in more detail.

iii) The Fine Detail Model provides extra detail about structure which may shadow the detector, e.g. mask support structure, PLM walls, etc.

The isotopic composition of the components will be modelled as accurate as possible, based upon the information provided by the instrument teams. The instrument teams will be alerted of certain type of isotopes which yields significant amounts of background noise even with a very small quantities in a component. **Currently the first version of the Major Component Model has been completed and a few drawings will be shown here.**

2.2 The M-C simulation software

GEANT is the chosen M-C simulation package for TIMM and is also used by both SPI and IBIS modelling teams. The mass model is created in the form of GEANT geometrical files so it can be easily used in various simulation software. The GEANT code models all electro-magnetic interactions from 10 keV to TeVs. Thus it is adequate for the modelling of instrument response to various source photons and for the generation of the detector response matrix of SPI and IBIS.

When come to the evaluation of background noise, however, one will need a code

i) be able to model all relevant particle types over the entire energy range necessary, i.e. photons, electrons, neutrons, protons, alpha, etc.
ii) covers all possible interaction types
iii) follows the transport of the incident particles and their secondaries, through the material of the whole geometrical set-up.
iv) be able to calculate the induced radioactivity.
v) be able to simulate the induced radioactive decays and follow the transport of the decay particle(s).

Although there are many excellent M-C simulation packages available, but not a single code can perform all the tasks outlined above. The solution is to combine the power of different codes. GGOD (GEANT-GCALOR-ORIHET-DECAY) is such a integrated suite of codes that fulfils all the INTEGRAL simulation requirements.

A flow-chart diagram showing the basic layout of the GGOD simulation software is given below:

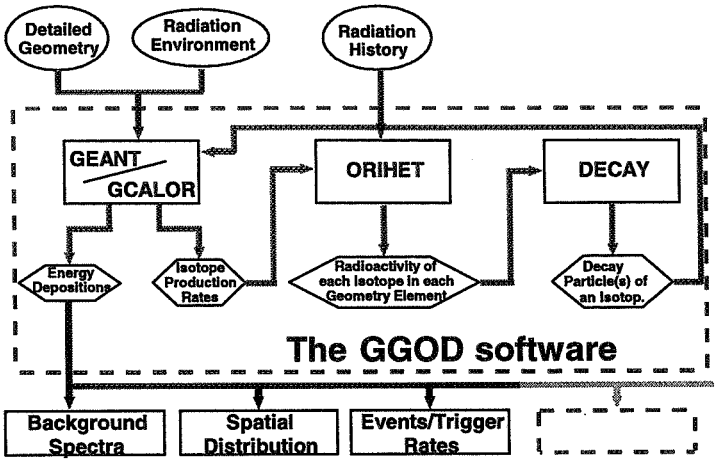

In GGOD, geometry, material modelling and particle transport are dealt in the GEANT/GCALOR code.

Induced radioactivity are calculated by ORIHET, taking the isotope production rates outputted from GEANT/GCALOR simulations and the radiation history of the satellite as inputs. The outcome from ORIHET is a list of radioactive isotopes and their radioactivity at the given time of the satellite history. This is then passed to the DECAY code which generates the expected decay particle(s) for each individual decay, according to the ENSDF radioactive decay schemes. The DECAY code is designed as an event generator for GEANT thus the transport of the decay particle(s) is performed in GEANT.

TIMM background simulation process is rather CPU intensive and cannot be done on a single workstation. Instead a parallel version of GGOD has been developed and implemented in a IBM SP2 machine.

2.3 First results

TIMM background simulations based on the first Major Component Model have been carried out for both solar maximum and minimum cases. **Examples of the background spectra will be given here.**

3) TIMM simulation as a tool to optimise instrument designs:

3.1 To zone or not to zone: the IBIS veto system.

The TIMM simulation estimated trigger rates in the IBIS BGO veto is in the order of 30 k/s at solar min. This, together with the calibration tagging signals, will lead to a dead-time in the order of 20% for IBIS assuming the current veto gate time of 4 us can not be reduced significantly. Various schemes of local or zoned veto have been envisaged so as to reduce the overall dead-time. Any use of a zoned veto system, however will inevitably result in the increase of detector background noise, and reduce the sensitivity of IBIS. The TIMM background simulation data-set enable us to evaluate the impact of various zoned veto scheme to the detector dead time, background noise level and the sensitivity. Preliminary analysis shows that all types of zoned veto schemes will lead to a reduced sensitivity. We are currently investigating an alternative solution of increasing the veto thresholds.

3.2 SPI localised beta component.

The background of the Germanium detectors of SPI is dominated by the induced radioactive decays in the 100 keV to a few MeV energy ranges. If the induced radioactive decays are predominantly localised beta- decays, as suggested by studies carried out by the SPI team, then it is possible to reject this dominant background source by introducing either segmented germanium detector or pulse shape discrimination techniques. In GGOD as the induced radioactive decays are simulated macroscopically, i.e., decays are simulated on individual bases, we can easily evaluate the localised/non-localised ratio of the induced radioactive decay events in this energy range. Early analysis results show that the expected

percentage of localised events is about 50% of the total in the 200 keV to 1 MeV. This is less than the 85% value the SPI team has estimated.

4) SUMMARY

The first version of the Major Component Model of TIMM has been completed and background simulation for solar min and max cases have been carried out. Background spectra for the two main instruments SPI and IBIS have been derived for each data event mode. Studies of the IBIS zoned veto designs have concluded that all zoned veto options will in fact lead to a lower sensitivity. Investigation of the localised induced radioactive decays in the SPI detectors has shown a lower percentage value than what the SPI team has estimated.

Activation in the COMPTEL Double-Scattering Gamma-Ray Telescope

D. J. Morris, M. L. McConnell, J. M. Ryan
Space Science Center, University of New Hampshire, Durham NH 03824-3525 USA

V. Schönfelder, M. Varendorff, G. Weidenspointner
Max-Planck-Institut für extraterrestrische Physik, Postfach 1603, D-85740 Garching, Germany

H. Aarts
SRON-Utrecht, Sorbonnelaan 2, NL-3584 CA Utrecht, The Netherlands

K. Bennett
Astrophysics Division, Space Science Department of ESA/ESTEC, NL-2200 AG Noordwijk, The Netherlands

COMPTEL is a double-scattering telescope designed for gamma-ray astronomy in the energy range 0.75-30 MeV [1]. It has two sets of detector modules arrayed in two planes separated by about 1.5 m (Figure 1). The upper (D1) detector consists of seven cylindrical modules filled with NE213A liquid scintillator, each with radius 13.8 cm and depth 8 cm and viewed by eight photomultipliers around the side. The lower (D2) detector consists of 14 cylindrical NaI modules, each with radius 14 cm and depth 7.5 cm and viewed from below by seven photomultipliers. Each detector is surrounding by plastic charged-particle shields. A photon is detected when it scatters in the D1 detector followed by an interaction of the scattered photon in the D2 detector. Ideally, the scattered photon is absorbed in a D2 module. The total energy measured in the two detectors is then the energy of the incident photon, and the ratio of the energies in the two detectors, together with the interaction locations in the detectors, allow the direction of the incident photon to be localized to a circle on the sky. The time between the two interactions and the pulse shape in the D1 detector are used to discriminate against events which are not caused by single photons from within the telescope's normal field of view, extending about 40° from the telescope axis.

COMPTEL is one of four experiments aboard the Compton Gamma-Ray Observatory (CGRO), which was launched on April 5, 1991 into a circular orbit with inclination 28°. Until the spring of 1997, the altitude of the orbit was maintained between 350 and 450 km. During its first 18 months of operation COMPTEL completed a survey of the gamma-ray sky. This was followed by observations of sources or regions of particular interest. Observing periods typically last one to two weeks, during which the orientation the spacecraft is maintained toward a given point on the sky.

Despite the measures to discriminate against events not produced by celestial photons, the COMPTEL data are dominated by instrumental background. Figure 2 shows a typical count spectrum of acceptable double-scatter events. Most of the events are in a distribution with a smooth, exponential decline following the sharp rise near the energy threshold. These events are mostly prompt background, which is the subject of another talk at this conference (J.. M. Ryan *et al.*), though a significant fraction is photons from an isotropic flux of cosmic origin [2]. There are two very prominent peaks on top of this smooth spectrum. At 2.2 MeV is the deuterium formation line from the combination of thermal neutrons with hydrogen in the NE213A liquid scintillator [3]. There is a less well understood feature near 1.4 MeV. Part of it is due to the decay of ^{40}K in the D1 photomultiplier tubes, but the feature is too wide and too large to be explained by this single decay line.

There are also smaller features which can be attributed to the activation of various isotopes with halflives ranging from minutes to years. The activation takes places principally in aluminum, which makes up most of the housings of the D1 modules and the D1 support structure. Two such features were recognized early in the mission and can be see in Figure 2, near 2.8 MeV and 3.9 MeV. Both are attributed to ^{24}Na which is produced in the reaction

$^{27}Al(n,\alpha)^{24}Na$. The ^{24}Na decays with a halflife of 15 hr, simultaneously emitting photons of energies 1.37 MeV and 2.75 MeV. The features result from absorption of the 2.75 MeV photon in D2 together with the scattering of the 1.37 MeV photon in D1. The higher energy feature corresponds to the Compton edge for the 1.37 MeV photon. The converse reaction, with absorption of the 1.37 MeV photon in D2, may contribute to the 1.4 MeV feature.

Identification of less significant features requires a detailed examination of the data. Selecting certain periods or subsets of the data can accentuate activation features. Activation features can also be identified by looking at the relative size of the energy deposits in the two detectors or the distribution of the interaction locations within the detector modules. Individual activation lines can be identified as photopeaks in energy spectra from the D2 modules alone. These methods are used in conjunction with Monte Carlo simulations of activation events, which may involve bremsstrahlung photons from beta-decay electrons and positron-annihilation photons, as well as direct nuclear-decay photons.

Short-lived isotopes are most evident in periods following passage of the spacecraft through the large proton fluxes of the South-Atlantic Anomaly (SAA). Figure 3 shows, for one two-week observation period, the excess counts in summed 30-minute periods following each SAA passage relative to the remainder of the observation. Short-lived activation is evident at energies up to about 4 MeV, with two possible activation features below 2 MeV. One feature, near 1.1 MeV, is tentatively attributed to ^{27}Mg, with a halflife of 9.5 min, while the other may be due to ^{24}Na. The level of short-term activation may be understated in Figure 3 due to confusion with the prompt background, which is modulated by the geomagnetic cutoff rigidity. Prompt background is relatively low in the periods following SAA passages, which explains the negative counts above 4 MeV. Data from additional observations and for periods of different lengths following the SAA passages is being examined to better characterize the short-lived activation.

Long-lived isotopes accumulate over the lifetime of the experiment at a rate which depends on both the spacecraft altitude and solar modulation of the cosmic-ray flux. As these isotopes accumulate their associated features in the COMPTEL data grow in strength. Comparison of data from different epochs can reveal long-lived activation, though direct comparison of spectra is complicated by long-term changes in the instrument response. Fits of the spectra up to 2.6 MeV with a smooth underlying background plus two Gaussians, revealed the growth of the feature near 1.4 MeV in both width and amplitude since launch. Features associated with the isotope ^{22}Na (halflife 2.6 yr) have also been identified near 1.4 MeV, but a complete explanation for the 1.4 MeV feature has not yet been achieved.

1. V. Schönfelder *et al.*, "Instrument Description and Performance of the Imaging Gamma-Ray Telescope COMPTEL aboard NASA's Compton Gamma-Ray Observatory", *Astrophys. J. Suppl.*, **86**, 657 (1993).

2. C. Kappadath *et al.*, "The Preliminary Cosmic Diffuse γ-Ray Spectrum from 800 keV to 30 MeV Measured with COMPTEL", submitted to *Astron. Astrophys.*

3. G. Weidenspointner *et al.*, "The Local Neutron Flux at Low Earth Orbiting Altitudes", submitted to *Advances in Space Research.*

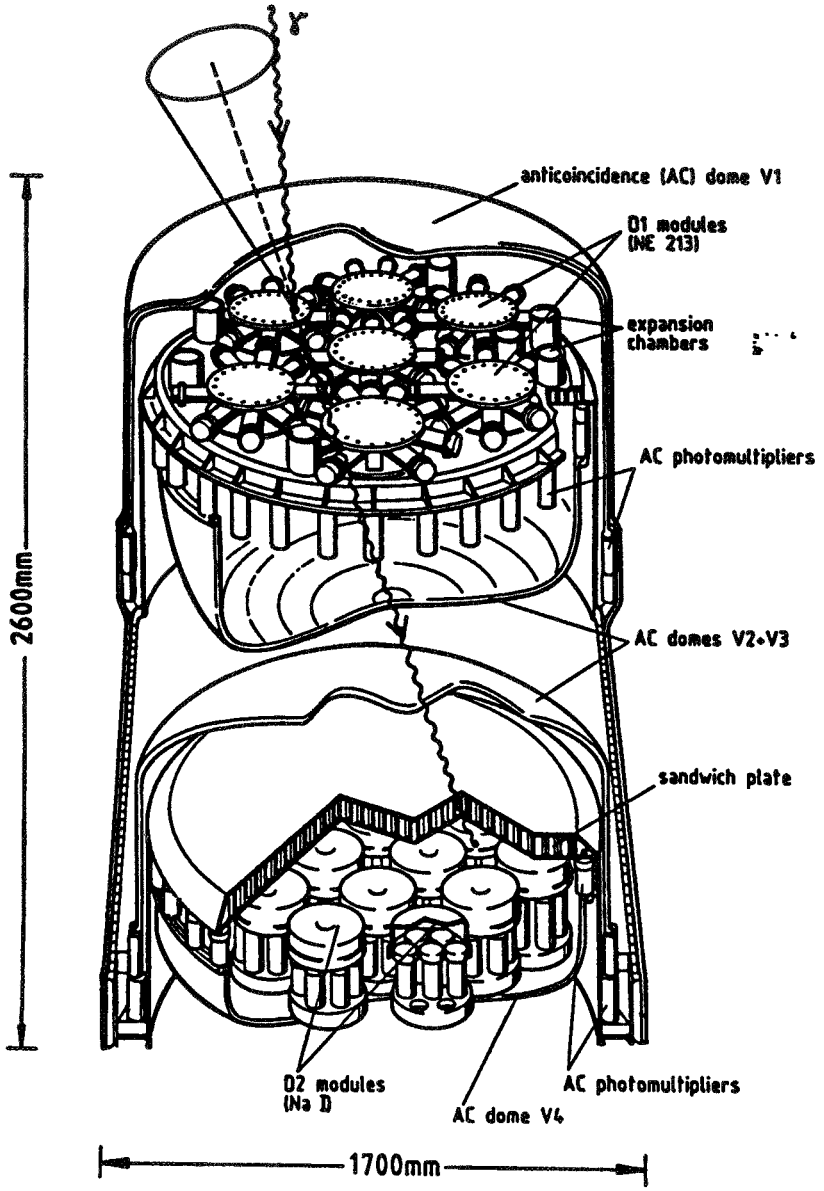

Figure 1: Schematic diagram of the COMPTEL double-scattering gamma-ray telescope.

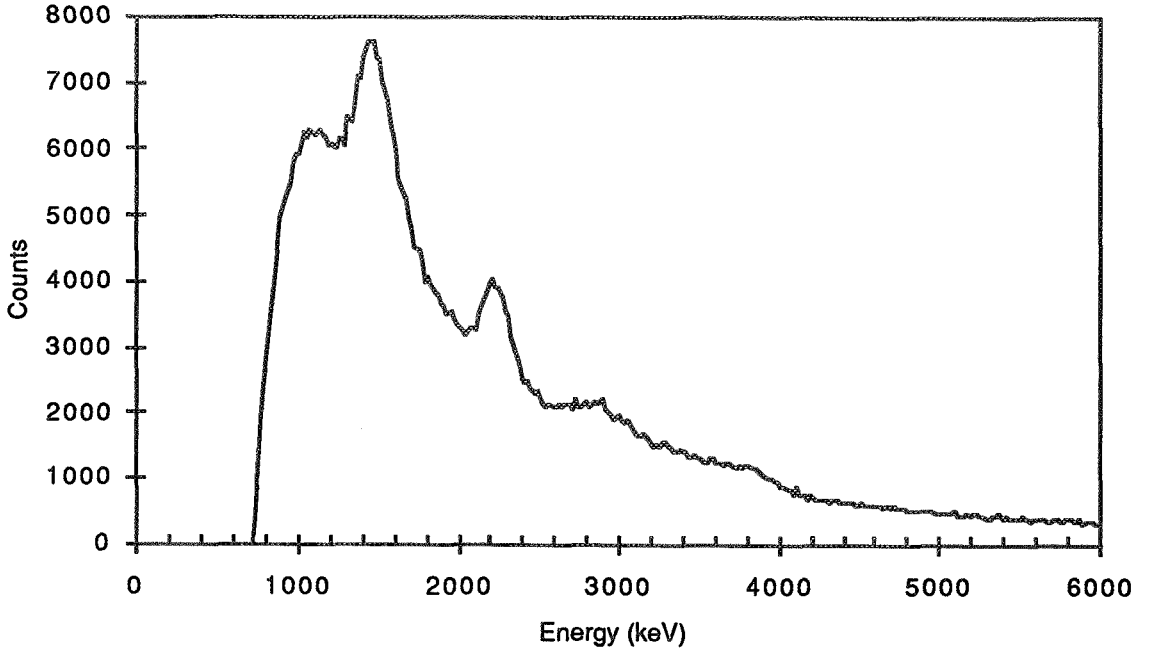

Figure 2: A typical energy spectrum of double-scatter events.

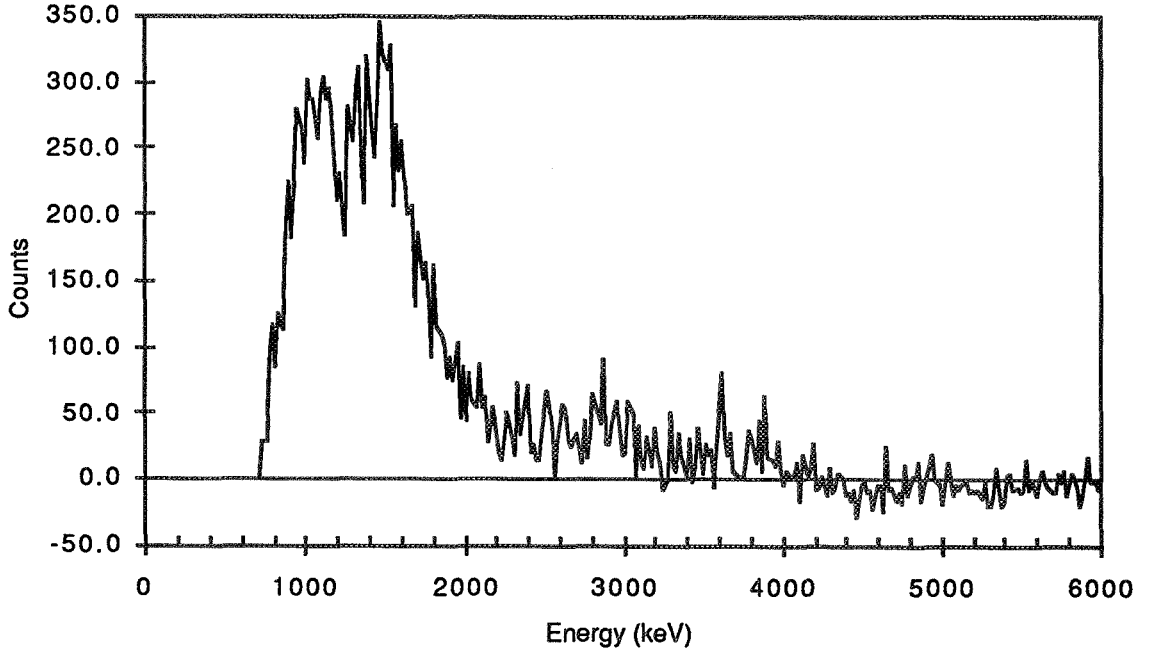

Figure 3: Excess events in the 30 min. following SAA passages during one observation.

RADIATION THREATS FROM HUGE SOLAR PARTICLE EVENTS*,

Robert C. Reedy, MS D436, Los Alamos National Lab., Los Alamos, NM 87545 USA (Tel. 505-667-5446; fax 505-665-4414; e-mail: rreedy@lanl.gov)

Among the natural sources of energetic particles in space, the main radiation threats are the galactic cosmic rays (GCRs), solar energetic particles (SEPs), and trapped radiation around planets. All are very serious sources of radiation, especially away from the Earth's strong magnetosphere for SEPs [e.g., 1–3]. However, over a short period of time (only a few days), the effects from a huge solar particle event (SPE) can be far greater than from any other nature source of radiation. Effects of large SPEs include high doses to humans [2], microelectronics [3], and solar panels [4].

The nature of GCRs is well known as is the variation in their flux over a typical 11-year solar activity cycle. The models for the Earth's trapped radiation belts are not good, but a number of recent satellites are helping to map the spatial and temporal variations of the fluxes and spectral shapes of trapped energetic particles. The radiation threats from GCR or trapped particles can be very serious, but the data to plan for ways to manage them are in good shape. The radiation threat that is least known is that from the huge solar particle events that occur, on average, about once a decade or from even larger and rarer events. This paper reviews SPEs, what is known about them (especially huge events), and what needs to be done to have better confidence in planning for missions to survive huge SPEs.

SPEs in General

Before direct measurements of solar energetic particles by spacecraft, a few observation were made using instruments on the Earth's surface that detected ionization, neutrons, or radio disturbances caused by the high-energy particles in an SPE [5]. Routine studies of SPEs started around the time of the International Geophysical Year in 1957–1958. It wasn't until 1965 that continuous measurements of SEPs by spacecraft outside of the Earth's magnetosphere were made [5].

SEPs have energies from ~1 MeV to hundreds of MeV with the flux dropping rapidly with increasing energy [6]. Some events can have "relativistic" particles ($\gtrsim$1 GeV), and only such very-high energy particles can produce effects observable at the Earth's surface, such as in neutron monitors [7]. The peak fluxes during a SPE last only a few hours, and a SPE lasts only a few days to a week or two. The nuclei in a SPE are ~98% protons and a few heavier nuclei [6] with an alpha-particle/proton ratio of $\approx$60.

Solar particle events tend to occur when the Sun is away from it period of lowest activity. Few large SPEs are observed in the $\approx$4 years of lowest solar activity (fewest sunspots) [8,9]. During the remaining $\approx$7 years of a typical 11-year solar cycle, large SPEs can occur any time. The largest SPEs tend to occur after the maximum in sunspot numbers (the "declining phase" of the solar cycle) [9], but some huge SPEs (such as 23 Feb. 1956) occurred before solar maximum. The exact causes of large SPEs are still being debated by some, but the earlier theory associated them with solar flares now is being replaced with strong shocks in fast coronal mass ejections as the main cause of high fluxes of energetic particles [e.g., 10].

Most SEPs have enough energy to induce nuclear reactions in material into which they penetrate. Many nuclides have been observed as having been produced by SEPs in lunar samples [e.g., 11]. Solar-proton-produced radionuclides with half-lives up to 3.7-Myr ^{53}Mn have been observed in lunar samples, and some stable nuclides such as ^{21}Ne made by solar protons also have been studied [12]. When cross sections to unfold the data are available, these SEP-produced nuclides have been used to infer the average flux of solar protons over various time periods determined by the half-life of the radionuclide [11] or the surface exposure age of the lunar rock [12]. Such "fossil" records enable us to study the long-term record of SEPs.

Modern Solar Particle Events

The event-integrated fluences of SEPs have been compiled by several authors for SPEs since 1956 [e.g., 8,13,14]. Figure 1 [15] shows a plot of event-integrated solar-proton fluences since 1954 for protons with energies above 10 and 30 MeV. The fluences before 1965 are based on indirect measurements of relative fluences and activities of ^{22}Na in lunar rocks [14]. Many events since 1989 are not in this plot as fluences for these events have not been reported in the literature.

Statistics on solar proton events since 1956 have been studied [8] and used to develop a model for fluences of solar protons [16]. This model is better than some older ones [e.g., 17] in that it included events from almost four full solar cycles and properly included the rare but important huge events, such as those in 2/56 (with its many relativistic protons), 7/59, 11/60, 8/72, 8/89, 10/89, and 2/91.

One problem in modeling SPEs has been that huge events, which have event-integrated 4π (omnidirectional) fluences above 10 MeV of $\sim 10^{10}$ protons/cm^2, have been rare. Thus the statistics for such events are fairly uncertain. A few decades ago, some authors even proposed that events many orders of magnitude larger than these could occur very rarely. Now that there is more measurements, it is generally accepted that events an order of magnitude larger than those recently observed do not occur or are exceeding rare.

Ancient Fluxes of Solar Particles

The production of nuclides in lunar samples has been known since the first samples returned by Apollo 11 in 1969 [14,11]. However, even a decade ago, cross sections did not existed for unfolding the records of many of the SEP-produced radionuclides [11]. Several groups are now measuring the needed cross sections. Thus the results mentioned below are not final. However, preliminary studies with the newest cross sections show that the results for solar-proton fluxes over various time periods are known much better than a factor of two.

Besides cross sections, other uncertainties in studying the fossil record of SEPs are corrections for nuclide production by GCR particles and effects of the erosion of the surfaces of lunar rocks by micrometeoroids ($\sim$1 mm/Myr) [11,12]. Because of these uncertainties, it has been difficult to get good fluxes and spectral shapes from the lunar fossil record. Recently, several radionuclides, especially 1.5-Myr ^{10}Be, have been shown to be very sensitive to the spectral shape of solar protons [18].

Lunar SEP-produced nuclides only give an average flux of solar protons over the mean-life of the radionuclide or the surface-exposure age of the sample. The average flux of solar proton over the last few million years is about 100 protons/cm^2/s with most nuclides giving fluxes within about 50% of this value [11,12]. This flux is similar to that from modern SPEs averaged over the four decades during which they have been observed.

The Complete SPE Record

While the similarity of modern and ancient SEP fluxes has been known for over two decades, few have tried to combine both data sets. Many have plotted events per year above a given fluence versus event fluence, but few have added the ancient record. Figure 2 [from 15] shows a plot of events per year above a given fluence F versus the event fluence F for the modern record. The point for 3–10$\times 10^{10}$ protons/cm^2 is an upper limit of one over the last four decades as no event of this fluence or greater has been observed.

A similar plot was given by [19], but they also used a limit on large SPEs using measurements for ^{14}C in tree rings over the last 7000 years. Their point based on ^{14}C is in Fig. 2. Also shown are several points using the lunar record discussed above. The limits using the lunar data assume that all of the activity of the various radionuclides was made by a single, huge event a half-life of that radionuclide ago, an extreme assumption but clearly a limiting case [15].

Figure 2 shows that there has to be a sharp break in the probability plot of SPE fluences at $\sim 3 \times 10^{10}$ protons/cm^2. Thus models like [16] using the modern record over the last four decades should be good for long time periods. While an event of such a fluence is a serious radiation hazard [e.g., 1–4], it is good to know that events even only an order of magnitude greater than any seen since 1956 are very unlikely.

Summary

Both the modern and ancient records for solar energetic particles have been very quickly reviewed above. High fluxes of solar energetic particles are serious radiation hazards in space. The main conclusion is that huge solar particle events should be extremely rare and that recent models for SPE fluences such as [16] should be good guides in planning future deep space missions. However, the record for SEPs is not complete. More work is needed on both the modern and ancient records.

The modern record is fairly good since 1965, although several reports of event-integrated fluences differ for some events by up to about 50%. More data sets that can be used to get modern SPE fluences need to be studied to improve the very recent record. The record from 1956 to 1962 is less certain, and reported SEP fluxes, and SPE fluences different by factors of many. Earth-based measurements need to be examined to give good fluences, especially relative ones. These data sets can then be used with lunar short-lived radioactivity measurements, as in [14], to check the absolute fluxes for this period.

The fossil record is also improving, with new measurements of SEP-produced nuclides in lunar rocks and of the cross sections for making these nuclides by protons. Better models to use in making corrections for production by galactic-cosmic-ray particles are also being developed. Within a few years, many newer and better fluxes should be available from the lunar fossil record for SEPs.

References:

[1] R. Silberberg, C.H. Tsao, J.H. Adams, and J.R. Letaw (1989), "High-energy radiation environment during manned space flights," in *High Energy Radiation Background in Space* (AIP Conf. Proc. 186), pp. 146–158.

[2] J.R. Letaw, R. Silberberg, and C.H. Tsao (1989), "Radiation hazards on space missions outside the magnetosphere," *Adv. Space Res.*, **9**, (10)285–(10)291.

[3] C. Tranquille (1994), "Solar proton events and their effect on space systems," *Radiat. Phys. Chem.*, **43**, 35–45.

[4] D.C. Marvin and D.J. Gorney (1991), "Solar proton events of 1989: Effects on spacecraft solar arrays," *J. Spacecraft Rockets*, **28**, 713–719.

[5] M.A. Shea and D.F. Smart (1995), "History of solar proton event observations," *Nucl. Phys. B (Proc. Suppl.)*, **39a**, 16–25.

[6] D.F.Smart and M.A. Shea (1989), "Solar proton events during the past three solar cycles," *J. Spacecraft Rockets*, **26**, 403–415.

[7] M.A. Shea and D.F. Smart (1992), "Recent and historical solar proton events," *Radiocarbon*, **34**, 255–262.

[8] J. Feynman, T.P. Armstrong, L. Dao-Gibner, and S. Silverman (1990), "New interplanetary proton fluence model," *J. Spacecraft Rockets*, **27**, 403–410.

[9] M.A. Shea and D.F. Smart (1995), "A comparison of energetic solar proton events during the declining phase of four solar cycles (cycles 19–22)," *Adv. Space Res.*, **16**, (9)37–(9)46.

[10] S. Kahler (1994), "Injection profiles of solar energetic particles as functions of coronal mass ejection heights," *Astrophys. J.*, **428**, 837–842.

[11] R.C. Reedy and K. Marti (1991), "Solar-cosmic-ray fluxes during the last ten million years," in *The Sun in Time* (U. Ariz. Press), pp. 260–287.

[12] M.N. Rao, D.H. Garrison, D.D. Bogard, and R.C. Reedy (1994), "Determination of the flux and energy distribution of energetic solar protons in the past 2 Myr using lunar rock 68815," *Geochim. Cosmochim. Acta*, **58**, 4231–4245.

Page intentionally left blank

LONG-TERM ENERGETIC-PARTICLE DATABASES FROM GEOSYNCHRONOUS AND GPS ORBITS*, Robert C. Reedy, Richard D. Belian, Thomas E. Cayton, Michael G. Henderson, John C. Ingraham, Michael M. Meier, Geoffrey D. Reeves, and Loretta A. Weiss, MS D436, Los Alamos National Laboratory, Los Alamos, NM 87545 USA (Tel. 505-667-5446; fax 505-665-4414; e-mail: rreedy@lanl.gov)

Since the Vela satellites, first launched in 1963, Los Alamos has had a number of instruments in space to measure energetic radiations from nuclear tests, such as x rays, neutrons, and gamma rays. It soon became clear that we also needed instruments dedicated to the study of the space environment, including energetic particles and the plasma.

Energetic particles in space can induce some serious radiation effects in spacecraft. Electrons with energies above about 10 keV can charge the surfaces of spacecraft and change the surface potential. Relativistic electrons (energies $\gtrsim$1 MeV) can penetrate deep into material and create hazardous deep dielectric charging. High fluxes of solar energetic particles can create anomalies in electronics and degrade the performance of solar panels and other spacecraft components. A good knowledge of the temporal and spatial variations of these energetic particles is needed in planning future spacecraft and in understanding the Earth's space environment.

Energetic particle and plasma measurements by Los Alamos in space began with the second Vela satellite launch in 1963. Since then, Los Alamos has had energetic-particle instruments on twelve spacecraft at geosynchronous orbit since 1976 and on seven satellites of the Global Positioning System (GPS) since 1983. Data from these and other instruments, such as plasma analyzers, have been sent to Los Alamos for processing and analysis. Databases using these data have been or are being established at Los Alamos and are described here.

Los Alamos Energetic-Particle and Plasma Instruments

The first Los Alamos energetic-particle instrument with a large database is the Charged Particle Analyzer (CPA) [1,2], which has been on eight satellites at geosynchronous orbit (6.62 Earth radii, R_E) since 1976. CPA instruments on two satellites continue to generate data. The instrument consists of four subassemblies or units based on one or more semiconductor or scintillator detector elements. Each unit was designed for a specific particle (electron or proton) and energy range (low or high). The LoE electron unit has six nominal energy levels from 30 to 200 keV with an upper threshold of 300 keV. The HiE electron unit has six energy levels from 0.2 to 1.4 MeV with an upper-energy cutoff of 2.0 MeV. The LoP proton unit has a lowest threshold that varies among the different instruments in orbit between 0.07 to 0.15 MeV, with an upper threshold of $\sim$0.6 MeV. The HiP unit has nominal proton energy thresholds from 0.4 to 100 MeV with an upper-energy cutoff of 150 MeV, providing 16 differential channels.

In 1989, the CPA was replaced as the Los Alamos energetic-particle instrument on geosynchronous satellites with the Synchronous Orbit Particle Analyzer (SOPA). The SOPA instrument consists of three nearly-identical silicon solid-state-detector telescopes [3]. The SOPA instruments have nine differential channels for electrons from 50 keV to 1.5 MeV and an integral electron channel above 1.5 MeV. It also has 12 differential channels for protons from 50 keV to 50 MeV and eleven channels for particles heavier than protons (alpha particles to strontium). Data have been returned from SOPAs on four geosynchronous satellites.

Higher-energy particles have been measured using another set of instruments. From 1979 to 1989, the Spectrometer for Energetic Electrons (SEE) was flown on several geosynchronous satellites along with the CPA instrument. In 1989, this instrument was replaced with the Energy Spectrometer for Particles (ESP). The ESP instrument is a bismuth germanate crystal coupled to a thick plastic scintillator that in turn is coupled to a photomultiplier tube [4]. The ESP instrument can measure electrons from 0.7 to 26 MeV and protons from 11 to >20 MeV.

Instruments to measure the electrons and ions associated with the plasma at geosynchronous orbit have also been on the later geosynchronous satellites. The current plasma instrument, the Magnetospheric Plasma Analyzer (MPA) [5], measures electrons from 70 eV to 44 keV and ions from 90 eV to 43 keV. The MPA can be used to extend the measurements by the CPA or SOPA to lower energies and to study the behavior of the plasma in the vicinity of these spacecraft.

Some satellites of the Global Positioning System (GPS) carry a Burst Detector Dosimeter (BDD). The GPS satellites are in 12-hour orbits at 4.1 R_E, which takes them into the heart of the trapped electron radiation belt four times per day. Two of the Block I GPS satellites carried a BDD–I instrument: Navstar–8 (NS08), which returned data from August 1983 until April 1984, and NS10, which returned data from October 1984 until November 1992. The BDD–I [6] consisted of silicon sensors under four domes. Holes in the domes allowed only a small fraction of the incident radiation to get inside the dome, where different filters gave four energy ranges. Electrons channels had lower thresholds of about 0.5, 1.0, 2.0. and 4 MeV. Proton channels had lower thresholds of about 6, 10, 15, and 15.5 MeV.

On five Block II GPS satellites, a BDD–II was or is being flown: NS18 (Feb. 90 – May 94), NS24 (Aug. 91 – present), NS28 (Apr. 92 – Oct. 96), NS33 (Apr. 96 – present) and NS39 (July 93 - present). The BDD–II consists of two sensor assemblies, one under a solid dome and one with 15 holes [7]. The active sensor part has nested pairs of scintillators each viewed by a microchannel plate photomultiplier tube. The BDD–II has seven electron channels from 0.2 to >5.9 MeV and four proton channels from 9 to >50 MeV. Three GPS satellites launched from 1997 until about 2000 as part of GPS Block IIR will include a new version of the BDD, the BDD–IIR. Later GPS satellites of Block IIR and then Block IIF will carry a Combined X-ray Dosimeter instrument, which will continue our coverage of energetic particles at GPS orbits to well into the next century.

The BDD data are stored in on-board memory and downlinked once per day during routine contact with the satellite. The ground station formats the BDD data into an EPRO (End PROduct) file that comes to Los Alamos over a network.

Los Alamos Energetic-Particle Databases

The energetic-particle data since 1979 from the CPA and SOPA instruments on geosynchronous satellites have been incorporated in a database at Los Alamos. This digital database is stored on-line using a SUN workstation and 12 GB of hard disk storage [8,9]. The workstation is *leadbelly.lanl.gov*, which has the internet node number 128.165.207.108. A single data file is stored for each satellite for each day. This database is available over the "World Wide Web" [8,9] with the "home page" *http://leadbelly.lanl.gov/lanl_ep_data/lanl_ep.html* and includes the energetic-particle fluxes and supplementary information, such as how to use the database. The plasma data from the MPA instruments for the same period can be accessed from this site. This energetic-particle database is being expanded and is used as part of the International Solar Terrestrial Physics program for studies using many satellites in various orbits and as part of the National Space Weather Program to understand the space environment around the Earth. In addition, the data is supplied to the U.S. Air Force's Space Weather Forecasting Center for their use.

The energetic-particle data from the BDD instruments on GPS satellites are being compiled into another database. At Los Alamos, the BDD EPROs (End PROducts) are unpacked, converted to counting rates, and written as ASCII files, one file per satellite per GPS-week (a new GPS-week begins at 00:00 UT each Sunday). Time, geographic coordinates, and a set of geomagnetic coordinates computed from the Tsyganenko-89-model field, are appended to the energetic-particle data to aid the interpretation of the measurements from the 55°-inclined, 4.1-R_E, circular GPS orbit.

Summary

Instruments designed and built by the Los Alamos National Laboratory have provided an extensive set of data on the fluxes of energetic particles at geosynchronous orbit since 1976 and in the orbit of Global Positioning System satellites since 1983. This continuous record is valuable for long-term studies of energetic particles in important regions of the Earth. Energetic particles can induce serious radiation effects in spacecraft. Our long-term databases are useful in studying these particles and many times showing the cause of these radiation effects.

Many studies have been and can be done using these databases. For example, fluxes of relativistic electrons measured since 1979 showed that their fluxes varied with a cycle of about 10.5 years but out of phase with the sunspot cycle (having higher fluxes near periods of minimum solar activity) [10]. The large solar particle events in 1989 were studied using data from CPA instruments [11]. Combining data from geosynchronous orbit with those from other orbits, such as GPS, is helping researchers to understand the dynamics of energetic particles in the Earth's magnetosphere. With these databases coming "on line," others now can use them in their studies of energetic radiations in the Earth's environment.

References:

[1] P. R. Higbie *et al.* (1978), "High resolution energetic particle measurements at 6.6 Re, 1, electron micropulsations," *J. Geophys. Res.*, **83**, 4851–4855.

[2] D. N. Baker *et al.* (1979), "High-energy magnetospheric protons and their dependence on geomagnetic and interplanetary conditions," *J. Geophys. Res.*, **84**, 7138–7154.

[3] R. D. Belian *et al.* (1992), "High-Z energetic particles at geosynchronous orbit during the great solar proton event series of October 1989," *J. Geophys. Res.*, **97**, 16897–16906.

[4] M. M. Meier *et al.* (1996), "The Energetic Spectrometer for Particles (ESP): Instrument description and orbital performance," in *Workshop on the Earth's Trapped Particle Environment*, AIP Conf. Proc. 383, pp. 203–210.

[5] D. J. McComas *et al.* (1993), "Magnetospheric Plasma Analyzer (MPA): Initial three-spacecraft observations from geosynchronous orbit," *J. Geophys. Res.*, **98**, 13453–13465.

[6] D. M. Drake *et al.* (1993), "Experimental evaluation of the BDD-I dosimeter for the Global Positioning System," *Nucl. Instrum. Methods Phys. Res.*, **A333**, 571–588.

[7] W. Feldman *et al.* (1985), "The BDD II: An improved electron dosimeter for the Global Position System," Los Alamos National Laboratory report LA–10453–MS.

[8] G. D. Reeves *et al.* (1996), "Los Alamos geosynchronous space weather data for radiation belt modeling," in *Radiation Belts: Models and Standards*, AGU Geophysical Monograph 97, pp. 237–240.

[9] G. D. Reeves *et al.* (1996), "Los Alamos space weather data products: On line and on time," in *Proceedings of the Third International Conference on Substorms*, ESA report SP–389, pp. 689–694.

[10] R. D. Belian *et al.* (1996), "Long term behavior of trapped relativistic electrons and their correlation with solar wind speed," in *Solar Drivers of Interplanetary and Terrestrial Disturbances*, Astron. Soc. Pacific Conf. Series Vol. 95, pp. 429–436.

[11] G. D. Reeves *et al.* (1992), "The great solar energetic particle events of 1989 observed from geosynchronous orbit," *J. Geophys. Res.*, **97**, 6219–6226.

* Work support by the DOE and NASA and done under the auspices of the U.S. Dept. of Energy.

[13] M.A. Shea and D.F. Smart (1990), "A summary of major solar proton events," *Solar Phys.*, **127**, 297–320.
[14] R.C. Reedy (1977), "Solar proton fluxes since 1956," in *Proc. 8th Lunar Sci. Conf.* (Pergamon Press), pp. 825–839.
[15] R.C. Reedy (1996), "Constraints on Solar Particle Events from Comparisons of Recent Events and Million-Year Averages," in *Solar Drivers of Interplanetary and Terrestrial Disturbances* (ASP Conf. Series Vol. 95), pp. 429-436.
[16] J. Feynman, G. Spitale, and J. Wang (1993), "Interplanetary proton fluence model: JPL 1991," *J. Geophys. Res.*, **98**, 13281-13294.
[17] J.H. King (1974), "Solar proton fluences for 1977–1983 space missions," *J. Spacecraft Rockets*, **11**, 401–408.
[18] K. Nishiizumi *et al.* (1988), "^{10}Be profiles in lunar surface rock 68815," in *Proc. 18th Lunar Planet. Sci. Conf.* (Cambridge U. Press), pp. 79–85.
[19] R. E. Lingenfelter and H. S. Hudson (1980), "Solar particle fluxes and the ancient sun,"in *The Ancient Sun* (Pergamon Press), pp. 69-79.
* Work support by NASA and done under the auspices of the U.S. Dept. of Energy.

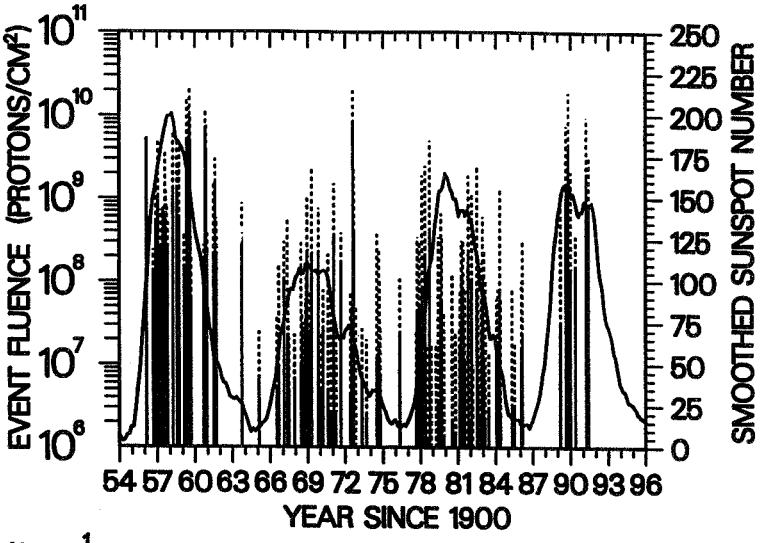

Figure 1. Smoothed monthly sunspot numbers (curve) and event-integrated solar-proton fluences above 10 MeV (dashed lines) and 30 MeV (solid lines) for recent solar particle events [from 15].

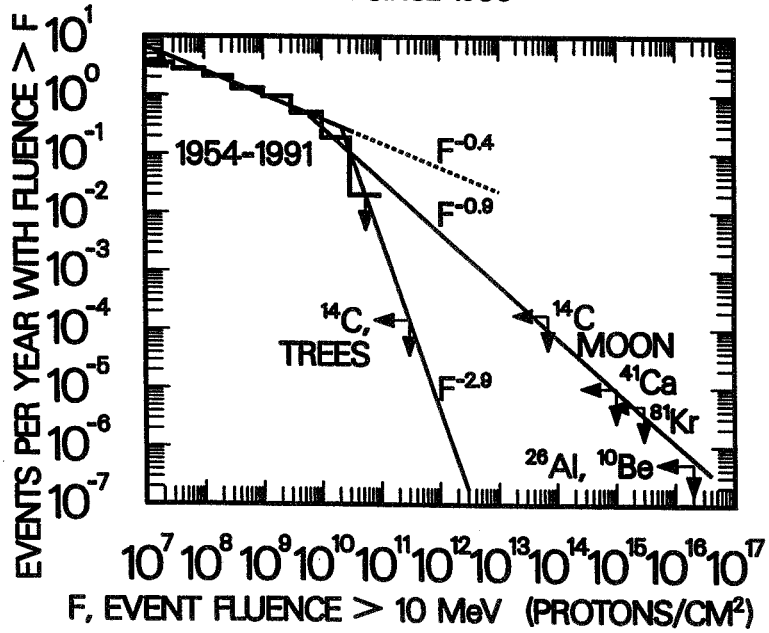

Figure 2. Probabilities of solar particle events with fluences above a given value occurring per year versus the fluences for both modern events and for limits determined from various fossil records [from 15].

The Prompt Cosmic-Ray-Induced Background in the Orbiting Compton Telescope COMPTEL

J.M. Ryan[1], S. Kappadath[1], M. McConnell[1], D. Morris[1], V. Schönfelder[1], M. Varendorff[2], G. Weidenspointner[2], W. Hermsen[3], K. Bennett[4]

[1]Space Science Center, University of New Hampshire, Durham, NH, 03824
[2]Max-Planck-Institut für Extraterrestrische Physik, Postfach 1603, Garching-bei-München, Germany
[3]Space Research Organization Netherlands–Utrecht, Sorbonnelaan 2, NL-3584 CA, Utrecht, The Netherlands
[4]Astrophysics Division, ESTEC, P.O. Box 299 NL-2200 AG Noordwijk, The Netherlands

Summary

One of the major objectives of the COMPTEL experiment on the Compton Gamma Ray Observatory is the measurement of the cosmic diffuse gamma ray flux. One of the advantages enjoyed by COMPTEL is that it experiences a varying background environment that, in principle, some of this background can be extrapolated to zero. Another paper in this session deals with the portion of the background that either builds up or is not modulated.

As it orbits the earth on the Compton Observatory, COMPTEL often views (toward the local zenith) the high galactic latitude portions of the sky free from contamination of gamma rays emerging from the earth's atmosphere. It is these data that we use to measure the cosmic diffuse gamma ray flux. However, because of other particles hitting either the instrument or the spacecraft, multiple gamma rays are generated that "simultaneously" interact with the independent detectors that constitute the COMPTEL instrument. These coincident gamma ray interactions in the independent detectors of COMPTEL give rise to gamma-ray events that pass all the logic and electronic criteria for a legitimate event. The gamma-ray emissions fall into two categories. The first is the decay of metastable nuclei that are activated by bombardment by cosmic rays. The other, the topic of this paper, is the photons that come from cascading de-excitation of nuclei excited by cosmic rays. In this latter case nuclei are excited into high quantum states (or the continuum) and they de-excite by multiple photon emission on very short time scales. The photon emission from this process should closely track the local and instantaneous cosmic ray intensity.

The operation of COMPTEL has been described by Schönfelder et al. (1993). A gamma ray scatters in D1, the forward low-Z scintillation detector. It scatters again in D2, the rearward high-Z scintillation detector. The event is accepted if both scintillations are above threshold and occur within 10 ns of one another with the D1 signal occurring first. Additionally, no signal from the surrounding charged particle shields is allowed within ~ 100 ns of the coincidence. Photon showers from a de-exciting nucleus can therefore produce acceptable signals in the instrument with a broad range of time-of-flight values (from D1 to D2). The excited nucleus, if it is within the instrument, must arise from a fast neutron interaction since proton-induced events are rejected by the charged-particle shields. If a neutron interaction occurs in the mass directly associated with the D1 detectors the consequent "gamma-ray" event will have precisely the correct time-of-flight to be accepted as a cosmic photon. Figure 1 shows the distribution of time-of-flight values from high-galactic-latitude observations. The gaussian peak corresponds to the correct gamma-ray time-of-flight from D1 and D2, but it contains not only good cosmic photons but local cascade events produced around the D1 detectors. The underlying continuum contains contributions from accidental coincidences (flat baseline) and from other cascade events (declining curve) that are broadly distributed in time-of-flight.

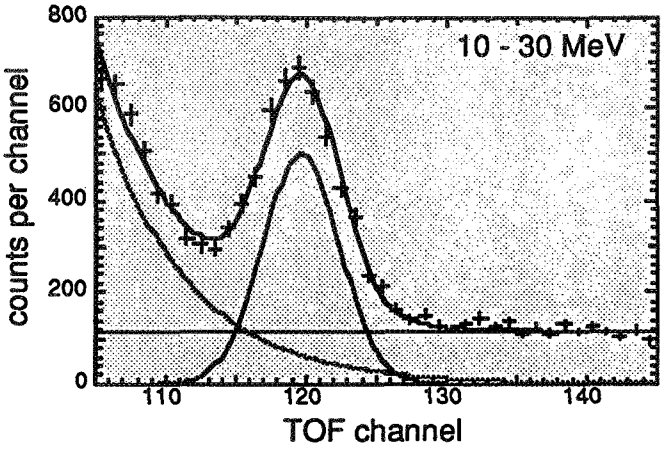

Figure 1. The measured time-of-flight distribution of accepted gamma-ray events.

Proton-induced reactions are also possible sources of these showers if they occur outside the instrument away from COMPTEL's shields and do not produce secondaries that trigger the shields. The fast neutrons must be of secondary origin, whereas the protons may be either primary or secondary cosmic rays. The secondary component originates from both the earth's atmosphere and the spacecraft, but its intensity tracks the intensity of the primary component.

The charged-particle shields not only suppress proton-induced background but also provide a measure of the local cosmic ray intensity. Shown in Figure 2 is the acceptable gamma-ray count rate plotted as function of the charged-particle count rate in four independent shields for the gamma-ray energy range of 10–30 MeV. We see that the gamma-ray count rate is a linear function of the cosmic-ray count rate, but it does not extrapolate to zero gamma-ray count rate for the case of no incident primary cosmic rays. This pedestal serves as a measure of the cosmic diffuse gamma ray flux.

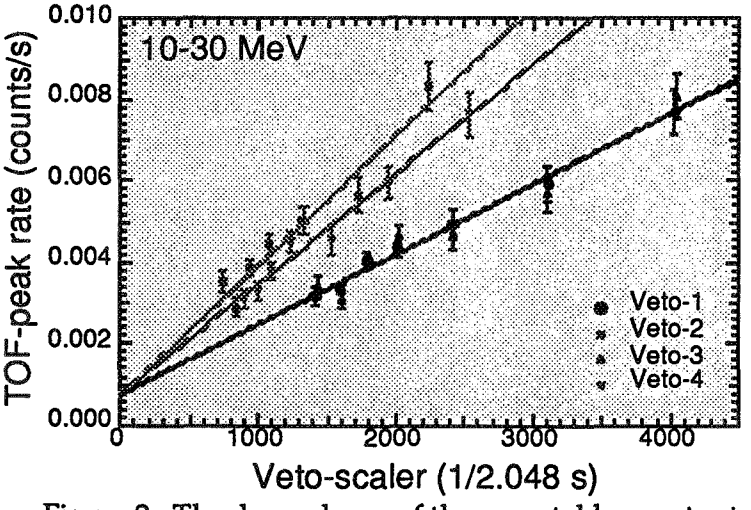

Figure 2. The dependence of the acceptable event rate on the primary cosmic-ray intensity.

For each energy band we can construct such a dependence of the acceptable gamma-ray event rate on the local cosmic-ray intensity. The intercept of the lines on the ordinate once corrected for longer-lived background components can be used to compute the cosmic diffuse gamma-ray flux spectrum. However, the slope of each of these lines is a direct measure of the rate of neutron (or proton) induced cascade gamma-ray events in that energy range. Shown in Figure 3 is the unnormalized spectrum of these cascade multiple-gamma-ray events registered in the COMPTEL instrument.

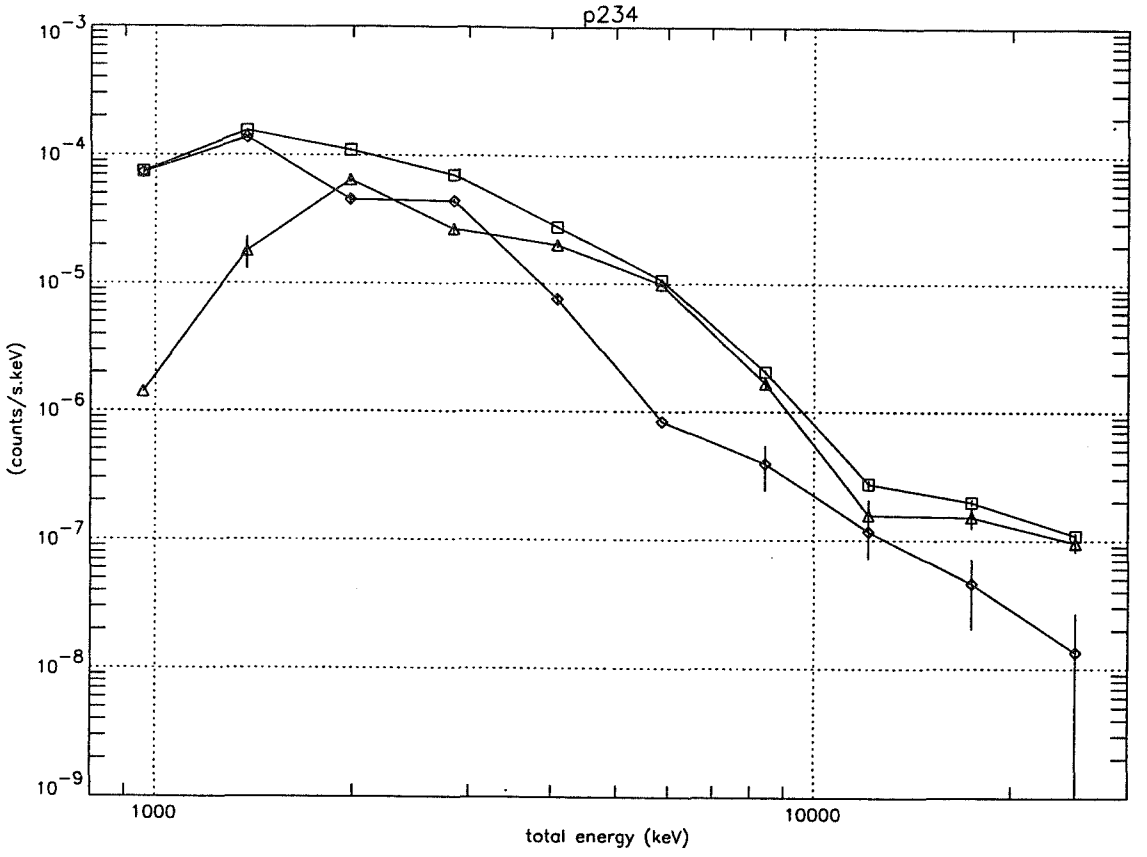

Figure 3. The count rate spectra for the total accepted gamma rays (squares) and prompt background events (triangles). The diamonds represent the difference.

We see that the spectrum of the nuclear cascade gamma rays peaks, as represented by the triangles in Fig. 3, in the few-MeV range and rapidly falls off after ~ 7 MeV, indicative of its nuclear origin. This background is a poorly understood phenomenon and is widely neglected in studies of instrumental background. This background is most pronounced in the data from a Compton telescope because it requires the registration of two separate gamma-ray interactions. However, it is certainly present in all gamma-ray spectrometers. Being most intense in the MeV range it mostly affects an instrument's ability to do nuclear spectroscopy.

Page intentionally left blank

Ceramic Mercuric Iodide Semiconductor Particle Counters

M. Schieber (a,,*) A. Zuck(a), M. Braiman(a) , J. Nissenbaum(a),
R.Turchetta(b), W.Dulinski(b), D. Husson(b) and J. L. Riester(b)

a)The Hebrew University of Jerusalem, Jerusalem 91904 , Israel

b)LEPSI (ULP/IN2P3), Strasbourg, France

*)Also at Sandia National Laboratories,Livermore Ca 94550

Mercuric iodide ceramic radiation detectors, which can act as nuclear particle counters, have been fabricated with single continuos electrical contacts and with linear strip contacts. They have been tested with different kinds of gamma and betha sources as well as in a high energy beam at CERN.
The detectors were also successfully tested for radiation hardness with irradiation of $5*10^{14}$ /cm^2 neutrons for about 200 seconds. This dose corresponds to a few years of functioning at the Large Hadron Collider (LHC). A few days after the irradiation the charge collection efficiency was remeasured and the results are shown in figure 1. At the maximum applied bias, the collected charge after irradiation has decreased to about 3500 electrons, compared to 4500 electrons before irradiation. moreover the curve shows some saturation effect. However, the charge collected is still high enough to be detected with today low-noise VLSI electronics.
Counting efficiency has been measured on different setups with beta (90sr) and gamma sources (photon energies from 44 to 660 keV). For photons the counting efficiency, defined as the ratio between the number of counts and the number of absorbed photons, depends on the energy of the radiation and ,varies from about 20% at 44 keV up to 70% at 660 keV. For beta particles, about 70% of the emitted particles were detected in a 350 micron thick detector.
Charge collection efficiency, to distinguish from counting efficiency, defined as the amount of charge induced on the electrodes as a results of a single photon interaction, has also been calculated. The average collected charge fits well with a linear curve with slope of 35 electrons/((100 micron)(kV/cm)). This data is well described by a dynamic device simulation, where the free carrier mean lifetime is used as a free parameter, adjusted to a value of 1.5 ns, i.e. about 1/100 of the corresponding lifetime τ in single crystal HgI2 detectors and corresponds to a μt value of 10^{-7} cm^2/V as compared to 10^{-4} value for single crystals.

The response to MIP (Minimum Ionizing Particle) has also been studied with a high energy (100 GeV) beam at CERN. One detector was connected to a VA-3 circuit [1].The gold contact strips are 135 micron wide with almost equal spacing for a pitch of 275 microns; the area of the detector is about 2 cm^2. The detector leakage current was about 1 nA/100 V up to about 1000 V. Because of the different pitch on the detector and on the elctronics, 29 contiguous strips on the HgI2 detector were read out.The detector with the readout electronics was put in the center of a silicon detector telescope [2], in a high energy beam (100 GeV muon) at the SPS in CERN. The telescope can reconstruct the track trajectory with a precision better than 1 micron. About 60000 events were collected with the detector biased at 600 V. The one dimensional beam profile as reconstructed by the HgI2 strip detector is shown in Fig.2 and the. Landau distribution is shown in figure 3A 3-dimensional representation of the number of events as a function of pulse-height and interstrip position taken with the same detector is shown in Fig.4. It shows the detector response is uniform, with no charge loss for particles passing in between the strips. These first results of this very novel detector shows great potential for application demanding position sensitive, radiation resistant, room-temperature radiation detectors as it can be found in high energy physics and space applications. Because of its low cost and of its polycristalline material chracter, detectors can be potentially fabricated in any size and shape,i.e. it can also be deposited on flexible thin alumina paper on which any size of electrodes can be predeposited and where the paper with the detector material can assume a cylindrical shape,features which make this material attractive and interesting for large area imaging applications.

References

1) O.Toker et al.,Nucl.Inst.and Methods A340 1994 572

2) C. Colledani, W. Dulinski, R. Turchetta, F. Djama, A. Rudge, P.Weilhammer, Submicron Precision Silicon Telescope For Beam Test Purposes", Nucl. Inst. And Methods A 372 (1996) 379-384.

Prof.Michael Schieber Phone:972-2-6584364
The Fredy and Nadine Herrmann Fax: 972-2-6586412
Graduate School of Applied Science, email: schieber@vms.huji.ac.il
The Hebrew University of Jerusalem,
Jerusalem 91904, Israel.
Dr.Renato TURCHETTA email renato@lepsi.in2p3.fr
Tel:(33)-03-88.10.68.68 Fax 33-3-88-283485
LEPSI (CNRS/University) Strabourg,67030 France

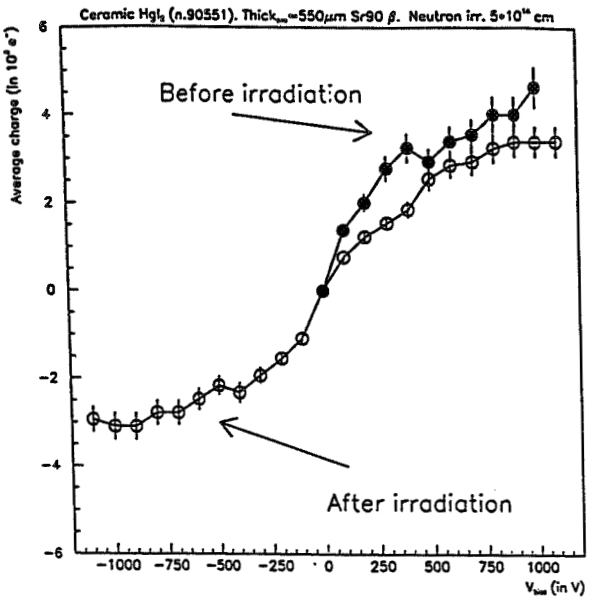
Ceramic HgI2 (n.90551). Thick=550μm Sr90 β. Neutron irr. 5•10^14 cm
Before irradiation
After irradiation
Average charge (in 10^3 e^-)
V_bias (in V)

Fig.1 Average collected charge as a function of bias voltage before (blackdots) and after (white dots) irradiation with $5x10^{14}/cm^2$ neutrons

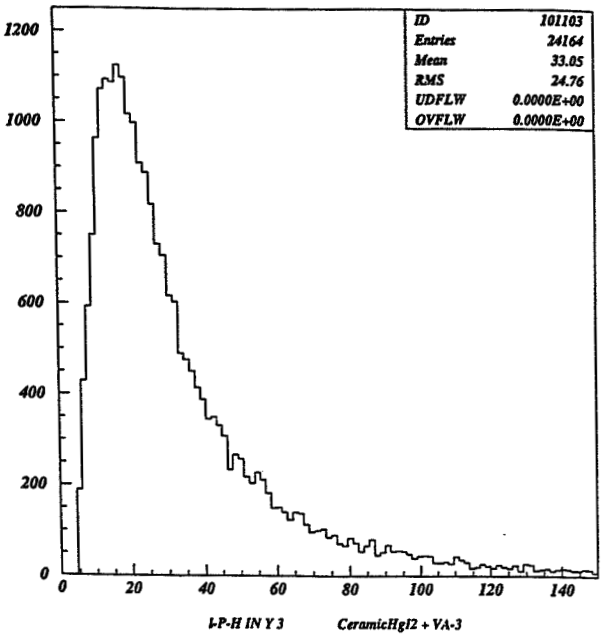

Fig.2 The one dimensional beam profile as reconstructed by the HgI2 strip detector

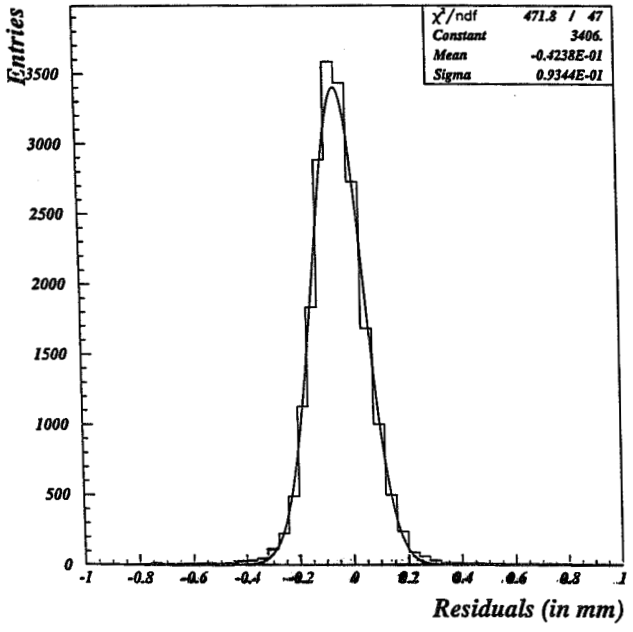

Fig.3 Landau distribution of the beam profile shown in Fig.2

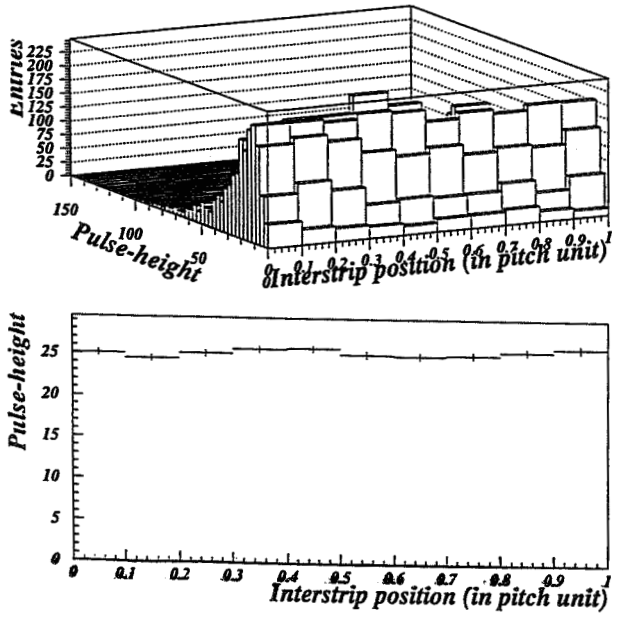

Fig.4 3-dimensional representation of the number of events as a function of pulse-height and interstrip position taker with the same HgI2 detector

Page intentionally left blank

Induced Radioactivity Measured in a Germanium Detector after a Long Duration Balloon Flight

R. Starr[1], L. G. Evans[2], S. R. Floyd[3], J. I. Trombka[3], D. M. Drake[4], W. C. Feldman[4], S. W. Squyres[5], and A. C. Rester[6]

1 Department of Physics, The Catholic University of America, Washington, DC, 20064
2 Computer Sciences Corporation, Science Programs, Lanham-Seabrook, MD 20706
3 NASA Goddard Space Flight Center, Greenbelt, MD, 20771
4 Los Alamos National Laboratory, Los Alamos, NM 87545, USA
5 Cornell University, Ithaca, NY, 14853
6 Constellation Technology Corporation, St. Petersburg, FL 33702

Abstract

A 13-day long duration balloon flight carrying a germanium detector was flown from Williams Field, Antarctica in December 1992. After recovery of the payload the activity induced in the detector was measured.

INTRODUCTION

The Long-Duration Antarctic Mars-Calibration Balloon (LAMB) project was conceived as part of the United States/Russian Joint Balloon Working Group. The intent of this working group was to develop balloon payloads for testing detector systems for future use on planetary space flight missions. LAMB included both gamma-ray and neutron detectors supplied by various US and Russian institutions (Floyd *et al.* 1991). After its launch from Williams Field in the Antarctic (76° South latitude) on 13 December 1992, the LAMB payload circumnavigated the pole at an altitude that varied between approximately 36.6 km and 30.5 km. The flight was terminated on December 26. The most critical components of the payload were recovered and returned to Williams Field on December 28. One of the instruments recovered was the Gamma-Ray Advanced Detector (GRAD) which is a gamma-ray spectrometer designed originally to fly into earth orbit in the cargo bay of the Space Shuttle (Rester *et al.* 1986). Following the Challenger disaster it was reworked into a balloon payload for observations of supernova 1987a (Rester *et al.* 1988).

The GRAD is comprised of a high-purity, n-type germanium crystal with an active bismuth-germanate (BGO) shield. The central element is a 135-cm^3 crystal with a laboratory measured energy resolution of 2.0 keV at 1332 keV. It is enclosed in a BGO shield which is 4.5-cm thick on the sides and 10-cm thick on the bottom. The shield provides a field-of-view with a half angle of 23° at 1 MeV. A 0.3-cm thick plastic scintillator over the aperture provides additional active shielding against charged particles.

The performance of the BGO shield and the background lines detected during the initial flight of the GRAD in 1988 has been reported (Rester *et al.* 1990). During the LAMB mission the GRAD operated only intermittently due to the less than anticipated power available from the solar panels. Insufficient flight data were accumulated for meaningful analysis, however, induced radioactivity was measured over a period of about two days after recovery.

After recovery, high voltage was applied to the GRAD germanium detector and spectra were accumulated from about 0537 UT on 28 December through 0154 UT on 30 December 1992. The BGO was not operated. Counting was terminated in order to prepare the equipment for shipment back to Goddard Space Flight Center. After receipt of the LAMB payload on 30 April 1993 high voltage was again applied to the GRAD germanium detector. The detector system was damaged during shipment and was returned to the manufacturer for repair. No further counting of the GRAD was performed.

LINE IDENTIFICATION

Thirty-nine gamma-ray lines with fluxes exceeding about 0.08 counts per minute were measured in the GRAD central detector as shown in Table 1. The weakest line detected was the naturally occurring background gamma-ray at 2614.6 keV from ^{232}Th which had a flux of 0.083 cpm. The lines in Table 1 are identified and grouped by nuclide. Measured and true energy of the lines are presented as well as the abundance as given in Atomic Data and Nuclear Data Tables (Reus and Westmeier 1983). Also, the actual count rate for each line determined from one ten hour accumulation (see Figure 1) is tabulated as is a normalized count rate which is obtained by correcting for nuclide abundance and detector efficiency. For those gamma rays that originate in the shield the normalized count rate is further corrected by the e-folding length of the gamma ray in the BGO.

Lines at 661.6 keV and 2224.6 keV with count rates of 0.27 and 0.12 cpm, respectively, were not identified. Both of these lines may have been due to contamination from nearby sources. Several sources were brought to the Antarctic for preflight checkout and test of the LAMB payload. These included a ^{137}Cs source which produces the well known 661.6-keV line and a ^{252}Cf source which produces thermal neutrons. Neutrons from the Cf source may have interacted in the GRAD shield and other sources of hydrogen to produce the 2223-keV line from neutron capture on H.

Where more than one gamma-ray line is attributed to the same nuclide the identifications can be checked by comparing normalized count rates. In the case of ^{206}Bi, for example, there are eleven lines with actual count rates that vary by more than an order of magnitude. After normalization the variations are reduced to less than a factor of 1.6. Agreement for other groups of lines is generally as

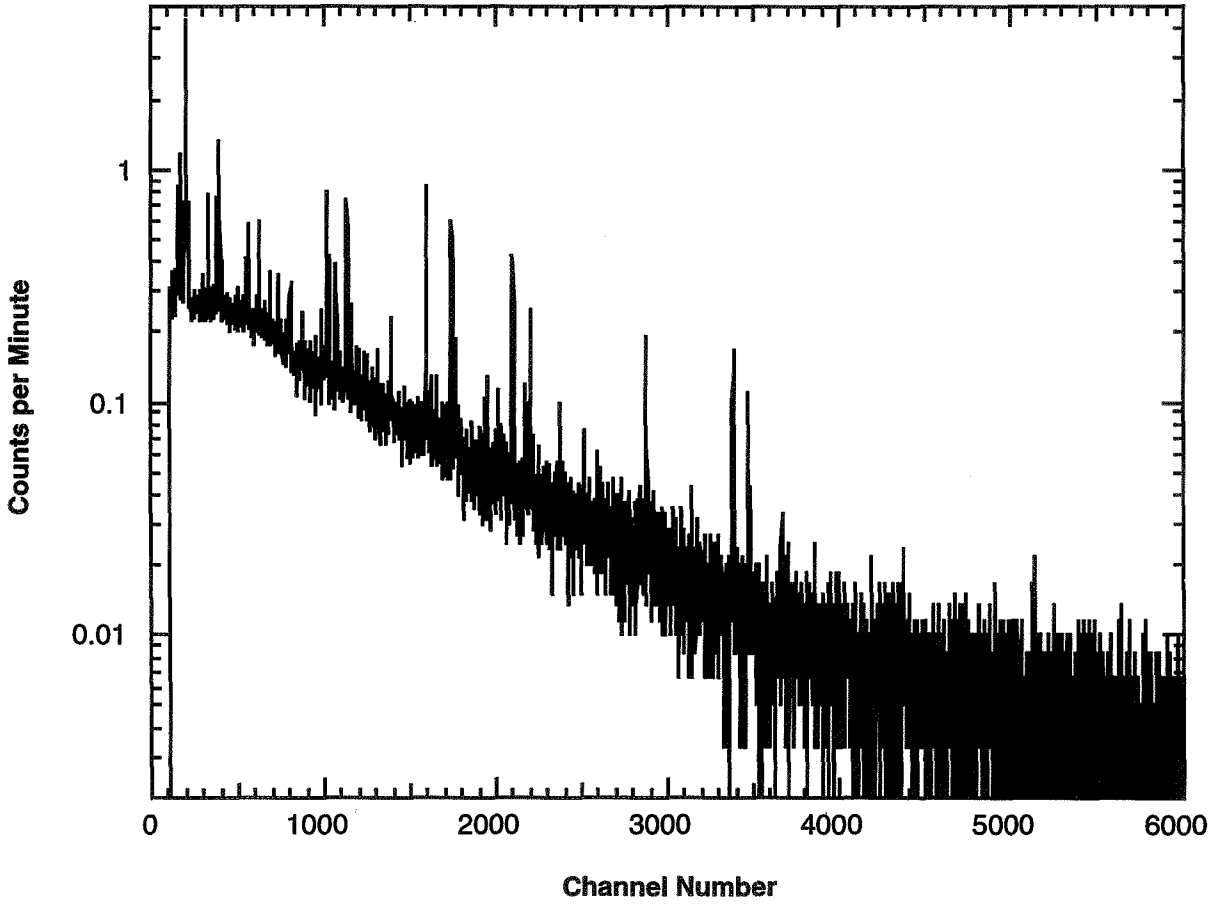

Figure 1. Ten hour accumulation of induced activity and background radiation detected by the GRAD on 28 December 1992. Normalized to counts per minute.

TABLE 1. GAMMA-RAY LINES

CHAN	MEASURED ENERGY (keV)	ELE	NUCLIDE	TRUE ENERGY (keV)	HALF LIFE	ABUN	COUNTS PER MINUTE	NORMALIZED CPM
380	185.8	Ge	71-As	184.8*	2.70 d	83.3	1.458±0.099	0.022±0.002
199	93.4	Cu	67-Cu	93.3	2.58 d	16.1	11.442±0.172	0.851±0.013
162	74.5	Bi	Bi Kα2	74.8		24.7	1.375±0.099	0.887±0.063
167	77.1		Bi Kα1	77.1		41.5	2.203±0.106	0.748±0.036
187	87.3		Bi Kβ1	87.2		14.2	0.991±0.097	0.659±0.065
193	90.3		Bi Kβ2	89.8		4.32	0.312±0.089	0.617±0.176
1394	703.2	Bi	205-Bi	703.5	15.31 d	31.1	0.500±0.057	0.037±0.004
1951	987.4			987.7		16.1	0.312±0.043	0.042±0.006
3473	1764.0			1764.3		32.5	0.422±0.034	0.031±0.002
689	343.4	Bi	206-Bi	343.5	6.24 d	23.4	0.350±0.067	0.051±0.009
989	496.5			497.1		15.3	0.340±0.062	0.051±0.010
1027	515.9			516.2		40.7	1.401±0.099	0.078±0.006
1069	537.3			537.5		30.4	0.932±0.072	0.069±0.005
1589	802.7			803.1		98.9	2.759±0.086	0.062±0.002
1742	880.8			881.0		66.2	2.257±0.081	0.075±0.003
1770	895.0			895.1		15.7	0.470±0.055	0.066±0.008
2012	1018.5			1018.6		7.59	0.235±0.041	0.066±0.012
2167	1097.6			1098.3		13.5	0.306±0.042	0.049±0.007
3142	1595.1			1595.3		5.01	0.143±0.028	0.065±0.013
3384	1718.6			1718.7		31.8	0.654±0.041	0.049±0.003
214	101.1	Ge	67-Ga	100.6†	3.26 d	2.96	11.719±0.891	0.341±0.026
217	102.6			102.6†		37.0	‡	‡
396	193.9			193.9†		20.4	3.097±0.115	0.198±0.007
623	309.8			309.5†		16.6	1.044±0.087	0.110±0.009
806	403.1			402.8†		4.64	0.660±0.080	0.297±0.036
2205	1117.0	Ge	69-Ge	1116.7*	39.05 h	36.0	0.801±0.054	0.107±0.007
2878	1460.4	K	40-K	1460.8	1.28e+9 y	10.7	0.703±0.045	0.389±0.025
563	279.1	Bi	203-Pb	279.0	2.16 d	80.1	0.901±0.087	0.049±0.005
1132	569.5	Bi	207-Pb	569.7	0.805 s	97.9	1.913±0.082	0.043±0.002
2100	1063.4			1063.6		88.5	1.509±0.063	0.036±0.001
547	271.0	Ge	44m-Sc	271.2	2.44 d	77.8	0.506±0.082	0.010±0.002
328	159.2	Ge	47-Sc	159.4	3.34 d	68.0	1.502±0.095	0.026±0.002
737	367.9	Bi	200-Tl	368.0	26.1 h	87.2	0.601±0.079	0.022±0.003
2379	1205.8			1205.7		29.9	0.232±0.037	0.017±0.003
1160	583.8	Th	232-Th	583.1	1.41e+9 y	30.9	0.506±0.063	0.046±0.006
5142	2615.7			2614.6		35.8	0.083±0.017	0.025±0.005
1017	510.8		e^+-e^-	511.0			4.387±0.127	
1313	661.8						0.268±0.057	
4376	2224.6						0.120±0.028	

* EC plus 9.9 keV Kα1 X-Ray.
† EC plus 9.3 keV Kα1 X-Ray.
‡ Summed with 100.6-keV line.

TABLE 2. HALF LIVES

NUCLIDE	GAMMA-RAY ENERGY (keV)	HALF LIFE	MEASURED HALF LIFE
71-As	184.8	2.70 d	2.83±1.1 d
67-Cu	93.3	2.58 d	3.08±0.30 d
206-Bi	803.1	6.24 d	5.57±1.6 d
67-Ga	102.6*	3.26 d	2.63±0.90 d
69-Ge	1116.7†	39.05 h	40.3±10.6 h
200-Tl	368.0	26.1 h	34.5±14.2 h
47-Sc	159.4	3.34 d	4.74±2.8

* EC plus 9.3 keV Kα1 X-Ray.

† EC plus 9.9 keV Kα1 X-Ray.

good or better except in the case of ^{67}Ga where normalized count rates vary by a factor of 3.1. No good candidate nuclides could be identified that might add to the line fluxes at 100.6 and 402.8 keV, so these deviations remain unexplained for this measurement.

A further check on the identification of induced activity gamma rays is by determination of the half life of the lines. For the strongest gamma ray from each nuclide, where there are sufficient statistics to make a meaningful calculation, the half life is determined. Because measurements did not begin until two days after recovery and only lasted about two days, half lives shorter than 1 day or longer than about six days could not be determined. The results are presented in Table 2. In each case there is good agreement between the measured values and those taken from the Atomic Data and Nuclear Data Tables (Reus and Westmeier 1983).

ACKNOWLEDGMENTS

The authors would like to thank the personnel at the University of Michigan Space Physics Research Laboratory for their support during design, assembly, test and flight of the LAMB payload. In particular, we are grateful to Stephen Musko and David Boprie for their efforts in the Antarctic. We would also like to express our gratitude to Danny R. J. Ball, Steven Peterzen, Victor Davison, David Gregory, Kevin Tillery and the rest of the National Scientific Balloon Facility team that provided launch services at Williams Field. Finally, we gratefully express our thanks to the National Science Foundation and the United States Navy for the superb support they provided while we were in the Antarctic.

REFERENCES

S. R. Floyd, J. I. Trombka, L. G. Evans, R. Starr, S. W. Squyres, Yu. A. Surkov, L. P. Moskaleva, O. Scheglov, A. G. Mitugov, A. C. Rester, G. J. Bamford, R. L. Coldwell, W. C. Feldman, D. M. Drake, W. E. Sharp, and J. E. Dombrowski, 1991, *Joint US-USSR Long Duration Antartic Mars Calibration Balloon (LAMB) Mission*, AIAA International Balloon Technology Conference, **AIAA-91-3655-CP**, Albuquerque, N Mexico, October 8-10.

A. C. Rester, R. B. Piercy, G. Eichhorn, R. L. Coldwell, J. McKisson, D. W. Ely, H. M. Mann, and D. A. Jenkins, 1986, IEEE Tans. Nucl. Sci **33**, 732-34.

A. C. Rester, R. L. Coldwell, F. E. Dunnam, G. Eichhorn, J. I. Trombka, R. Starr, and G. P. Lasche, 1988, Ap. J. **342**, L71-3.

A. C. Rester, R. L. Coldwell, J. I. Trombka, R. Starr, G. Eichhorn, and G. P. Lasche, 1990, IEEE Tans. Nucl. Sci **37**, 559-65.

U. Reus and W. Westmeier, 1983, Atomic Data and Nuclear Data Tables, Volume **29**, Numbers 1 and 2.

ANALYSIS OF ACTIVATION EFFECTS IN SPACE-BORNE AND PROTON BEAM IRRADIATED γ-RAY DETECTORS

P R Truscott, C S Dyer, H E Evans, M Cosby
Space Department, Defence Evaluation and Research Agency, Farnborough, Hamphire GU14 0LX, United Kingdom

C E Moss
Los Alamos National Laboratory, Los Alamos, NM 87545

ABSTRACT
Results are presented from Space Shuttle and proton-beam (0.3 and 1 GeV) experiments in which BaF_2, GSO and LSO γ-ray detector materials were irradiated. These are compared with predicted effects of activation and detector response.

Author details

Name	Address	Tel	Fax
Pete Truscott	Space Department, A8 Bldg, Defence Evaluation and Research Agency, Farnborough, Hampshire, GU14 0LX, United Kingdom	+44 1252 393290	+44 1252 396330
Clive S Dyer	Space Department, A8 Bldg, Defence Evaluation and Research Agency, Farnborough, Hampshire, GU14 0LX, United Kingdom	+44 1252 393774	+44 1252 396330
Howard E Evans	Space Department, A8 Bldg, Defence Evaluation and Research Agency, Farnborough, Hampshire, GU14 0LX, United Kingdom	+44 1252 392652	+44 1252 396330
Matthew Cosby	Space Department, A8 Bldg, Defence Evaluation and Research Agency, Farnborough, Hampshire, GU14 0LX, United Kingdom	+44 1252 396313	+44 1252 396330
Cal E Moss	Los Alamos National Laboratory, Los Alamos, NM 87545, USA	+1 505 667 5066	+1 505 665 4414

SUMMARY

Justification

Spacecraft in Earth orbit are exposed to a radiation environment comprising high-energy cosmic-ray nuclei, solar-flare protons, and particles (predominantly protons and electrons) trapped in the Van Allen radiation belts. Whilst the prompt effects of these sources on γ-ray instruments can usually be vetoed with shield detectors, spallation and nuclear capture interactions can give rise to radioactivity in detector materials themselves, resulting in enhanced background levels as nuclei decay without a veto. The problem is made more complex as a result of:

- The variation of the cosmic-ray/solar-flare/trapped proton source as a function of orbital position and time;
- The important contribution of secondary nucleon production in the spacecraft;
- The potential range of nuclide species produced by spallation, and hence the range of half-lives and decay modes that are involved in the radioactive decay process.

In order to achieve overall background reduction of an instrument, consideration should be given to induced activation properties of potential detector materials. Here the variety of materials available may help optimise the design in terms of spectral range, resolution, and efficiency as well as background. However, for many attractive detector materials our experience of activation effects from space-flight is limited to non-existent.

Description of Study and Results

The Cosmic Radiation Effects and Activation Monitor (CREAM) experiment is a Space Shuttle middeck payload used to collect information on the single-event upset environment, and mission accumulated neutron flux and total dose experienced in the Shuttle crew cabin area. In addition, this experiment has permitted space-flight of a variety of detector materials, including sodium iodide, barium fluoride, GSO, LSO and CdZnTe. A similar radiation experiment, the Shuttle Activation Monitor, has provided data on NaI and BGO activation effects. Post-flight activation analysis has been performed by measuring:

- The pulse-height spectrum through a photomultiplier tube mounted to the scintillators;
- Any escaping γ-rays emanating from the materials using a germanium detector in close proximity to the scintillator or semiconductor.

Results from beam irradiations (using 300 MeV and 1 GeV proton sources) provide an additional and important source of experimental data obtained under better controlled and more intense irradiation conditions. Figures 1 and 2 show internal energy-loss spectra from GSO (at 19 minutes to 21 hours after irradiation) and barium fluoride (at 6, 8 and 10 hours), and indicate a more rapid fall-off in activation for the GSO (see Figures 3 and 4). The spectra show the energy-loss processes going on in the crystals as a result of radionuclide decay - the peaks are from isomeric transitions and electron-capture events, while the continua principally arise from β-decays. In the barium fluoride almost all of the activation comes from radioisotopes of barium, caesium and iodine (i.e. from barium spallation).

The analysis process also involves comparison of the spectra with ab initio predictions from Monte Carlo computer programs. These simulate in great detail the processes of detector activation, multiple-generation radionuclide decay and detector response. The DRA's Integrated Radiation Transport Suite (IRTS) has been applied to simulate the detailed physics of many of these processes. The suite comprises three Monte Carlo radiation transport codes to model particle nuclear and electromagnetic interactions in three-dimensional geometries (see Table 1 and Figure 5). These are supported by a series of pre-processor (e.g. cross-section data set up) and analysis codes.

Table 1

Suite	Radiation Transport Code	Particle types	Energy range of transport
IRTS	**LHI/HETC**	**protons, neutrons, pions, muons, light-nuclei such as deuterons, tritons, helium and lithium**	**>15 MeV (neutrons <15 MeV transported by MORSE, spallation product de-excitation γ's transported by EGS)**
IRTS	**MORSE**	**neutrons (inelastic scatter γ's transported by EGS)**	**thermal - 15 MeV**
IRTS	**EGS**	**photons, electrons and positrons**	**photons >1 keV electrons/positrons >10 keV**
	BANKER	**photons in cylindrical geometries**	**>1 keV**

Depending on the detector material, the total predicted response takes into consideration the decays of between 100 to over 300 nuclide species. The modelling process allows for shielding effects of the spacecraft structure, and most importantly for cosmic-rays, the generation of secondary neutrons which then interact with the crystals. Results show very good agreement between these simulations and measurements and serve to quantify the relative contributions of the different sources of primary and secondary radiation to detector activation (see Figure 6).

Principal Conclusions

The CREAM experiment has provided an excellent opportunity to gather data on activation effects in a variety of more novel γ-detector materials as a result of space-flight, and has given the first results from the space-flight of BaF_2 and GSO. Together with ground irradiation experiments, CREAM is permitting validation of simulation codes and techniques, which may then be applied to the materials selection process so that the background in future instruments are optimised.

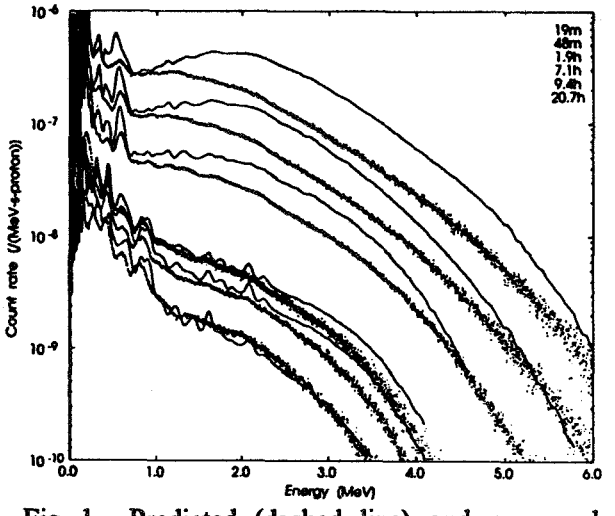

Fig 1 Predicted (dashed line) and measured internal spectra from 5cm x 5cm GSO detector irradiated by 1 GeV protons.

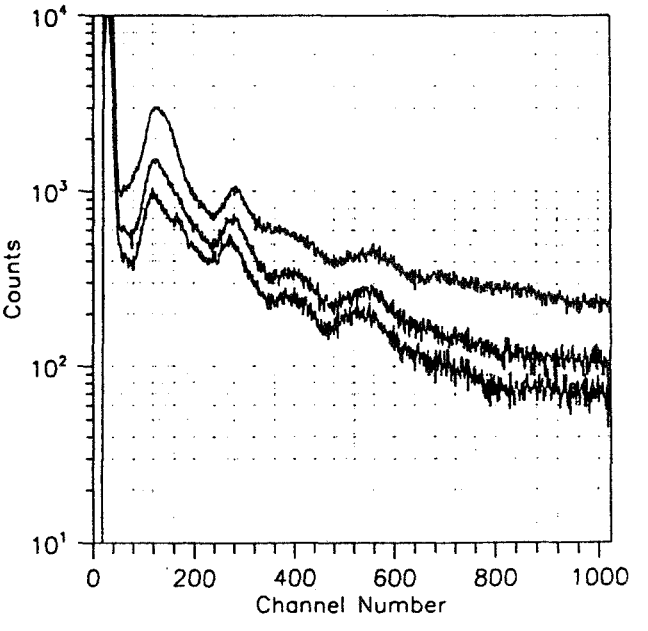

Fig 2 Internal spectra from 1GeV proton beam irradiation of BaF_2 (at 6.2, 8.2, and 10.2 hours).

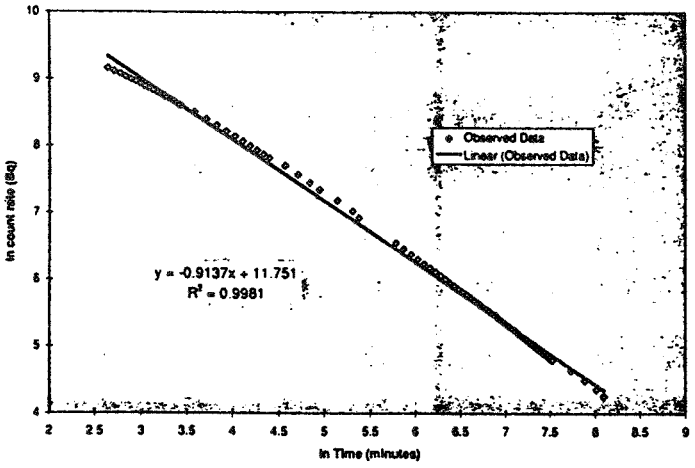

Fig 3 Decay rate in 5cm x 5cm GSO crystal as a function of time after irradiation.

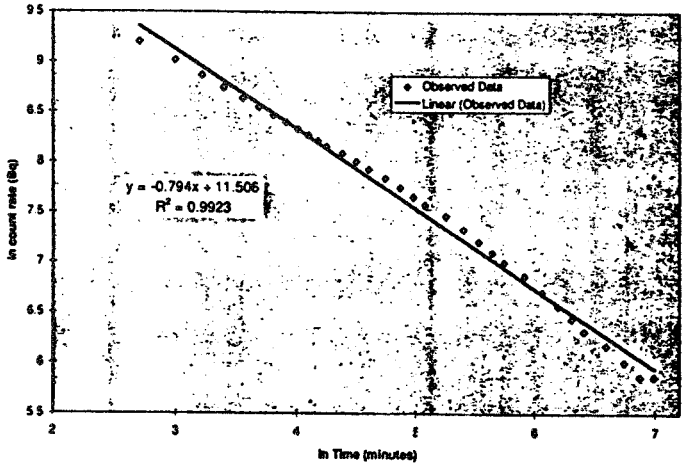

Fig 4 Decay rate in 2.5cm x 2.5cm BaF_2 crystal as a function of time after irradiation

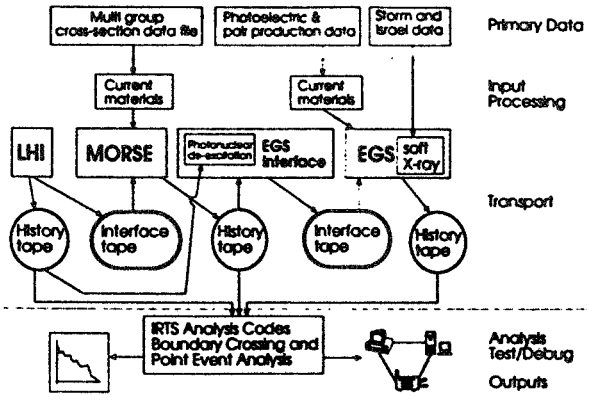

Fig 5 The Integrated Radiation Transport Suite (IRTS).

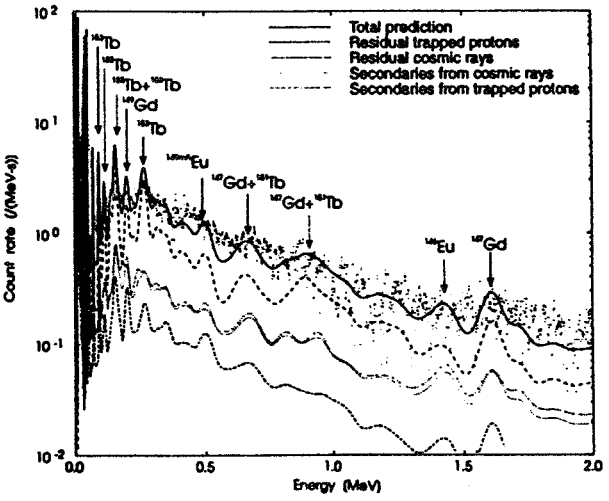

Fig 6 Measured internal spectra from CREAM 5cm x 5cm GSO detector 17 hours after touchdown, compared with predictions identifying contribution from different radiation sources

Outer Zone Energetic Electron Environment Update

A. L. Vampola
Space Environmental Effects, Vista, CA

Introduction

This paper discusses a European Space Agency-funded study which included two major phases: first, a data processing phase in which 16 months of in-situ CRRES energetic electron data were analyzed to provide better estimates of the energetic electron environment in the outer zone of the Earth's magnetosphere and to provide processed data bases for further investigations; and second, a phase in which results from the first phase were used to train neural networks to predict energetic electron flux levels using historic magnetic indices as the input variable.

Phase 1 -- CRRES MEA Data Analysis

CRRES (Combined Release and Radiation Effects Satellite) was launched on 25 July 1990 into a highly elliptical orbit (350 x 33584 km, 18.1° inclination) and provided almost continuous data until loss of communications occurred on 11 October 1991 (Johnson and Kierein, 1992). The CRRES satellite was redundantly instrumented with ionizing particle detectors with the express intention of using the resulting data to update both the AE8 and AP8 models. Included in the instrument complement was the modified and refurbished backup instrument for the OV1-19 magnetic focusing electron spectrometer which supplied low altitude data for the AE8 model. For the CRRES mission, the energy range was changed to 100 keV to 1.7 MeV, since this range is of primary interest to engineering applications and the RADSAT portion of CRRES was directed toward engineering. This instrument was identified as Medium Electrons A (MEA) (Vampola et al, 1992).

In this project, the entire MEA data base was processed a number of times to produce a reduced data set in which background corrections were made and local measurements were transformed to equatorial equivalents, using the locally-determined pitch-angle distributions. This equatorial-equivalent data base was then used to determine average conditions, maximal conditions, and the frequency of observation of specific flux levels as a function of energy and L.

Daily averages of equatorial flux were merged with the magnetic indices Kp, Dst, and Ap. The merged data set was then used in the second phase, which involved training neural networks to predict flux levels using magnetic indices as input.

All of the goals of the first phase were achieved: a mission-averaged outer zone environment from MEA in-situ data which could be compared with AE8 was generated; flux probability distributions were obtained; flux maxima were derived; processed data bases for use in other investigations by other investigators were produced; and, an input data base for training and testing neural networks was produced.

The primary output products from the first phase were:

a) Mission-averaged energetic electron spectra at 21 L values in the outer zone.
b) Mission-averaged energetic electron pitch-angle distributions at 21 L values in the outer zone.
c) Mission-maximum fluxes as a function of L and energy.
d) Two software modules:
   1) MEAPROB.FOR. This program accepts L and Energy as input and returns the equatorial Jperp log(flux) at 90%, 50%, 10%, 1%, and 0.1% probability of occurrence. Since it is based on statistics derived from the CRRES mission, the fluxes it predicts are probably excessive for solar minimum conditions.
   2) MEAMAX.FOR. This program accepts L and energy as input and returns the maximum differential and integral (to 7 MeV) fluxes which might be experienced in orbit. The energy extrapolation uses OV1-19 spectral fits. Since the CRRES mission included high magnetic activity periods, these maxima are probably valid for engineering design specifications.
e) Four major MEA data bases:
   1) TASK1B.BIN. This ~200 MByte binary data base contains ephemeris and raw MEA data averaged in 5° pitch-angle bins, with one record provided for and averaged over each passage through each 1 hr local time-0.25 L bin.
   2) TASK1C.BIN. Similar to TASK1B.BIN, but includes only background-corrected Jperp counts normalized to equatorial values and includes a pitch-angle distribution coefficient. An ASCII version of TASK1C.BIN, TASK1C.DAT, was also generated.
   3) Data Base A, This ASCII file contains ephemeris parameters, flux spectral fits, pitch-angle distribution coefficients, and magnetic index parameters for each passage through a 1 hr LT - 0.25 L bin.
   4) Data Base B. This binary file, contains the same data as TASK1B.BIN, plus pitch-angle distribution fits, energy spectral fits, and magnetic indices.

The software and data bases are available to those who wish to use them for research and/or design purposes.

Phase 2 -- Neural Network Training and Analysis

Phase 2 was also successful, though not completely. A commercial neural network software package, Brainmaker for Windows, was selected and trained using the MEA data and Kp. The predicted fluxes from the trained networks for five energies at six L values (30 cases), when averaged over the CRRES MEA mission, agree with the actual observed fluxes within 15% (worst network). On average, individual predictions for a specific L, energy, and date agree with the MEA observation within 0.2 in log(flux). As a result, an accurate *average* model of outer zone electron fluxes *over the energy interval of the CRRES MEA data set* has been generated using 65 years of estimated daily flux. A new model, ESA-SEE1, was generated. An accurate representation of the solar cycle variation was also obtained via a superposed analysis of six solar cycles of data. But, the failure of the neural networks to properly predict extrema (both minima

and maxima) prevented the generation of probability models or maximal models from the historical magnetic indices.

This phase of the study produced additional products of use to engineering-design of satellites and satellite subsystem. They included:

a) Thirty trained neural networks (5 energies at each of 6 L-values) which use daily-sum Kp as input and provide estimates of daily-average log(flux).
b) An outer-zone energetic electron average flux model, based on over 64 years of daily average fluxes, to supplant AE8. This model is defined in terms of fluxes at ENVIRONMENT MINIMUM (which occurs six months after the solar sunspot minimum) and a quadratic fit to the solar-cycle variation.
c) A functional dependence of energetic electron flux on epoch within a solar cycle.
d) A neural-network produced energetic electron data base, TASK3B.DAT, which contains the daily average log(flux) for 5 energies at 6 outer zone L values for each day from 10 January 1932 through 31 July 1996.
e) Four software modules:
    1) SEE.FOR. This program accepts daily-sum Kp as input and produces an estimate of the daily average energetic electron fluxes at 5 energies between 148 keV and 1.58 MeV at 6 L-values from 3 to 7.
    2) ESA-SEE1.DAT. This is a flux map that is a modified version of AE8MIN and can be used by any software package that uses the NSSDC-supplied AE8MIN map. It is a "drop-in" replacement.
    3) An updated version of RADMODLS (Vampola, 1996) which accesses the new ESA-SEE1 map. RADMODLS accesses all of the NSSDC particle maps and does orbital integrations and dose calculations. This updated version provides additional flexibility over previous versions in that any of the DGRF field models can be used (recommended only for research purposes).
    4) MEAINTEG.FOR. This program accepts L and energy as input and prints out the average differential and integral (to 7 MeV), unidirectional and omnidirectional, equatorial log(flux). The energy extrapolation uses OV1-19 spectral fits.

This data base and the software are also available to those who wish to use them for research and/or design purposes.

Discussion

The cumulative log(flux) probability distributions produced from the MEA data set are a much-needed tool for spacecraft design. They permit the engineer to make reliability/cost trade-offs based on a knowledge of the variability of the environment which will be encountered in space. Such trade-offs apply to both dose degradation and the permissible level of background effects. The short time span of the MEA data (compared to a solar cycle), the limited energy level of the MEA (40 keV to 5 MeV would have been much more desirable), and the fact that CRRES flew during a more-active than normal period all argue against this study being a definitive one. But, the utility of the product should lead to similar analyses in the future which will have a more adequate data base.

The maximum-flux tables permit similar trade-off studies of radiation protection design for thick dielectric charging. Since in this case we are looking for a maximum, the limitations noted above pertaining to the mission duration and the level of magnetic activity do not apply. In fact, the high magnetic activity almost ensures that the maxima observed by the MEA are valid maxima, for all practical purposes. The limited energy range is a separate question. Extrapolating spectra measured by the MEA provides only an educated guess as to the true maxima.

Recommendations:

While the present results are a significant improvement over AE8, the results of this study cannot be considered ***the*** definitive result for an outer zone environment. The following areas need further improvement:

1) Extension of the energy spectrum below and above the energy range of the MEA instrument response (90 keV to 1.7 MeV). For the present study, published energy spectra (Vampola et al, 1977) from the OV1-19 instrument (50 keV to 5.1 MeV, circa 1969) were used to extrapolate the energy spectra down to 40 keV and up to 7 MeV. However, the published spectra were segmented linear fits in log(flux) *vs.* log(energy) which overestimate the flux above about 4 MeV and perhaps below 100 keV. The OV1-19 data should be reanalyzed and fitted with cubic (rather than linear) functions to the log(flux) *vs.* log(energy) spectra so that more reliable fits are available for extrapolating the OV1-19 spectra above 4 MeV and below 100 keV.
2) Different neural network software which does a better job of predicting extrema should be identified, procured, and trained with the MEA data in order to produce a probability distribution model based on a longer data base than the CRRES MEA data base.

Acknowledgments

Selection and training of the neural network software was done by Dr. H. C. Koons, Harbor City, CA. The project was funded by the European Space Agency through the Mathematics and Software Division, ESTEC. Dr. Eamonn Daly was the cognizant officer.

References

Johnson, M. H., and J. Kierein, "The Combined Release and Radiation Effects Satellite (CRRES): spacecraft and mission," *J. Spacecr. Rockets, 29*, pp. 556-563, 1992.

Vampola, A. L., J. B. Blake and G. A. Paulikas, "A New Study of the Magnetospheric Electron Environment," *J. Spacecraft and Rockets, 14*, 690-695, 1977.

Vampola, A. L., J. V. Osborne, and B. M. Johnson, "The CRRES magnetic electron spectrometer AFGL 701-5A (MEA)," *J. Spacecr. Rockets, 29*, pp. 592-594, 1992.

Vampola, A. L., "Radiation Belt Models for the PC: RADMODLS," *Radiation Belts Models & Standards,* Geophysical Monograph 97, American Geophysical Union, Washington, D. C., J. F. Lemaire, D. Heynderickx and D. N. Baker, (eds), 1996, pp. 315-319.

Using Cross-Correlations of SEUs and AP8 as a Diagnostic Tool

A. L. Vampola[#]
University Research Foundation, Greenbelt, MD 20770
and
M. Lauriente[*]
NASA Goddard Space Flight Center, Greenbelt, MD 20771

Introduction

Timely data on low altitude energetic protons is very important for predicting the effect on humans and satellites. Because of the high bioeffectivity of protons in tissue, determination of the geographical location of the south Atlantic anomally (SAA) would be especially useful for reducing the risk associated with extra-vehicular activities. Because the AP8 model was developed with an epoch several decades old, the location of the south Atlantic anomally is incorrectly positioned in the model. The lack of extensive present-epoch energetic proton data at low altitude has prevented the update of the AP8 proton model. While there are studies in progress which are attempting to update the model at low altitude by using the path-integrated column density of the residual atmosphere as an organizing parameter, success in those studies will be defined by consistency in organization of old data. New data will still be required to provide a good present-epoch model.

As an alternative to using instrumental measurments of proton fluxes, background effects, proxy data sets such as SEUs, anomalies in instruments, enhanced background in shielded sensors believed to be induced by high energy protons, and dosimeter data in which key parameters (energy, efficiency, geometric factor, shielding, etc.) are poorly known can also be used. This in situ data is not as precise as direct measurement of the proton flux as geometric factor and shielding etc. are not calibrated, but these factors do not affect determination of the location of the SAA.

The SAA in the Geomagnetic Field

The geomagnetic field has a complex geometry which is customarily described (mathematically) as a spherical harmonic series. The low order terms in the expansion have the largest coefficients, with the dipole term providing the largest contribution. The overall configuration is usually considered as an offset (from the center of the earth) tilted dipole with higher order terms. Since the principal axis of the field is offset and tilted with respect to the Earth's axis, the surface field intensity varies in a non-symmetric manner. In the region of Brazil and the south Atlantic, the surface field intensity is significantly lower than elsewhere. The ground-level intensity minimum is located at -27.4° latitude, -54.1° longitude.

The field intensity minimum does not maintain the same configuration as the altitude increases. The higher order terms in the expansion, which fall off faster than the lowest order terms, are still effective in determining the overall intensity of the field. Figure 1 shows contours of constant field intensity at 1336 km. At this altitude, the intensity minimum is at -18.7° latitude, -50.1° longitude (4° eastward and 8.7° northward of the 0 km location).

This variation of field geometry with altitude has a corollary effect on the configuration of the energetic proton flux distribution at low altitude.

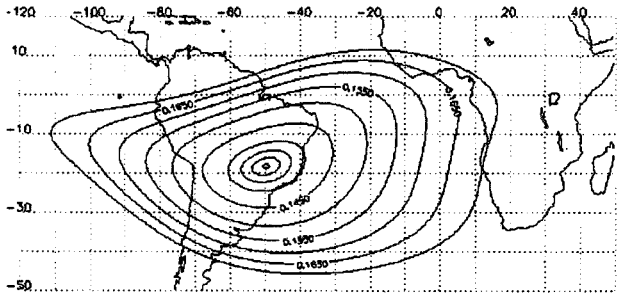

Figure 1. IGRF90, Epoch 1993.0, 1336 km magnetic field intensity contours. At this altitude, the contours are quite different from the ground level contours and the minimum is north and east relative to the 0 km intensity minimum.

[#]Consultant
[*]Manager, EnviroNET

The intensity minimum at low altitude is of interest because a particle which is trapped in the Earth's magnetic field and is performing bounce motion mirrors at a constant magnetic field intensity along its drift path. The particle's lowest mirror altitude coincides with the location at which the geomagnetic field intensity is a minimum at a given altitude. But, the maximum in the energetic proton flux at low altitude due to the SAA does not coincide in location to the exact region of the minimum in the magnetic field, since the particle maximum is a convolution of the magnetic SAA and the Energy-L-B/B0 dependence of the particle ensemble.

The SAA in Energetic Proton Fluxes

For this study, proton fluxes were determined using the AP8MAX model and the IGRF90-Epoch 1993.0 magnetic field model. The AP8 model was constructed with a modified version of IGRF65. Note that use of the AP8 model with a modern epoch magnetic field will produce erroneous flux intensities as a function of altitude,[1] but will provide accurate geographic results.[2]

Figure 2 shows proton flux intensities at 1000 km obtained from AP8. The particle contours do not correspond in detail to the magnetic field contours in Fig. 1. Other energies will produce slightly different contours (and centroid locations) for two reasons. First, higher energy protons peak at lower L in the inner zone. This translates to a lower magnetic latitude (closer to the geographic equator in the vicinity of the SAA). The second effect is due to differences in flux intensity gradients as a function of altitude (or atmospheric density) and energy. This effect translates into a westward trend with increasing energy for the location of the centroid of the proton flux intensity.

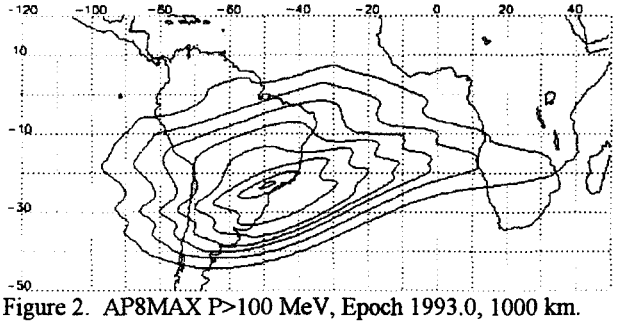

Figure 2. AP8MAX P>100 MeV, Epoch 1993.0, 1000 km.

At 500 km, a contour plot of >50 MeV protons would be virtually indistinguishable from Fig. 2 because the AP8 model has few or no protons with 50 MeV< E <100 MeV at this altitude in this region. As the altitude increases, the entire pattern moves northward and *westward*.

The above discussions show that the spatial geometry of energetic proton flux intensities is complex and is a function of energy and altitude. If the AP8 model provides a reasonably accurate longitude-latitude map of the fluxes, correlations between the model and proton-induced effects on spacecraft can be used to address a number of topics, including the accuracy of AP8 and the energy of the particle producing the effects.

Analysis Approach

All spacecraft in low orbit are affected by the energetic protons in the SAA region. In some cases, mission operations are not even possible while in this region. In other cases, the effects are entirely negligible. This is especially true if the orbit is a low-inclination orbit. The particle SAA at 500 km is centered at about -35° S latitude and lower inclination orbits, such as most Space Shuttle missions, miss the heart of the SAA. For most spacecraft, passage through the SAA produces only minor effects which constitute an annoyance.

Over a period of time, a log of proton-induced effects can effectively map the SAA. Figure 3 is a mapping of single event effects (SEEs) on TOPEX. The TOPEX/Poseidon satellite was launched August 10, 1992 into a circular Earth orbit at an inclination of 66° and an altitude of 1336 km. In this orbit, the satellite traverses the SAA region approximately six times per day. A total of 2172 Earth sensor anomalies experienced by TOPEX between launch and mid-1994 are plotted in Fig. 3.Two Earth sensor assemblies are located in a module on the Earth-facing side of the TOPEX spacecraft. Two types of anomalies are seen in these assemblies. One is a spike in the pitch and roll error telemetry, denoted PR. The other is a switch to the Wide Angle mode, denoted WA. Both of these errors occur in each of the sensors.[3] Figure 3 is a

longitude-latitude plot of the location of the TOPEX SEEs. This is a sparse data set: on average, only one out of twenty-two 0.5° x 0.5° latitude-longitude bins in the anomaly region will have a SEE.

A 2-D (longitude and latitude) cross-correlation between the background data set and the current-epoch AP8 predicted fluxes is used. The correlation must be done as a function of proton energy and satellite altitude. The technique can be used to

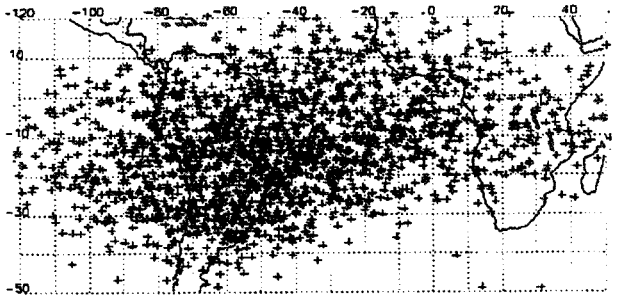

Figure 3. TOPEX SEE geographical distribution.

determine the energy of the particle that is producing a particular effect, as will be seen. In correlating two areal arrays, a base array is constructed to extend beyond the other array in all directions so that one of the arrays can be shifted relative to the other and maintain a complete overlap between the cells of the base array and the smaller shifted array. Shifting is done along both axes independently. A 2-D variational array is constructed in which each element of the array is the sum of the products of corresponding cells in the base array and the shifted array. The variational array is then normalized and contours of constant correlation strength are plotted.

The sparse SEE data set was correlated with a normalized AP8MAX Epoch 1993.5 flux map using the above procedure. AP8MAX fluxes were determined for each 0.5° x 0.5° bin from -130° to +60° longitude and-60° to +30° latitude. The AP8MAX and SEE longitude-latitude maps were cross-correlated with offsets from -10° to +10° in both longitude and latitude at 0.5° increments. The resulting variational array was then normalized and contours of constant correlation strength plotted. The centroid of the TOPEX SEEs coincides with the AP8MAX maximum of >80 MeV protons within the accuracy of the procedure, ~0.2°.

If other threshold energies are used, a slightly different correlation pattern is obtained for the two reasons mentioned previously. The center of the SAA flux intensity pattern at 1336 km altitude moves northward toward the geographic equator and westward as energy increases.

Since the location of the proton SAA has an energy-latitude dependence, we made use of this property to estimate the energy of the particles that are causing the TOPEX SEEs. Figure 4 shows the latitudinal and longitudinal offsets between the SEEs and AP8MAX Epoch 1993.5 as a function of energy. This figure indicates that the threshold energy for producing these SEEs is about 80 MeV.

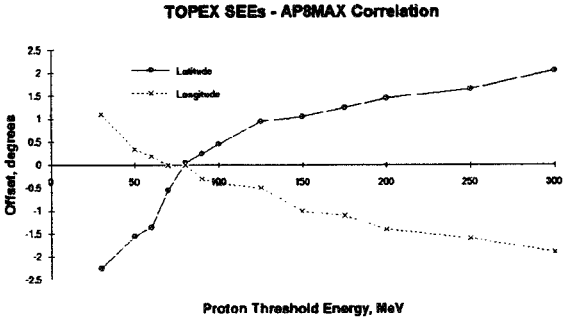

Figure 4. TOPEX SEEs-AP8MAX cross-correlation latitude-longitude offsets vs. threshold energy.

Figure 4 included all TOPEX SEEs. Separating the SEEs into subgroups, represented by "1", "2", "WA", and "PR", each of which included either all of the SEEs from assembly 1 or 2, or all of the WA or PR SEEs from both assemblies, produced correlation results that were indistinguishable from the entire set except for the "PR" subset. SEEs in the PR subset (which included only 337 SEEs) were apparently produced by a different particle population than the rest of the set. An analysis similar to that in Fig. 4 indicated that the threshold for production of those anomalies was around 175 MeV.

We also applied this procedure to an entirely different type of data set, "glitches" from the COBE/DIRBE sensor. COBE (COsmic Background Explorer) is in a high inclination 890 km circular orbit. The DIRBE sensor consists of a set of infrared detectors at several wavelengths. During passage through the SAA and the low altitude extensions of the outer zone electron belts, a shutter of several gm/cm^2 is used to protect the detectors. Excess signal in a detector for a single count cycle is considered to be due to particle penetration. The data are stored in 128-second segments, so there is an uncertainty in the location of a "glitch" of about +/-3° along the orbit path. This uncertainty "smears" the data set for

correlation purposes, but one of the advantages of the 2-D correlation is that it locates the centroid of the correlation strength. A large data set will provide accurate results if there are sufficient samples that the uncertainties average out. Figure 5 is a contour plot of the DIRBE "glitch" set. When we apply the correlation procedure to this data set, we get ambiguous results. The correlation procedure produces normal results up to about 100 MeV, at which point a strong single correlation peak is still seen, but a broad plateau begins to appear o the north. By 135 MeV, there are two equal correlation peaks, the original one at lower latitude and a new one closer to the equator. Finally, by 175 MeV, the major correlation is with the northern peak with only a shoulder being seen to the south.

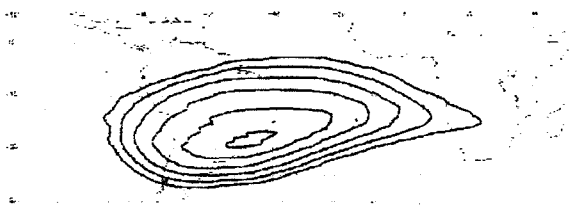

Figure 5. Contours of background effects in COBE/DIRBE IR sensor.

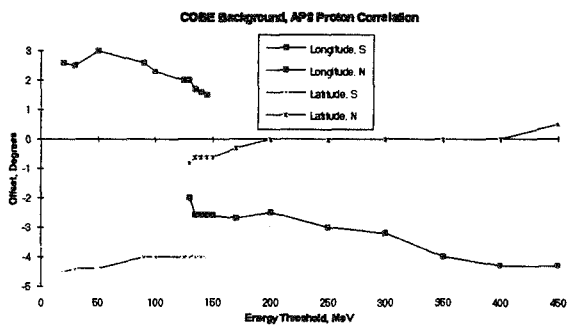

Figure 6. COBE-AP8MAX cross-correlation latitude-longitude offsets vs. threshold energy.

Figure 6 shows the result. This appears to be a breakdown in the cross-correlation technique. Actually, it illuminates a problem with AP8. At the COBE altitude in the energy range 120 MeV<E<150 MeV, the AP8 model itself contains two flux intensity peaks. The two correlation peaks occur because one data set, COBE, has a single peak and the other, AP8, has two.

At 890 km and 135 MeV, the AP8 model has two peaks of equal intensity. Below this energy, one peak is dominant, above it the other dominates. This dual-peak characteristic is not seen at lower or higher altitudes. it's clearly an artifact in the model, since the COBE correlation follows the peaks. If there actually were a dual peak structure in the fluxes, the correlation would have a single peak. The COBE data would show a dual intensity structure corresponding to the particle structure, and the correlation would be maximum when the two sets of peaks matched. While not as clear cut as Fig. 4, Fig. 6 does indicate that the background in the DIRBE detectors is due to protons with energies above about 200 MeV. The shutter is being penetrated.

Discussion

This cross-correlation technique is very simple to apply and yet is very powerful, in that the use of large data bases produce good results in spite of the fact that they may be very noisy or the data may have significant uncertainties. Random noise or uncertainty in the data base are reduced (proportionally to $1/\sqrt{n}$, where n is the number of samples) while the "signal" in the system is increased linearly with n. The cross-correlation technique appears to offer a simple means of determining the minimum energy of the particle necessary for producing SEUs and other SEEs on spacecraft in low altitude orbits. This information can then be used to get a better understanding of the SEEs. The availability of this analysis technique adds additional motivation for updating the AP8 model.

Acknowledgments

We would like to thank J. Rose and C. Elliott for the TOPEX data. The COBE data were obtained through private communication with Tom Kelsall and Bryan Franz of the COBE project, which is supported by NASA's Astrophysics Division. Goddard Space Flight Center (GSFC), under the scientific guidance of the COBE Science Working Group, is responsible for the development and operation of COBE.

References

[1]Konradi, A. and Hardy, A. C., "Radiation Environment Models and the Atmospheric Cutoff" J. Spacecraft and Rockets, 24, p. 284, 1987.

[2]Lauriente, M., Vampola, A. L., Inamati, P., and Bilitza, D., Experimental Validation of Particle Model Drift Theories, J. Spacecraft and Rockets, Vol. 33, March-April, 1996.

[3]Rose, J., "Experiences with Single Event Upsets", TOPEX/POSEIDON Project Memo JPL D-10643, Jet Propulsion Laboratory, April 1993.

Solar Cycle Variation in the Inner Zone Proton Belt Configuration

A. L. Vampola[#]
University Research Foundation, Greenbelt, MD 20770
and
M. Lauriente[*]
NASA Goddard Space Flight Center, Greenbelt, MD 20771

Introduction

This paper presents a novel method of demonstrating atmospheric scale-height effects on energetic trapped protons. We have been using 2-D cross correlations as a powerful method of assessing the role of the trapped energetic protons in producing various effects in low altitude satellite systems. The method has permitted us to directly measure the drift of the particle South Atlantic Anomaly (due to the secular variation in the geomagnetic field) as a function of altitude and proton energy[1] and to estimate the energy of the particles causing those effects. We have also been able to address minor artifacts in the AP8[2] model, itself.[3] In this paper, we show that the technique is sufficiently powerful to address the variation in the inner zone energetic proton environment which occurs as a function of the solar cycle. The solar cycle variation arises in two ways:

First, there is a small increase in the entire magnetospheric energetic proton environment near solar minimum due to the change in the interplanetary magnetic field. As the sun becomes more quiescent nearing solar minimum, there is less turbulence in the solar wind and in the magnetic field which is embedded in it. Galactic cosmic rays then find easier access to the inner solar system, resulting in an increase in the number of cosmic rays which impact upon the Earth's atmosphere, producing the albedo neutrons which are the source of the inner zone proton belt. Thus, the proton source strength is increased during solar minimum, giving rise to an increase in the trapped flux.

The second effect is an increase in the low altitude proton flux due to the reduced residual atmospheric density during solar minimum. The primary energy input to the upper atmosphere is absorption of solar EUV (extreme ultra-violet) and soft x-rays. The production of EUV by the sun varies with the solar cycle. At solar minimum, the decrease in solar EUV and soft x-rays results in a lower average temperature in the Earth's upper atmosphere. The reduced temperature results in a reduced atmospheric scale-height, which results in a lower average atmospheric density in the regime of low altitude satellites. As a result, the energetic protons, which diffuse radially inward under the influence of temporal variations in the geomagnetic field, are able to move to lower altitudes before being degraded in energy and scattered into the atmosphere.

The variation in proton flux at low altitude is a prominent feature in the proton data base obtained from the NOAA satellites, which have been making energetic proton measurements at 800 km altitude for over a solar cycle. This variation in the energetic proton environment is presently modeled by having two versions of model environments, AP8MIN and AP8MAX. AP8MIN is more appropriate for use for missions flown during solar minimum and AP8MAX is more appropriate during solar maximum. There is a program currently underway which is investigating the relationship between the energetic proton environment and the atmospheric scale height.[4]

[#]Consultant
[*]Manager, EnviroNET

Methodology

The technique used here, and previously, is that of a two-dimensional cross correlation. The correlation is between two sets of data elements which can be ascribed a unique value based on their location in longitude and latitude (the two dimensions). In various studies, these data elements were: a) the magnetic field intensity at a specific altitude and using a specific reference model; b) the proton integral flux intensity at a specific altitude and energy threshold; and, c) proton-induced anomaly data from satellites, such as erroneous commands, single event effects (e.g., bit flips, data "glitches", etc.) or sensor noise.

The reason the 2-D cross-correlation technique is so powerful is that it compares detailed patterns with other detailed patterns. The parameter that is extracted from the correlation is not the correlation strength, which is meaningless since the individual data sets have no common normalization, but rather is the location at which the two sets show the most similarity. In our work, we actually do correlations between one data base (such as the anomalies) with a set of data bases (proton fluxes at various energy thresholds), looking for the set which produces the best overlap in location. For an example, we'll use an analysis that was done with anomalies from the TOPEX satellite, which is in a 1336 km circular orbit at 66° inclination, and the AP8 proton model. The anomaly data base is limited, but the AP8 model is not. We generate a grid of proton flux intensities, P_{ij}, at the altitude of TOPEX at 0.5° x 0.5° longitude-latitude intervals from -150° to 70° in longitude and -70° to +40° in latitude. The anomalies are used to produce a similar grid, A_{kl}, from -120° to 50° in longitude and -50° to +20° in latitude, in which the elements are the number of anomalies that have occurred in that bin. Over 95% of these bins are empty.

The anomaly grid A_{kl} is then offset with respect to the proton grid P_{ij} by -20° in both longitude and latitude and a correlation grid is produced, C_{mn}, in which each element is the sum of the products $A_{rs} \cdot P_{rs}$ where m and n are indexed ±20° by shifting the A grid by one element (0.5°) in either latitude or longitude and r,s cover the parameter space of -120° to +50° longitude and -50° to +20° latitude at 0.5° increments.

The C array is normalized and a contour plot is made of the correlation strengths. Figure 1 is one such plot, where the P grid was generated using the AP8MAX >80 MeV protons and the A grid was constructed from the TOPEX anomaly data base. The highest correlation strength occurs with essentially no offset in either latitude or longitude, indicating an excellent match between the two grids.

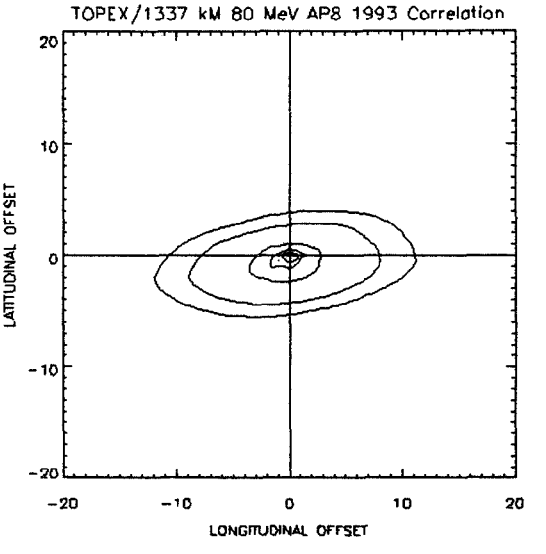

Fig. 1. Contour plot of correlation strength between AP8MAX >80 MeV protons and TOPEX SEEs.

If we do the above procedure with lower energy protons, we get a maximum correlation with an offset that is in the lower right quadrant of the contour plot, which is to be expected because the lower energy protons have their maximum flux at higher L (farther away from the equator) and are absorbed at lower atmospheric densities along their drift path, which occurs to the east. Higher energy protons protons maximize closer to the equator and further west, putting the maximum in the upper left quadrant.

Cross-correlating the TOPEX anomalies with a series of AP8MAX proton energy grids at the

TOPEX altitude produces the results seen in Figure 2. The offsets shown in Figures 1 and 2 have been corrected for the 0.25° offset in latitude that exists between the actual DGRF65 Epoch 1970 and the pseudo IGRF65 Epoch 1970 that was used for AP8MAX. The offset was determined by cross-correlating grids of the magnetic field intensities from the two models at the TOPEX altitude.

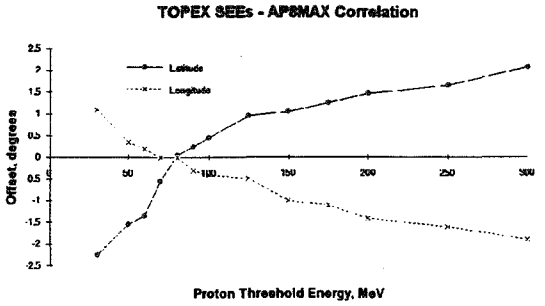

Figure 2. Offset results of cross-correlation of AP8MAX with TOPEX Earth-sensor anomalies.

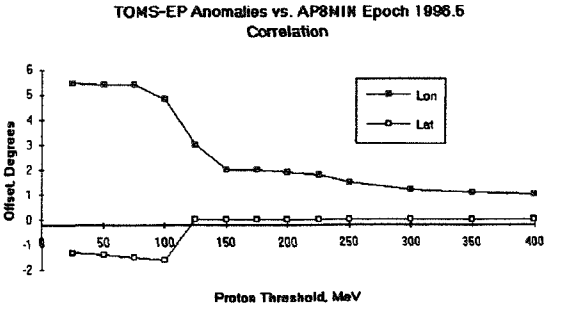

Figure 3. Offset results of cross-correlation of AP8MIN with TOMS-EP sensor anomalies.

Figure 2 indicates that the threshold proton energy for causing these anomalies is about 80 MeV. At lower altitude, the atmospheric density effect noted above (a westward trend in the location of the centroid of the energetic proton flux distribution with increasing energy) is much less.

Present Results

Figure 3 is a plot that was generated in the same manner as Figure 2, but using anomaly data from the TOMS-EP (Total Ozone Mapping Spectrometer - Earth Probe satellite launched on July 2, 1996) at 500 km altitude. Here we see virtually no change in latitude with proton energy. But we do see a change in longitude. The lack of a latitudinal variation means that at 500 km in the AP8MIN model the various proton energies have a similar L dependency (since it is the model fluxes that are being correlated with the anomalies).

The question arises as to whether there are B/B0 and L variations between AP8MIN and AP8MAX. We would expect that there should be if the two models adequately represent the actual changes in the proton environment between solar minimum and solar maximum. Comparing the two directly, e.g., comparing both models at individual energies and Ls, won't work because we really need the results from the entire distribution. We can do this readily by using the cross-correlation approach, which involves both a broad range of L (via the latitude variation) and B/B0 (via the longitude variation).

Figure 4 is a cross-correlation of AP8MAX Epoch 1991.85 with AP8MIN epoch 1995.0 at 1200 km done as a function of proton energy. Here we see a slight change (~1° in latitude (indicating a change in the L dependency as a function of solar cycle), but we do not see any change in the B/B0-dependency as a function of solar cycle. Is this correct? Fortunately, we have a way of checking it against in-situ data.

Figure 5 is a contour plot of the correlation between the location of TOMS/METEOR anomalies during the last half of 1991 and their location during the Oct. 1994-Mar. 1995 period. During this period, the centroid of the anomalies has moved 2.6° north. This 2.6 degrees in latitude corresponds to about 0.03 in L--not a lot, but measurable in the SEU data.

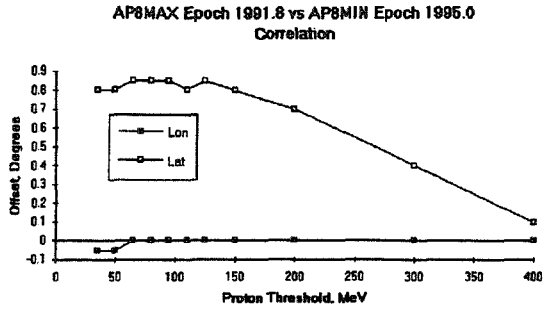

Figure 4. Comparison of AP8MAX and AP8MIN energetic proton distributions at 1200 km as a function of energy.

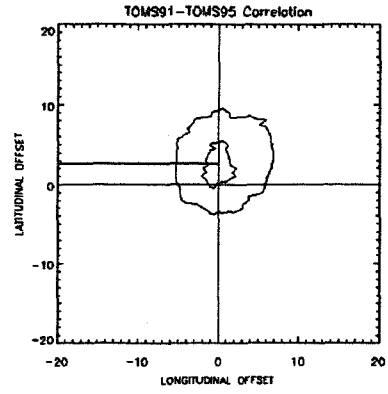

Figure 5. Correlation of the location of SEUs from the TOMS/METEOR satellite in 1991 with those in 1995. The location of the center of the SEU distribution on TOMS/METEOR moved 2.6° closer to the equator between the end of 1991 and early 1995.

This motion toward the equator represents a *lowering* in L of the center of the energetic proton distribution of about 0.03 (from about 1.29 to 1.26). This translates to an average decrease in altitude of about 250 km in the energetic proton distribution at the equator, about a factor of 3 higher than is represented in AP8. This is probably due to the change in scale height of the atmosphere-- the protons diffuse radially inward, and when the effective top of the atmosphere is lower, they go down farther before they are lost.

Discussion

This investigation is still under way. But it does serve the purpose to elucidate yet another shortcoming of the AP8 model. While the model is good, it can use improvement. These studies, using proxy data in the place of energetic proton data which are not available, have been useful in providing both impetus and direction for an improved inner zone proton model.

Acknowledgment

The cross-correlations between TOMS-EP and the AP8MIN model were performed by K. Gosier while he was an employee of Universities Research Foundation.

References

[1]M. Lauriente, A. L. Vampola, P. Inamti, and D. Bilitza, "Experimental Validation of Particle Model Drift Theories," J. Spacecraft and Rockets, Vol. 33, No. 2, March-April 1996, pp. 250-254.

[2]D. M. Sawyer and J. I. Vette, *Trapped Particle Environment for Solar Maximum and Solar Minimum (AP-8)*, NSSDC 76-06, Greenbelt, MD, 1976.

[3]Vampola, A. L., "Using Cross-Correlation Techniques to Assess the Validity of AP8 at Low Altitude," *Adv. in Space Res. 19*, 1997 (in press).

[4]Hunton, S. L., G. A. Kuck, and K. A. Pfitzer, "Low Altitude Trapped Radiation Model Using TIROS/NOAA Data," in *Radiation Belts Models & Standards*, Geophysical Monograph 97, American Geophysical Union, Washington, D. C., 1996, J. Lemaire, D. Heynderickx and D. N. Baker (eds), pp. 119-122.

Estimate of Brittle Fracture Effects in Sensor Systems Exposed to Heavy Cosmic Ray Ions

V.P. Vasilyev*, A.I. Kalinichenko**, S.V. Vasilyev*
* SOLERC, P.O. Box 30, Kharkiv, 310052, Ukraine,
** Kharkiv State University, P.O. Box 60, Kharkiv, 310052, Ukraine

Abstract. A mechanism of brittle fracture in the sensor system materials due to the powerful thermoelastic wave generated in a heavy ion track is studied. Probability of spacecraft sensor system damage is analyzed on the basis of concept of destruction zone around the ion trajectory.

As it is known, single heavy ions passing through the microelectronic elements (memory cells, chips, sensor systems, optonic devices, etc.) can cause single event failures in these, as well as hard errors due to irreversible defects in the material (see, e.g. [1]). These failures are, as a rule, connected with the charge transport and recombination processes, generation of displacement cascades and other crystal structure defects in the nanometer neighborhood of the ion trajectory. In particular, one of the main reasons for these failures is the overheated region around the ion track arising during the relaxation time τ of the linear energy transfer (LET) into the material temperature: $\tau \le 10^{-12}$ sec [2,3]. At the same time such rapid overheat yields generation of a powerful cylinder stress wave, which is able to cause crystal structure defects and even brittle fracture of material at significant (up to 1μm) distances from the track.

This work concerns the thermoacoustic destruction in a spacecraft material near a heavy cosmic ray ion track from the viewpoint of minimizing its influence on the sensor systems in space.

For the analysis we use the theory of the elastic wave excitation by a charged particle [4,5,6], as well as a simplified model of the combination "shield – sensor system", which assumes the shield as a material layer of constant thickness disposed between the cosmic ray source and the sensor system. We also take into consideration the LET irregularity along the ion trajectory and attenuation of the generated elastic wave in the material. This gives an equation to determine the ion track destruction zone radius r_d as a function of coordinate ξ counted from the ion incidence point in the material along its trajectory:

$$\frac{\Gamma \cdot k \cdot F(\xi)}{2\pi\left[R_c + S/2 \cdot \omega_a(r_d)\right]^{3/2} \cdot \sqrt{r_d}} - \sigma_d = 0,$$

where Γ, S and σ_d are the Gruneisen parameter, the longitudinal sound speed and the tensile strength of the material, respectively; $F(\xi)$ is the LET function of an ion, $R_c \approx (20 \div 50)$ Å is the radius of an energetic track containing the energy loss fraction $k = 0.6 \div 1$ [4], $\omega_a(r)$ is the minimum frequency which attenuates effectively at the length r. $\omega_a(r)$ is derived from the equation: $\beta(\omega_a) \cdot r = 1$, where $\beta(\omega)$ is the frequency absorption coefficient for the sound [7,8]. We imply the zone of possible destruction as an area $r \le r_d(\xi)$ near the ion track where amplitude of the divergent elastic wave exceeds the material tensile strength. When a border of the sensor system element lies in the destruction zone then interaction of the elastic wave with the interface

will lead to material splitting off, i.e. to irreversible changes which may yield hard errors in the system. Assuming for estimates $\sigma_d = 10^{10}\,\mathrm{dyn/cm^2}$, $\beta = 10^{-19}\,\mathrm{sec^2 \cdot cm^{-1}}$ obtain for the destruction zone radius near the maximum of the ion energy loss $r_d = 0.1;\ 0.3;\ 1$ μm for the ions having the atomic numbers $z = 5;\ 10;\ 25$ respectively [6]. Thus the destruction zone radius is $10^2 \div 10^3$ times as large as the area size of ion LET location, where all the other defects caused by the ion are concentrated.

In the framework of the proposed model we estimate the probability $p(x)$ for a point lying under the shielding layer having the thickness x to be disposed in the destruction zone:

$$p(x) = 2\pi A \cdot \sum_{z} \int_{E_{\min}}^{\infty} J_z(E)dE \cdot \int_{0}^{\frac{\pi}{2}} \pi \cdot r_d^2\left(z, E, \frac{x}{\cos\theta}\right) \cdot tg\theta \cdot d\theta,$$

where z and E are the ion atomic number and energy per nucleon, respectively, $J_z(E)$ is the ion density flux per steradian, θ is the angle of incidence, x is the shield thickness in g/cm^2, A is the normalizing constant. The summation is performed over all the atomic numbers in the cosmic ray spectrum.

So, the mechanism described can yield mechanical damage of the sensor system elements at relatively significant distances (to 1 μm and more) from the trajectory of a heavy ion. Introducing the zone of possible destruction seems to be important in estimating probability of the irreversible mechanical damage causing hard errors of a sensor system. Since this zone differs essentially by its shape from and exceeds by its volume the area of the ion energy loss, the depth profile of the damage probability distribution $p(x)$ does not resemble that predicted by the known approaches. It should be also noted that the efficiency of the described mechanism rises with the heliocentric distance due to the decrease of the energy cut-off $E_{\min}$ in the spectrum of galactic cosmic rays.

References

[1] T.R.Oldham et al. "Total dose failures in advanced electronics from single ions," *IEEE Trans. Nucl. Sci.*, Vol. 40, Iss. 6, pt.1, pp. 1820-1830.

[2] M.W.Thompson, "*Defects and Radiation Damage in Metals*," Cambridge at the University Press, 1969.

[3] I.M. Lifschitz, M.I. Kaganov, L.V. Tanatarov, "On the theory of radiation changes in metals," *Atomnaya Energiya*, Vol.6, pp.391-402, 1959 (In Russian).

[4] A.I.Kalinichenko, S.V.Vasilyev, V.P.Vasilyev, "Surface thermoelastic erosion of atmosphereless solar system bodies under bombardment by multicharge cosmic ray ions," *Earth, Moon, and Planets*, Vol.74, pp.17-33,1996.

[5] A.I.Kalinichenko, "Material Brittle Fracture Owing to Thermoelastic Effect of High Energy Nuclear Particle," *Abstract Book of the 1996 IEEE Nuclear Science Symposium and Medical Imaging Conference*, Nov. 3-9, 1996, Anaheim, CA, USA, p.83.

[6] A.I.Kalinichenko, S.V.Vasilyev, V.P.Vasilyev, "Thermoacoustic Destruction of Spacecraft Material under Cosmic Ray Bombardment," submitted to *IEEE NSREC'97.*

[8] A.I.Kalinichenko, V.T.Lazurik, "Propagation of acoustic pulses generated by fission fragments and fast neutrons in matter," *Akust. Zhurn.*, Vol.31, pp.703-709, 1985. (In Russian)

SONTRAC - a low background, large area solar neutron spectrometer

Cornelia B. Wunderer[1], Daniel Holslin[2], John R. Macri[1], Mark McConnell[1], James M.Ryan[1]

[1] Space Science Center, University of New Hampshire, Durham, NH 03824-3525 USA
[2] Science Applications International Corporation, San Diego, CA 92121 USA

ABSTRACT

SONTRAC will measure neutrons from solar flares using scintillator fibers viewed by CCD cameras to track neutron-proton scatters. SONTRAC rejects all background radiation except neutrons from the solar direction. A prototype is operational.

SONTRAC - a low background, large area solar neutron spectrometer

Solar neutrons are produced in solar flares by energetic protons (and other ions) accelerated in the corona that impact the denser regions of the chromosphere or photosphere. These same energetic protons are responsible for nuclear gamma-ray emission and π meson production. The production of π mesons manifests itself in photon emission from the decay of neutral π mesons and through bremsstrahlung of the decay electrons and positrons of the charged π mesons.

Nuclear gamma rays, neutrons and gamma rays associated with π mesons originate from different regions of the energetic proton spectrum at the Sun. The nuclear gamma-ray production is heavily weighted toward the low end of the spectrum (up to $\approx$50 MeV), while gamma rays associated with π meson production are evidence of protons with energies above 250 MeV. The intervening region of the proton spectrum (50 – 300 MeV) can only be measured by the detection and measurement of neutrons.

Both gammas and neutrons have the property that they are neutral particles and their transport through the interplanetary medium is unaffected by the ambient magnetic field. Therefore, the production or release time of the gammas and neutrons can be calculated directly from the time-of-flight over one astronomical unit once - in the case of the neutrons - their energy is known.

The radiation background encountered by an instrument in near-earth orbit consists of charged particles, gamma rays and neutrons. The primary cosmic rays consist primarily of protons and, to a lesser degree, electrons. The secondary component has many more constituents with particle lifetime seldom being important so close to the source. The secondary neutron component has a harder spectrum than the primary protons from 10 to 100 MeV but largely originates from outside the aperture of a solar-viewing instrument, i.e., from the atmosphere and the spacecraft.

Although the main neutron background SONTRAC will encounter is made up of secondary neutrons coming mostly from behind the instrument on the instrument-Sun line, any material in the instrument's aperture is capable of scattering these neutrons into the instrument, possibly mimicking a solar neutron. The efficiency of the scattering process is unknown without detailed Monte Carlo modeling or measurement, but whatever its value we can suppress its effect by requiring that the direction of a registered neutron be from the solar direction. (We can suppress the effect of gamma rays by how they deposit their energy within the instrument.) The neutron flux measured by COMPTEL at 450 km altitude and 4.5 GV, the highest geomagnetic excursion of the instrument, at 20 MeV is 3×10^{-3} n-cm^{-2}-s^{-1}-MeV^{-1} while at 100 MeV the flux is 7×10^{-4} n-cm^{-2}-s^{-1}-MeV^{-1} (Moris et al. 1995). The degree to which we can suppress the effect of these neutrons will directly affect the instrument's sensitivity.

The basic SONTRAC instrument concept consists of a closely packed bundle of square cross section organic plastic-scintillator fibers. The fibers are arranged in stacked planes with the fibers in each plane orthogonal to those in the planes above and below. This alternating orientation of fiber planes allows one to track ionizing particles in three dimensions from their origin to the point where they stop. Neutrons undergo elastic scattering off hydrogen within the organic plastic-scintillator fibers, scattering at right angles with respect to the scattered proton at non-relativistic energies. A second proton scatter of the scattered neutron provides spatial information that is necessary and sufficient to determine the incident neutron energy and direction. The non-relativistic double-scattering schematic in a solid block of plastic scintillator is shown in Fig. 1. The compact design provides a large field-of-view and a good geometrical factor with good directional information.

A conceptual sketch of the full SONTRAC instrument is shown in Figure 2. The thickness of the scintillating fibers is chosen such that a 10 MeV recoil proton traverses several fibers before stopping. The nominal fiber thickness is 200 μm and the range of a 10 MeV proton (the lowest measurable energy) is 1 mm, equivalent to 5 fibers.

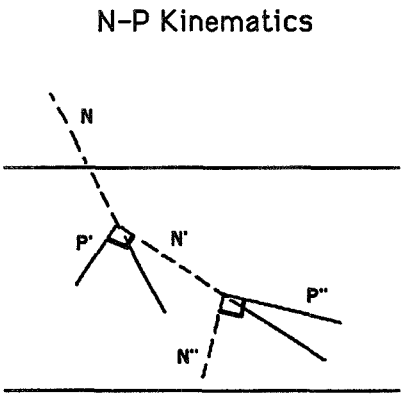

Figure 1. Schematic of non-relativistic double neutron scatter.

Scintillation light is collected from both ends of each fiber in the bundle. At one end is a series of image intensifiers and minifiers that amplify the light signals and reduce the image size for coupling to the CCD camera for image readout.

A photomultiplier (PMT) is coupled at the other end of the fiber bundle to provide a fast trigger indicating that an interaction in the fiber bundle above the specified energy threshold has taken place. A gate signal for the final intensifier and the camera shutter in each dimension is generated by fast coincidence circuitry requiring PMT triggers from both fiber dimensions and no anticoincidence signal.

The entire fiber block is surrounded by charged particle detectors to (1) reject cosmic ray protons and electrons and (2) to detect the escape of secondary charged particles from reactions within the detector. Directly behind the fiber block is a BGO gamma-ray spectrometer. The spectrometer has two functions: the first is to continuously monitor the nuclear-line gamma-ray spectrum, in particular the 4 – 7 MeV and 2.223 fluxes, the second is that of a calorimeter.

In an attempt to measure high-energy gamma rays we employ a thin Ta or Pb foil in front of the plastic block. It will produce a small number of neutron interactions, but these can be identified by the fact that proton tracks begin at the very top scintillating fiber layer. The high-energy gamma-ray detection proceeds in the same manner as the high-energy neutron mode, i.e., the calorimeter and the back plastic charged particle shield are utilized as detecting elements with no signals from the other charged particle shields.

The proposed instrument will also be compact—basically a solid block of detecting material with a very high ratio of active to passive material. The internal structure, alternating fiber planes, provides the detailed spatial information for tracking and analyzing fast proton and relativistic electron paths. The "monolithic" structure provides a large solid angle for neutron-

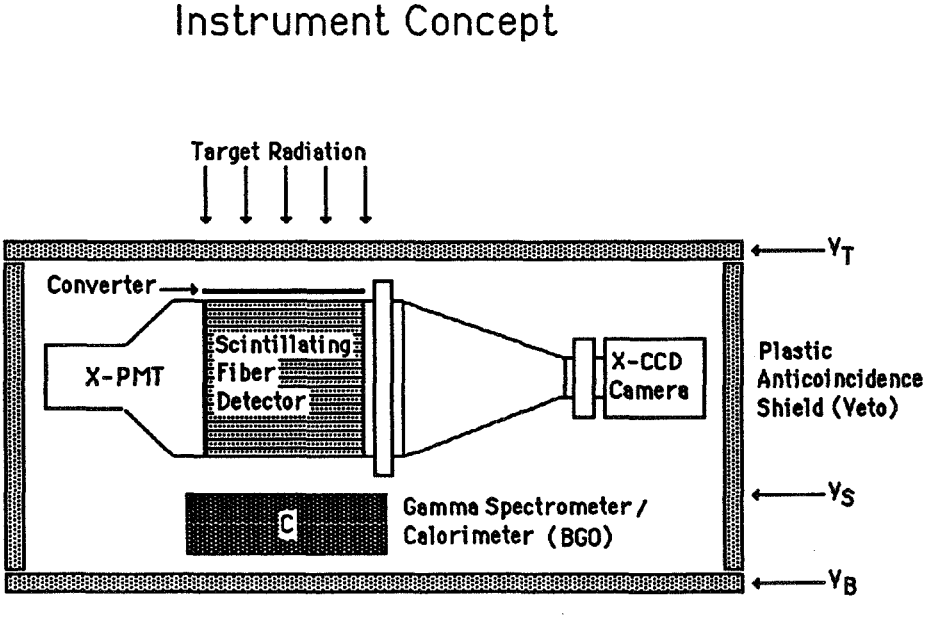

Figure 2. A Sketch of the flight-type SONTRAC instrument with Veto shields (top, sides and bottom) and calorimeter. The figure is not to scale and only the image readout electronics for one dimension is shown.

proton scattering, thereby increasing its efficiency.

The good spatial resolution of the detector provides one with the ability to distinguish between the two types of interactions, the n-C interactions showing a vertex with complex structure (several secondaries) as opposed to the isolated straight tracks produced by n-p events.

The discrimination between neutron and gamma-ray events in the bundle should be close to 100%, because the gamma-ray induced reactions, Compton scattering and pair production, result in tracks that are minimum ionizing and show appreciable multiple scattering at low energy. Bias levels or thresholds can be set to identify most of these events. The high-energy gamma-ray mode will deal with electrons > 10 MeV where multiple scattering is greatly reduced. There, the minimum ionizing nature of the tracks will identify gamma-ray events.

The angular resolution is dependent upon the ability to precisely track the recoil protons. This will be measured at threshold energies in the laboratory with the prototype. Estimates indicate that we will be able to reject ≈95% of the neutron background at 20 MeV (angular resolution ≈26°), rapidly improving with energy (> 99% of the neutron background being rejected at 40 MeV, corresponding to an angular resolution of ≈7°).

The existing SONTRAC prototype consists of a smaller fiber bundle (12x12x100 mm) with fibers in only one direction. It is therefore limited to tracking in two dimensions. The setup consists of PMT on one end and Intensifiers and a CCD-Camera on the other end of the fiber bundle. The logic setup is essentially the same as for the full-size instrument described above.

The prototype does not have anticoincidence shielding or the additional detectors used for calorimetry in the full-sized instrument.

As of today (1/97), the prototype fiber bundle has been operated with only the PMT attached. It could therefore only be used as a spectrometer. Figure 3 shows a (not yet calibrated) muon spectrum obtained by gating the PMT with a muon telescope.

We are planning to demonstrate self-triggering, single-event gating and ionization-track imaging using cosmic ray muons in the laboratory. After this is established, we plan to also show that SONTRAC is capable of single-event recoil-proton ionization-track imaging by calibrating our prototype detector with 14 MeV neutrons. These efforts are scheduled for May 1997.

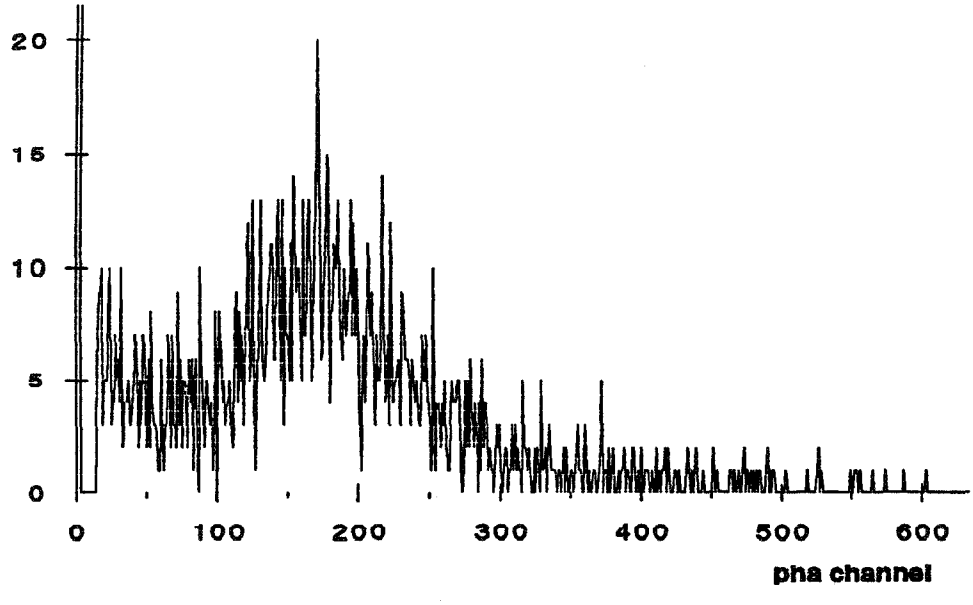

Figure 3: Muon spectrum obtained with the SONTRAC prototype by gating the PMT with a muon telescope

REPORT DOCUMENTATION PAGE

Form Approved
OMB No. 0704-0188

Public reporting burden for this collection of information is estimated to average 1 hour per response, including the time for reviewing instructions, searching existing data sources, gathering and maintaining the data needed, and completing and reviewing the collection of information. Send comments regarding this burden estimate or any other aspect of this collection of information, including suggestions for reducing this burden, to Washington Headquarters Services, Directorate for Information Operations and Reports, 1215 Jefferson Davis Highway, Suite 1204, Arlington, VA 22202-4302, and to the Office of Management and Budget, Paperwork Reduction Project (0704-0188), Washington, DC 20503.

1. AGENCY USE ONLY *(Leave blank)*	2. REPORT DATE	3. REPORT TYPE AND DATES COVERED
	July 1997	Conference Publication

4. TITLE AND SUBTITLE

Conference on the High Energy Radiation Background in Space

5. FUNDING NUMBERS

Code 691

6. AUTHOR(S)

Pamela H. Solomon, Editor

7. PERFORMING ORGANIZATION NAME(S) AND ADDRESS (ES)

Goddard Space Flight Center
Greenbelt, Maryland 20771

8. PEFORMING ORGANIZATION REPORT NUMBER

97A01316

9. SPONSORING / MONITORING AGENCY NAME(S) AND ADDRESS (ES)

National Aeronautics and Space Administration
Washington, DC 20546-0001

10. SPONSORING / MONITORING AGENCY REPORT NUMBER

NASA CP–3353

11. SUPPLEMENTARY NOTES

Co-sponsored by: Constellation Technology Corporation; IEEE/NPSS Radiation Effects Committee, Nuclear and Space Radiation Effects Conference

12a. DISTRIBUTION / AVAILABILITY STATEMENT

Unclassified - Unlimited
Subject Category: 90
Report available from the NASA Center for AeroSpace Information,
800 Elkridge Landing Road, Linthicum Heights, MD 21090; (301) 621-0390.

12b. DISTRIBUTION CODE

13. ABSTRACT *(Maximum 200 words)*

This volume contains the summaries of talks given at the second "Conference on the High Energy Radiation Background in Space," (CHERBS) held July 22–23, 1997, in Snowmass, Colorado. The first CHERBS meeting was held in Sanibel Island, Florida in 1987. As was the case in 1987, this year's meeting brought together researchers from the fields of astrophysics, planetary science, manned space flight, materials science, and electronics and sensor development. The conference focused on new data on high-energy (>1 keV) radiation in the space environment amassed in the intervening decade. Topics included X-ray, gamma ray, nuclear, solar, and cosmic radiation background measurements on balloon, satellite, planetary, and manned space flight missions using a wide variety of techniques and interpretations.

14. SUBJECT TERMS	15. NUMBER OF PAGES
X-ray, gamma ray, space radiation	118
	16. PRICE CODE

17. SECURITY CLASSIFICATION OF REPORT	18. SECURITY CLASSIFICATION OF THIS PAGE	19. SECURITY CLASSIFICATION OF ABSTRACT	20. LIMITATION OF ABSTRACT
Unclassified	Unclassified	Unclassified	UL